Chem Soc Rev

REVIEW ARTICLE

View Article Online
View Journal | View Issue

Cite this: *Chem. Soc. Rev.*, 2023, **52**, 2643

From a one-mode to a multi-mode understanding of conical intersection mediated ultrafast organic photochemical reactions

Yorrick Boeije †‡*[a] and Massimo Olivucci *[bc]

Over the last few decades, conical intersections (CoIns) have grown from theoretical curiosities into common mechanistic features of photochemical reactions, whose function is to funnel electronically excited molecules back to their ground state in regions where the potential energy surfaces (PESs) of two electronic states become degenerate. Analogous to transition states in thermal chemistry, CoIns appear as transient structures providing a kinetic bottleneck along a reaction coordinate. However, such a bottleneck is not associated with the probability of crossing an energy barrier but rather with an excited state decay probability along a full "line" of transient structures connected by non-reactive modes, the intersection space (IS). This article will review our understanding of the factors controlling CoIn mediated ultrafast photochemical reactions, taking a physical organic chemist approach by discussing a number of case studies for small organic molecules and photoactive proteins. Such discussion will be carried out by first introducing the "standard" one-mode model based on Landau–Zener (LZ) theory to describe a reactive excited state decay event intercepting, locally, a single CoIn along a single direction, and then by providing a modern perspective based on the effects of the phase matching of multiple modes on the same local event, thus redefining and expanding the description of the excited state reaction coordinate. The direct proportionality between the slope (or velocity) along one mode and decay probability at a single CoIn is a widely applied fundamental principle that follows from the LZ model, yet it fails to provide a complete understanding of photochemical reactions whose local reaction coordinate changes along the IS. We show that in these situations, in particular by focussing on rhodopsin double bond photoisomerization, it is mandatory to consider additional molecular modes and their phase relationship approaching the IS, hence providing a key mechanistic principle of ultrafast photochemistry based on the phase matching of those modes. We anticipate that this qualitative mechanistic principle should be considered in the rational design of any ultrafast excited state process, impacting various fields of research ranging from photobiology to light-driven molecular devices.

Received 21st November 2022

DOI: 10.1039/d2cs00719c

rsc.li/chem-soc-rev

1. Conical intersections in ultrafast photochemistry

Photochemistry is about the world of electronically excited states that lies, in terms of energy, above the ground state world in which thermal chemistry takes place. The interaction of a molecule with light opens up this higher world, which is not long-lived. In extreme cases, there are regions where these two worlds meet in the form of a conical intersection (CoIn),§ that is capable of funnelling the molecule from the excited state (ES) back into the ground state (GS). The GS relaxation process would then either result in regeneration of the starting molecule (a phenomenon called internal conversion, IC) or formation of a new molecule (a photochemical reaction).[1] In the latter case, we speak of a nonadiabatic¶ photochemical reaction (Fig. 1a) involving a real surface crossing between, for instance, a singlet ES PES (S_1) and the GS PES (S_0). Alternatively,

[a] *Van 't Hoff Institute for Molecular Sciences (HIMS), University of Amsterdam, Science Park 904, 1098 XH Amsterdam, The Netherlands*
[b] *Chemistry Department, University of Siena, Via Aldo Moro n. 2, 53100 Siena, Italy*
[c] *Chemistry Department, Bowling Green State University, Overman Hall, Bowling Green, Ohio 43403, USA*
† Current address: Department of Physics, Cavendish Laboratory, University of Cambridge, JJ Thomson Ave, Cambridge, CB3 0HE, UK, E-mail: yb289@cam.ac.uk
‡ Current address: Department of Chemical Engineering and Biotechnology, University of Cambridge, Philippa Fawcett Drive, Cambridge, CB3 0AS, UK.

§ The often applied acronym "CI" will not be used to avoid confusion with the popular configuration interaction method of electronic structure theory.
¶ Sometimes also called diabatic. Here we use the term nonadiabatic to avoid confusion with the diabatic states composing the adiabatic electronic wavefunction.

a nonadiabatic photochemical reaction can proceed through an avoided crossing (AC), in which the ES and GS PESs nearly touch (Fig. 1b). In contrast, the situation c in Fig. 1 shows an adiabatic photochemical reaction that takes place entirely on the ES PES, forming an excited product that can relax to the GS through fluorescence emission or IC at an AC or nearby CoIn. Whereas in b and c we indicate reactions involving, in principle, a vibrationally relaxed (*i.e.* thermalized) intermediate on the ES PES, situation a involves a photochemical reaction in which passage through the CoIn is achieved within a single vibrational period and, therefore, without generating ES intermediates. Below we will see that even the mechanistic case of Fig. 1a is far more complex than this one-dimensional picture suggests.

For a long time, it had been argued that situation b was substantially ubiquitous based on the non-crossing rule which states that electronic states with the same symmetry do not cross.[2] However, this rule is only strictly valid for diatomic molecules and it quickly became clear that CoIns are, indeed, the most common mechanistic features of photochemistry and not mere curiousities.[3–5] In the early 90s this was demonstrated *via* systematic quantum chemical investigations.[6–14] This paradigm shift in mechanistic photochemistry was supported both by advances in computational chemistry enabling the computation of ES PES gradients and therefore mapping of ES PESs as well as advances in laser spectroscopy enabling measurements of ES lifetimes in alkenes, polyenes and aromatic compounds on the femtosecond timescale, which are faster decay times than mechanisms b and c in Fig. 1 could account for.[15–18]

The nonradiative decay rate in these mechanisms can be calculated with Fermi's Golden Rule, which is a perturbation theory approach in which the overlap of vibrational wavefunctions between two electronic states in the (micro)-canonical statistical limit—*i.e.*, after intramolecular vibrational redistribution (~1 ps) and thermal equilibration in the condensed phase (~10 ps)—determines the efficiency of nonradiative decay.[19,20] Because this overlap is usually between the lowest vibrational state of the ES and a highly excited vibrational state of the GS that contains a significant nodal structure, its magnitude is small, resulting in nonradiative decay rates in the order of several picoseconds, but may extend to nanoseconds for rigid molecules in which the ES is only weakly distorted.[21,22] It is currently recognized, therefore, that ultrafast (<10 ps) photochemical and photophysical processes must involve CoIns. Whether it is favorable or unfavorable to have a prompt access to a CoIn and decay, then depends on the selected ES molecular systems. When both efficient photochemistry and high photostability are desired, having a promptly accessible CoIn is favorable, whereas it is unfavorable when a long-lived ES is the goal. Examples of these three groups of ES processes are provided in Fig. 2.

Nature provides examples of favorable ultrafast photochemical processes. One is the primary event in vision characterized by the ES of the chromophore of the visual pigment rhodopsin. Herein, the chromophore, corresponding to the protonated Schiff base of 11-*cis* retinal (rPSB11), undergoes an efficient ultrafast photoisomerization with high quantum yield (QY, defined as the number of molecules product produced divided by the number of photons absorbed), ultimately triggering the transduction pathway carrying over the visual information to the brain.[26–28] Other examples of favorable processes are found in the expanding fields of light-driven molecular devices (*e.g.* molecular motors that make often use of photoisomerization reactions as well)[29,30] and synthetic organic photochemistry (*e.g.* synthesis methods that make use of pericyclic reactions, Fig. 2a).[23] In other situations, reactivity of ES molecules is not desired, and CoIns can help to depopulate ESs without causing photoreactions. Nature has

Yorrick Boeije

Yorrick Boeije received his MSc degree in Chemistry cum laude at the University of Amsterdam and VU University Amsterdam. As part of the Holland Research School of Molecular Chemistry (HRSMC), he conducted research in spectroscopic and computational molecular photochemistry at the University of Amsterdam, Leiden University and the University of Cambridge. Yorrick is currently a PhD student in the Cavendish Laboratory at the University of Cambridge, supervised by Prof. Sam Stranks and Prof. Akshay Rao. His current research focuses on ultrafast carrier and vibrational dynamics in emergent optoelectronic materials, including inorganic-organic hybrid lead-halide (2D) perovskites.

Massimo Olivucci

Massimo Olivucci is professor of Organic Chemistry at the University of Siena, Italy and Research Professor of Computational Chemistry at the Centre for Photochemical Sciences, Bowling Green State University, USA. He authored over 290 research papers. His work focuses on the investigation of organic and bio-organic reactivity using theoretical and computational methods. The most recent results belong to two research lines: the investigation of light energy conversion in biological photoreceptors and the design of biomimetic photo-driven molecular switches and motors. The programming and implementation of fully automated hybrid quantum-mechanics/molecular-mechanics computational methodologies are also part of his work.

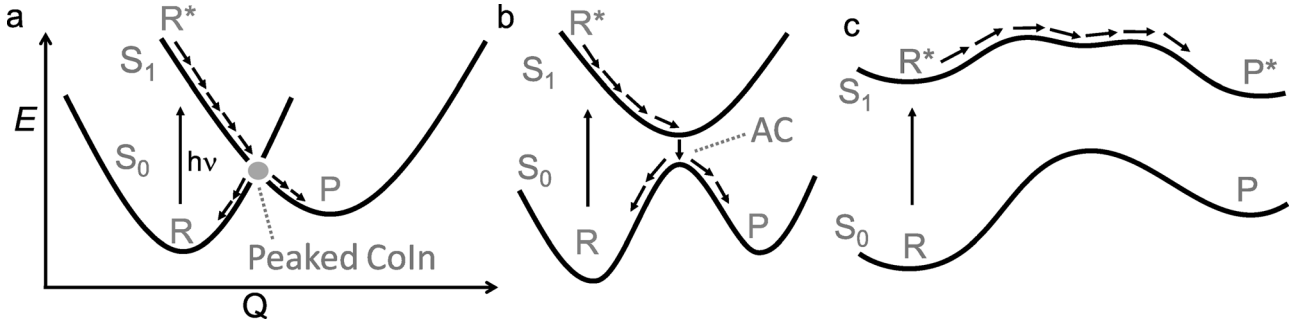

Fig. 1 One-dimensional representation for three classes of photochemical reactions involving two adiabatic electronic states S_1 and S_0 along a certain reaction coordinate *Q*. (a) nonadiabatic (diabatic) *via* CoIn (b) nonadiabatic *via* AC (c) adiabatic. R indicates reactant and P indicates photoproduct. Photochemical reactions of type a often proceed through peaked CoIns, whereas reactions through an AC are often close to a sloped CoIn. The definitions of peaked and sloped CoIns will be explained further in Section 2.1. The labels S_0 and S_1 mark PESs associated with a singlet spin-multiplicity placed in ascending potential energy order.

figured out methods to dissipate the photon energy efficiently through CoIns in thymine or cytosine DNA base pairs to compete with photochemical [2π+2π] cycloaddition, which is linked to skin cancer through disruption of the DNA strands.[31,32] Sunscreen researchers strive to achieve the same goal by designing molecules that absorb the UV light from the sun, but get rid of the excess energy rapidly through IC (Fig. 2b).[24,33] Similarly, CoIn mediated IC should be maximized in ''molecular heaters'', which are molecular light-to-heat converters with potential applications in agriculture, where their function is to improve crop yields by locally heating the plant surface after UV light absorption.[34]

Whenever a long-lived ES is required to promote either charge transfer, energy transfer (such as in optoelectronics[35–37] or photocatalysis[38]) or fluorescence (such as in luminescent organic molecular crystals[39] or super-resolution microscopy and optogenetics where fluorescent proteins are required to map cellular activity[40–42]), nonradiative decay through a CoIn should be blocked. This means that the corresponding molecule or material should be designed in such a way to avoid accessing a CoIn as much as possible, thus ''resisting'' IC. Photocatalysis is a type of photochemistry which requires the simultaneous use of a catalyst and light to promote a synthetic reaction pathway.[43] Several scenarios are possible depending on the role of the absorbing species. In one scenario, the photoexcited catalyst transfers an atom or electron to a substrate that is transformed in a reactive intermediate (*e.g.*, a radical) that then triggers a chemical reaction, after which the catalyst is regenerated in a subsequent step (Fig. 2c).[25] Alternatively, the photoexcited catalyst may sensitize a substrate through photoinduced energy transfer, changing its reactivity and ultimately triggering a chemical reaction. It has been shown in several ultrafast photoinduced electron and energy transfer processes that CoIns also mediate these processes (Section 3.3).

1.1 Theoretical description of conical intersections

In any of the above cases, it is important to understand CoIns and how they can be tuned to optimize the wanted ES process.

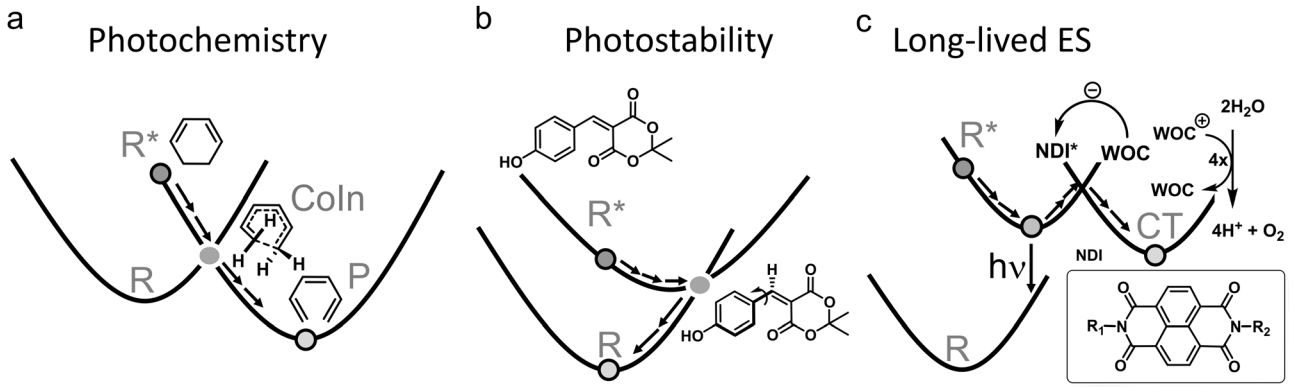

Fig. 2 Three groups of photophysical processes. (a) Photochemistry. Efficient decay through a CoIn is desired. The example provided is the electrocyclic ring-opening of 1,3-cyclohexadiene to hexatriene through a S_1/S_0 CoIn. The S_2/S_1 CoIn of this reaction is not shown.[23] (b) Photostability. Efficient decay through a CoIn is desired. The example provided is the IC process of coumaryl meldrum, which is a molecule being explored for several photoprotection applications.[24] (c) Long-lived ES. Efficient decay through a CoIn is not desired to promote longer timescale ES processes, such as fluorescence (*hν*) and photocatalysis through photoinduced charge transfer (CT). The latter is illustrated for a widely applied dye, naphthalene diimide (NDI), which after photoexcitation extracts an electron from a water oxidation catalyst (WOC) to form the radical anion of NDI. The WOC is then reactive enough to oxidize water producing oxygen in a subsequent step, which combined with the proton reduction half reaction yields hydrogen.[25]

As such understanding represents the main objective of the present review, it is convenient to revise few basic theoretical concepts that will be frequently used in the following sections. CoIns are real crossings between two adiabatic electronic states of the same spin multiplicity. Their existence can be demonstrated by considering a pair of electronic states $|\phi_1\rangle$ and $|\phi_2\rangle$, which might be S_0 and S_1 respectively. The goal is then to find the nuclear position vectors $\mathbf{Q}_x$ where the potential energies of the two adiabatic states E_1 ($\mathbf{Q}_x$) and E_2 ($\mathbf{Q}_x$) are equal. Notice that $\mathbf{Q}$ is a vector whose coordinates Q_1, Q_2,..., Q_{3N-6} are expressed on the bases of normal modes where N is the total number of atoms in the reacting system. Hence, $\mathbf{Q} = \sum_i Q_i \mathbf{N}_i$ in which Q_i are the coordinates and $\mathbf{N}_i$ are the normal mode vectors ($\mathbf{N}_i$ can be expressed as linear combinations of Cartesian unit vectors).

If we assume that the other states are far in energy, we can neglect their coupling to $|\phi_1\rangle$ and $|\phi_2\rangle$ and just consider the subspace formed by the latter two which may be written in terms of an orthogonal basis of diabatic states $|\eta_1\rangle$ and $|\eta_2\rangle$.[44] In the present context diabatic states are associated to specific electronic configurations in a Molecular Orbital language or resonance formulas in a Valence Bond language, the latter being more popular when discussing structures and reactions in organic chemistry. The energies may then be computed as follows:

$$E_{2,1} = \frac{1}{2}\left\{H_{11} + H_{22} \pm \sqrt{\Delta H^2 + 4H_{12}{}^2}\right\} \quad (1)$$

where $\Delta H = H_{22} - H_{11}$ and $H_{12} = \langle \eta_1 | \mathbf{H}_{el} | \eta_2 \rangle$. Then $E_1(\mathbf{Q}_x)$ and $E_2(\mathbf{Q}_x)$ are equal when both of the following conditions are met:

$$\Delta H\,(\mathbf{Q}_x) = 0 \text{ and } H_{12}\,(\mathbf{Q}_x) = 0 \quad (2)$$

Because diatomic molecules only have one nuclear coordinate, we have two independent equations that need to be solved and one unknown, implying that E_1 and E_2 cannot be equal. This is exactly what was referred to above as the non-crossing rule and it leads to an AC where H_{11} and H_{22} are degenerate but the coupling matrix element H_{12} is non-zero. However, this rule does not hold when the two states have different (space or spin) symmetries as in this case $H_{12}(\mathbf{Q}_1)$ is identically zero and only one equation needs to be solved. On the other hand, polyatomic molecules possess at least two coordinates Q_1 and Q_2 (*e.g.* three for triatomic molecules), allowing eqn (2) to be solved. In fact, the $E_1 = E_2$ condition is satisfied for a set of points with dimension $3N - 8$, which is called the intersection space (IS) or crossing seam.

Any CoIn is a point of the IS characterized by two branching plane (BP) vectors, $\mathbf{Q}_1$ and $\mathbf{Q}_2$, that may be defined by performing a Taylor expansion of ΔH and H_{12} at Q_x.[44,45]

$$\mathbf{Q}_1 = \nabla \Delta H(\mathbf{Q}_x) \quad \mathbf{Q}_2 = 2\nabla H_{12}(\mathbf{Q}_x) \quad (3)$$

$\mathbf{Q}_1$ and $\mathbf{Q}_2$ are molecular (*i.e.* nuclear) modes that can be regarded as the two-dimensional analogue of the one-dimensional transition vector characterizing transition states and, in the literature are also referred to as $\mathbf{x}_1$ and $\mathbf{x}_2$, $\mathbf{q}$ and $\mathbf{h}$ or $\mathbf{g}$ and $\mathbf{h}$ respectively.[1,44] In the case of a symmetry-allowed CoIn,[5] these may be referred to as tuning and coupling modes, respectively (Section 3.3).[46] Whereas the $\mathbf{Q}_1$ vector points along the direction of largest slope difference between the two intersecting PESs, the $\mathbf{Q}_2$ vector is the direction that best mixes the two degenerate adiabatic states. It is parallel to the nonadiabatic coupling vector, represented as $\mathbf{g}_{12}$

$$\mathbf{g}_{12} = \langle \phi_1 | \nabla \phi \rangle \quad (4)$$

The cone shape of CoIns along the BP may be visualized when the energy is plotted as a function of $\mathbf{Q}_1$ and $\mathbf{Q}_2$ (Fig. 3a).[47] Only molecular deformation along the BP—hence motion along the $\mathbf{Q}_1$ and $\mathbf{Q}_2$ vectors or any linear combination between them—is able to produce, locally (*i.e.* within the validity of the first order approximation), non-zero values for ΔH and H_{12}, lifting the degeneracy. In contrast, motion along any of the other $3N - 8$ nuclear degrees of freedom does not, locally, lift the degeneracy but follows the IS (Fig. 3b). As we will discuss below, often a local minimum energy CoIn (MECI) is computed and used in mechanistic analyses as a representative of the dominating decay channel (Fig. 3c). Accordingly, the slopes of the ES and GS PESs along the corresponding BP are mapped *via* reaction path computations to infer qualitative information on the population dynamics (*i.e.* on the atomic velocities) at the point of decay (Fig. 3d). More specifically, the ES slope informs on the most favourable direction of approach to the MECI along its BP and, therefore, provides a one-mode representation of the local reaction coordinate driving the ES decay.

In spite of the many MECIs and BPs reported and discussed in the literature together with their local reaction coordinate, there is no theorem supporting the decay at the MECI. In fact, it is not trivial to establish which of the IS points truly represents the dominating decay channel and, therefore, the kinetic "bottleneck" or "funnel" most relevant for the control of a photochemical reaction.[48] Below we argue that, in general, it is necessary to identify such a bottleneck with an entire IS segment thus effectively passing from a one-mode to a multi-mode description of the ES decay event.

In the following we will often differentiate between one-mode and multi-mode reactive processes. Therefore, it is useful to clarify these terms. As also discussed above, to define a set of modes, one must choose a reference basis. Such basis could correspond to the vibrational modes of the GS reactant at its equilibrium geometry. In this context, "one-mode" may refer to a reaction coordinate dominated by one specific vibrational mode. As we will also explain below, this is not the "one-mode" we are mainly discussing in the present paper. In fact, a linear combination of vibrational modes forming a "curved" reaction coordinate (*i.e.*, where the coefficients of such combination change during the progression from R* to a CoIn) may still be interpreted as a "local" one-mode process when the same trajectory enters the BP along a specific direction. In contrast, the multi-mode process of interest here refers to a motion that has a sizeable component orthogonally to the BP of a single CoIn point, which may be the MECI. In other words, we will discuss situations where the reaction coordinate is, in general,

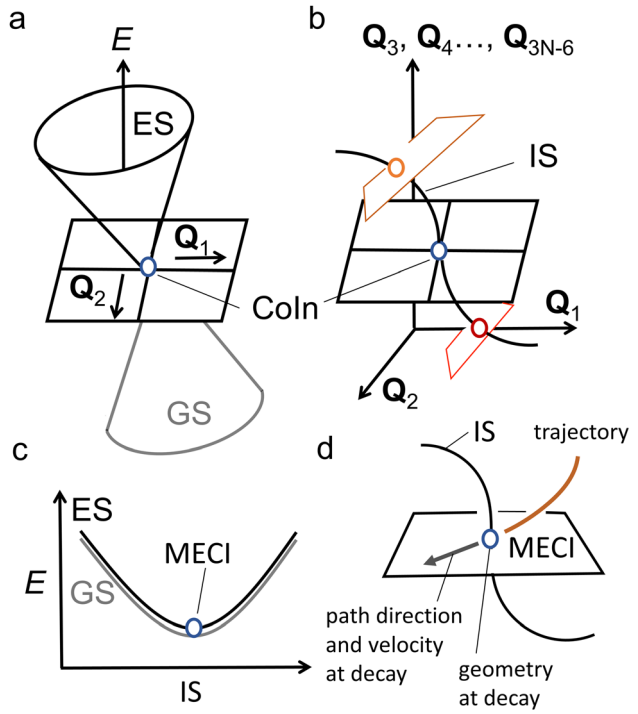

Fig. 3 Basic properties of CoIns. (a) graphical representation of a CoIn and its relationship to the BP vectors $\mathbf{Q}_1$ and $\mathbf{Q}_2$. Plotting the potential energy E as a function of these coordinates clearly shows the CoIn double cone shape. (b) illustration of the $3N-8$ dimensional nature of the IS. Each point on the IS is another CoIn characterized by its own BP vectors, here represented by $\mathbf{Q}_1$ and $\mathbf{Q}_2$. Even though the blue, orange and red CoIns lie on the same IS, their BPs are differently oriented. As a result, their corresponding PESs topographies are different. (c) When the ES and GS potential energy E is plotted along the $3N-8$ dimensional IS (here represented by a single coordinate axis), it generates, locally, a parabolic energy profile where the ES and GS are degenerate (*i.e.*, the ES (black) and GS (grey) PESs overlap perfectly). Notice that the MECI is a local minimum along the IS. (d) A standard one-mode view of the decay at the MECI. A trajectory hits the MECI along a specific direction (imposed by the ES PES topography) of its BP. The direction and velocity at decay are assumed to be critical for understanding the process outcome.

not parallel to the BP because it also projects along the IS. In this context a more convenient reference basis could be the one formally defined by the BP vectors at the MECI point plus a suitable set of modes spanning the IS. We will see that this has consequences for both the dynamics and quantum efficiency of the reaction because multiple CoIns and BPs become implicated in the reaction due to a variation in the weight of the IS spanning modes at the time of the ES decay. Therefore, below we will mostly consider a local coordinate system defined by orthogonalized BP vectors and one of the $3N-8$ remaining modes orthogonal to the BP.

1.2 Conical intersections *vs.* transition states

As a prerequisite for understanding multi-mode ES decay processes, we start by assuming that single CoIn points (*e.g.* a MECI) can be used to discuss the dynamics and kinetics of a light-induced ultrafast process (by dynamics we mean the detailed motion of the atoms as a function of time, while kinetics refers to a collective property describing, for instance, the decay time and photoproduct appearance time). This assumption will be considered valid for the rest of this section as well as for the most of Section 2, but will be released in Section 3.

Analogously to the transition state (TS) in an elementary GS reaction path (thermal chemistry), the CoIn represents a critical structure on an elementary "interstate" ES/GS reaction path (photochemistry). It can also be stated that, in both cases, the closer in energy such critical structures are to the corresponding products, the closer they would resemble the products, consistent with the Hammond postulate.[49] Despite these similarities, there are qualitative differences between a TS and CoIn even for elementary reactions (*i.e.*, a reaction where reactant and products are connected by a single critical structure). These differences are found in the local PES topography and topology (here we use these terms loosely with their meaning specified below), reaction coordinate, reaction energy profile and reaction dynamics (Fig. 4). Usually, the TS of an elementary thermal reaction is, topographically, a one-dimensional "saddle point" (*i.e.* where $\mathbf{Q}_x$ is the only nuclear coordinate associated with an energy maximum) with a smooth topology (*i.e.* with continuous first derivatives) which connects the reactant (R) and the product (P) on the GS PES. On the other hand, a CoIn has a GS PES featuring the topography of a two-dimensional spike (*i.e.* a singularity defined by discontinuous first derivatives along $\mathbf{Q}_1$ and $\mathbf{Q}_2$). A matching but opposite spike (a funnel) resides on the ES PES. Thus, such singularities connect the ES reactant (R*) to one, two or more GS products (R, P and P′) *via* a reaction coordinate that bifurcates along the BP.[19] Such a bifurcation determines the number and type of reaction paths and, thus, the photoproducts that might be generated. Of course, one of the GS branches invariably connects R* to R and therefore leads to reactant reconstitution and must correspond to an ultrafast IC event. Such a branching process shall not be confused with the topographically distinct bifurcation described in certain thermal reactions and due to a peculiar GS PES shape where a bifurcation takes place after the passage

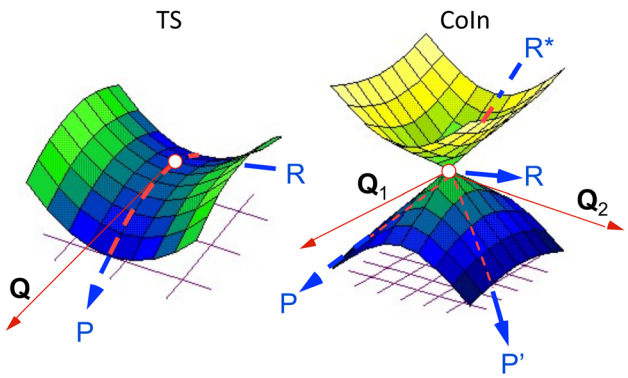

Fig. 4 Left: PES of a thermal reaction showing the reactant (R), transition state (TS) and product (P). The red arrow indicates the transition vector, $\mathbf{Q}$. Right: PESs of a diabatic photochemical reaction showing the excited reactant (R*), CoIn, GS reactant (R) and two photoproducts (P and P′). The red arrows indicate the branching plane vectors $\mathbf{Q}_1$ and $\mathbf{Q}_2$.[19]

through the critical TS structure on a PES with continuous derivatives, giving rise to multiple products (for instance different conformers).[50]

Another fundamental difference between a TS and CoIn concerns the energy profile connecting the reactant to these critical structures. In thermal reactions, TSs are always approached along energetically uphill reaction coordinates. As a result, the reaction efficiency is determined by the number of trajectories overcoming the energy barrier associated with the TS (see Fig. 5a). In contrast, the path towards the CoIn may be either energetically uphill or downhill (in Fig. 5b the CoIn is entered downhill). There is also the case where an activation barrier (*i.e.* an ES TS) separates a locally stable R* intermediate and the CoIn (Fig. 5c).[20] In this case a downhill path exists connecting the ES TS and the CoIn.

Another analogy can be made when comparing elementary schemes for selective thermal (Fig. 5d) and photochemical (Fig. 5e) reactions. It is clear from the illustration that the calculation of the different TSs accessible from R allows the prediction of the selectivity which is determined by the lower TS. The photochemical analogue will rely on different downhill slopes departing from R*. As we discuss in Section 2, a steep downhill path on the ES PES has important implications for the dynamical factors that controls the photochemistry through so called "peaked" CoIns. For "sloped" CoIns, however, the reaction path is uphill. Notice that this type of selectivity precedes, along the reaction path, the potential branching and production of different photoproducts *via* decay at a single peaked CoIn (see Fig. 4 right).

Steep downhill paths generate a further element of complexity. A R* moving towards the decay region of a peaked CoIn with finite velocity (Fig. 5b) will not decay to the GS at the MECI reached by the reaction path. In general, it will instead hit one specific point along a "line" or "segment" of the $3N - 8$ dimensional IS spanning an infinite number of CoIn structures that may include the MECI (Fig. 5f). This dimensionality issue needs to be considered when discussing the fate of the entire population of R* molecules as the one generated by a laser pulse experiment or even by the incoherent light employed in regular photochemical experiments. Thus the decay along an IS segment is a qualitatively distinctive feature of barrierless photochemical reactions not found in the nuclear motion occurring during a thermal reaction where the reactant molecule R moving towards the TS region will usually pass in the vicinity of a single isolated TS point.[48] We will now discuss how such features impact the observed reaction kinetics.

1.3 Kinetic control in ultrafast photochemistry

It appears that although there are qualitative differences between TSs and CoIns in the elementary reaction schemes discussed above, the latter can still be regarded as the ES analogue of TSs.[20] The aim of this section is to draw parallels between kinetic control in both types of reactions. As mentioned above, in a thermal reaction occurring under kinetic control the yield of product P with respect to competing product (P′) may be increased by lowering the activation barrier at the TS connecting R to P (Fig. 5d). In other words, the TS should be lowered in energy with respect to the TSs controlling other competing reaction paths ultimately leading to a high reaction selectivity.[52] Such a rational design relies heavily on the understanding of the geometrical structure and energetics of the corresponding TSs.[53] Indeed, chemists have learned to take control of kinetics through the electronic and steric tuning of TSs. Once the wanted TS structure is established and its energy relative to R is estimated, transition state theory (*i.e.* the TS is regarded as a species in equilibrium with R), amongst

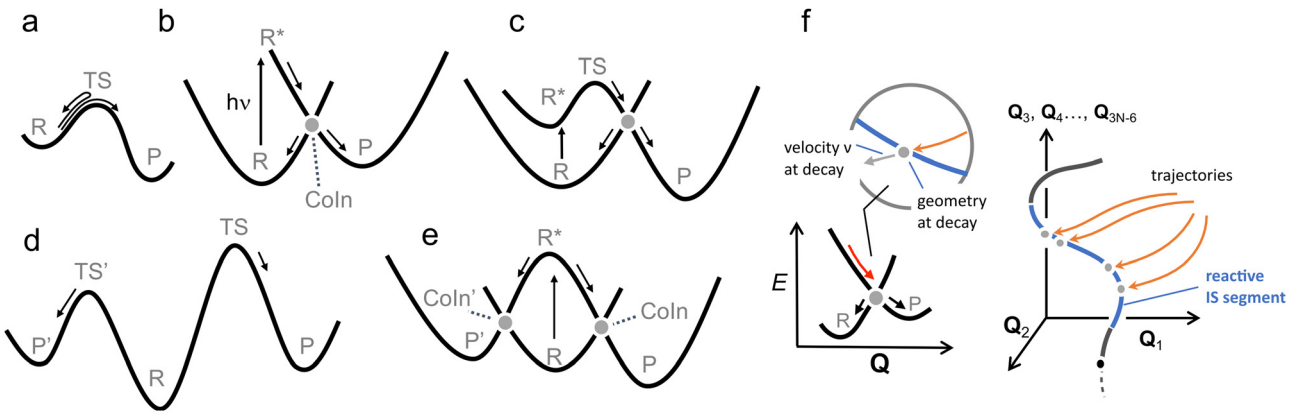

Fig. 5 Control in thermal and photochemical reactions. (a) An elementary thermal reaction. (b) Barrierless photochemical reaction leading to photoproduct formation and reactant reconstitution. The P:R* branching ration determines the QY of the reaction. Notice that this diagram corresponds to one branch of the reaction coordinates (R* to P) seen in Fig. 4. An analogue diagram could be written for the other (R* to P′) branch. (c) Photochemical reaction in which the access to the CoIn is controlled by and ES energy barrier located in correspondence of an ES TS.[51] (d) R, P and P′ are the reactant and competing products respectively. P′ is the kinetically favoured product as TS′ is lower in energy than TS. (e) Photochemical reaction in which the accessibility of two CoIns is controlled by the slopes of the ES PES, in this case biasing the reaction towards CoIn indicated by the larger (velocity) arow. A potential example of this situation is reported in Fig. 18. (f) A more realistic representation where a set of trajectories belonging to the same ES reacting population hit diverse CoIns belonging to the same reacting IS segment leading to a single product P. For simplicity we assume that each CoIn is entered along a single dominating direction (see circled inset) where a R:P branching occurs.

other basic principles, allow chemists to predict reaction rates and design thermal chemical reactivity and selectivity.[54,55]

Since there is no activation barrier in the photochemical reaction path of Fig. 5b featuring a peaked CoIn (see Fig. 4 right), the selectivity of the products must be determined by different rules as the decay point is entered in a far-from-equilibrium regime where both the geometry and the velocity at the decay point contribute to determine the reaction outcome. Such geometry and velocity must impact the quantum yields (QYs) of the different products with respect to the number of generated ES reactant molecules R* (*i.e.* the number of absorbed photons).

A practical complication that has to be considered for kinetic control in photochemical reactions is that the photoproduct might absorb at the irradiation wavelength as well, resulting in a photostationary state.[56] In many cases, however, the absorption bands of the photoproduct and reactant are well separated in energy, such as in certain molecular switches or photochromic compounds. In such a kinetically controlled regime it is, exclusively, the photochemical QY of a single transformation that determines the observed photoproduct and, therefore, reaction selectivity.

Whenever a photochemical reaction proceeds *via* a barrierless ES path through a single CoIn point (Fig. 5b), the QY is determined by the branching ratio to the possible products, which should then be controlled to obtain higher yields and selectivities.[57] In the elementary case of Fig. 5b (or Fig. 4 right), this is determined in a far-from-equilibrium regime by the corresponding ES nuclear dynamics that impact the geometry and velocity at the decay point responsible for branching.[58] The complexity of the dynamics may be further increased by the presence of multiple chemically distinct (*i.e.* leading to different photoproducts) energetically accessible CoIns (Fig. 5e) each one featuring different branching ratios.[59]

Finally, and most relevant for the present contribution, the dynamics of an elementary photoreaction is made dramatically more complex by the possibility (see Fig. 5f for a related description) that the branching itself must be a function of the position of the CoIn along the IS space. In fact, when the molecular population of R* decays not at a single CoIn point, but along an IS segment, each decay point will be associated with a different CoIn geometry, BP orientation and velocities along the BPs. Thus, the final observed selectivity will be the result of an entire range of different branching contributions. We will see how the discussion of this situation requires the anticipated expansion of the basis used to discuss the decay event from (usually) one reactive mode to a set (two or more) of modes.

1.4 Mechanistic principles for ultrafast photochemistry

This review focuses on the possibility to establish mechanistic principles useful to explain, classify and predict the outcome of ultrafast photochemical reactions. Ideally, such principles should inform the chemist on how changes in the chromophore structure and environment affect reaction selectivity and quantum efficiency. In Section 2 we start by discussing the mechanistic principles implied by Landau–Zener (LZ) theory which describes decay at an AC or CoIn considering a one-mode reaction coordinate with constant velocity at the crossing.[60] This theory will be applied to a one-mode ultrafast elementary photochemical reaction of Fig. 5b. In this ''standard'' model a single CoIn is entered along a single direction $\mathbf{Q}_x$ of the BP (Fig. 3d), which is bifurcating and therefore involves only competitive R and P formation (no competing product P′ will be considered).

In many cases predicting photochemical trends with LZ-based guidelines fails owing to the one-mode nature of the model (Section 2.3). Therefore, more sophisticated principles that incorporate the multi-mode nature of photochemical reactions are highly desired. In Section 3 we discuss how the synchronization of vibrational modes with a selected multi-mode basis controls the kinetics and QY (*i.e.* the P/R* ratio) of an ultrafast photochemical event, hence proposing a key mechanistic principle based on the '''phase matching'' of those modes.

As detailed below, this qualitative principle relies on the assumption that the light-triggered nuclear motion maintains a certain level of nuclear coherence. The phase matching between different molecular modes will be regarded as a mechanistic principle of far-from-equilibrium reactivity where the statistical distribution of velocities along the direction of bond formation plays the same role as the transition vector for a barrier controlled chemical reaction starting from a thermally equilibrated reactant.

Notice that, while the presented mechanistic principles form part of a qualitative theory of ultrafast reactivity, such theory shall not be confused with the quantitative theory used to numerically simulate photochemical reactions: nonadiabatic dynamics. In fact, as apparent from the reading of the present work, it is the analysis of nonadiabatic dynamics simulations carried out using suitable computer implementations of nonadiabatic dynamics and atomistic models that often drives the formulation of mechanistic principles.

2. The standard Landau–Zener model: focus on single CoIn structures

The development of Landau–Zener (LZ) theory goes back to the 1930s, where Landau and Zener were independently aiming to understand and calculate atomic collisions.[61,62] In their semi-classical one-mode approach, they treated the nuclei classically, introducing externally controlled parameters to deal with non-adiabatic effects occurring during such events. Even though LZ theory is already 90 years old, it is still being applied widely to provide first estimates of nonadiabatic transition probabilities in both complex and simple systems.[60,63]

LZ theory considers a two-state model involving one nuclear coordinate Q to calculate the probability P to change adiabatic state (eqn (5)), *i.e.*, decay to the lower state. For a complete derivation, the reader is referred to ref. 60. We only present here the result and the most important assumptions. In the

following discussion, we make frequent use of definitions already set out in Section 1.

$$P = \exp\left(-\frac{2\pi {H_{12}}^2}{|vF|}\right) \quad (5)$$

In eqn (5) v is the velocity of nuclear motion along Q on the upper PES (*i.e.*, the reaction coordinate pointing to the CoIn), which is assumed to be constant, and F is the difference in slopes ($F_2 - F_1$) of $H_{22}(Q)$ and $H_{11}(Q)$, see Fig. 6a. The parameters H_{12} and F are also set to be constant and H_{12} is assumed to be small to describe weakly AC regions. The electronic states are conveniently represented by diabatic states $|\eta_1\rangle$ and $|\eta_2\rangle$ whose combination yield the adiabatic states $|\phi_1\rangle$ and $|\phi_2\rangle$ (S_1 and S_0 in Fig. 6a, respectively). Notice that the diabatic and adiabatic representations coincide in regions far from the crossing, where the nonadiabatic coupling vanishes.[44] For instance, whereas the adiabatic states S_1 and S_0 are well described by the diabatic state $|\eta_2\rangle$ at the reactant and product equilibrium geometry, respectively, $|\eta_1\rangle$ describes S_0 at the reactant equilibrium geometry and S_1 at the product equilibrium geometry. In the regions where $|\eta_1\rangle$ and $|\eta_2\rangle$ cross, H_{12} modulates their coupling and affects the rate of nonadiabatic transfer (compare panels i and iii in Fig. 6b). When there is a real crossing, as in a CoIn ($H_{12} = 0$), P becomes unity, hence providing a 100% efficient funnel from the ES to the GS, within a single vibrational period (*i.e.* passage through the crossing region) and without any intermediates. Such a transition is fully diabatic as the electronic character of the diabatic state is conserved. In contrast, for a non-zero H_{12} there is a certain probability to change diabatic state upon passage through the AC region, reducing the probability for nonradiative decay to the GS. Although for a large H_{12} the LZ model predicts a fully adiabatic passage (small P), its predictions lose accuracy in this regime due to the above-mentioned assumptions (*e.g.* small H_{12}) required to derive eqn (5).

A key result from the LZ formula is that it relates v to the nonadiabatic decay probability. As demonstrated in panels i and ii in Fig. 6b, P increases when the velocity at the point of (near) degeneracy is larger, *i.e.*, the population continues moving on the same diabatic state after passing the crossing with an exit direction identical to the entry direction.[64] This greater velocity could be due to a steeper slope on the ES PES (F is a topographical factor), which implies faster molecular motion (v is a dynamical factor).

The qualitative interpretation of LZ theory, namely the direct proportionality between the nuclear velocity or slope along a diabatic PES and the probability of decaying maintaining the nuclear velocity direction (*i.e.* assuming one entry and exit direction of motion), can be seen as a fundamental principle valid along the nuclear mode Q intercepting a specific CoIn. This is considered the "standard" LZ model applied to MECI points. Such interpretation is not concerned with the complete nuclear trajectory $\mathbf{Q}(t)$ of a molecule, which is dependent on both topographical aspects,[65–67] as well as dynamical aspects inherent to the far-from-equilibrium nature of ultrafast photochemical reactions,[20,48,68] (*e.g.* how the photoexcited reactant reaches the CoIn region, which of the infinite number of CoIn is actually reached or whether the population is split before reaching the CoIn). As this trajectory consists of a set of molecular modes, application of the LZ formula may be non-trivial as the choice of Q may be ambiguous for curved reaction coordinates (*e.g.* when obtained by interpolating reactant and MECI geometries) and a full reaction mapping is rarely carried out due to its relatively high computational cost.

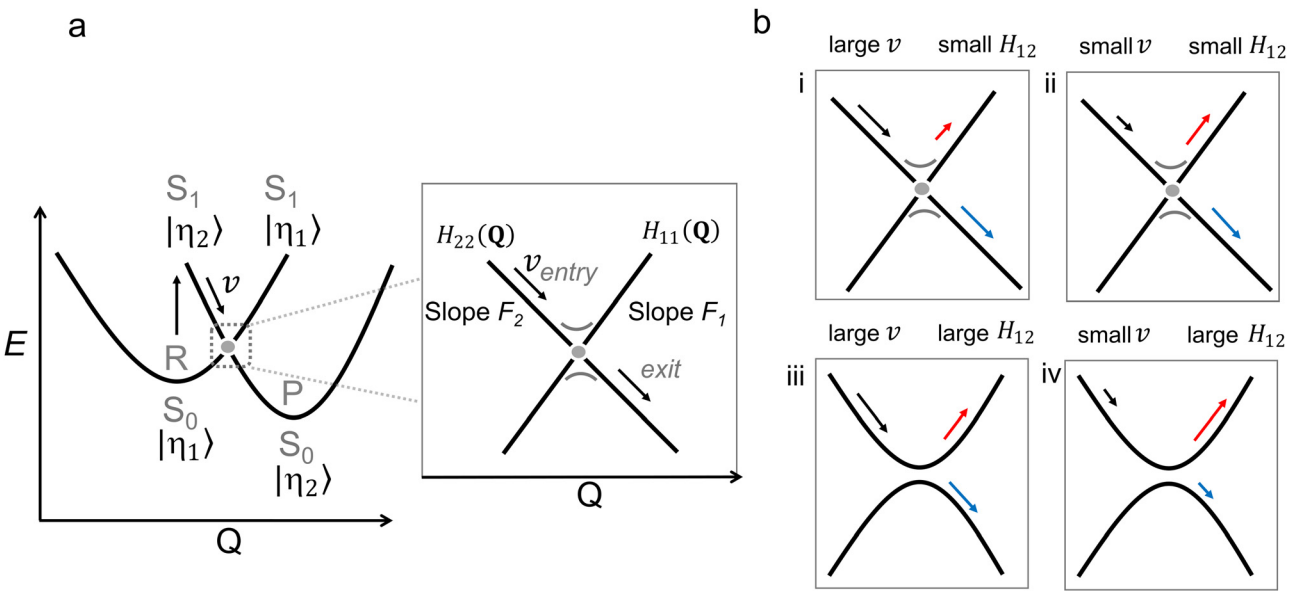

Fig. 6 (a) Diabatic representation of a photochemical reaction according to the Landau Zener model. The diabatic parabola are approximated by straight lines close to the crossing region, as shown in the inset. In this inset, the relevant parameters for the Landau Zener formula (eqn (5)) are shown as well. (b) Four situations (labelled i–iv) of a photochemical reaction illustrating its dependence on the velocity and the coupling between the diabatic states H_{12}. The blue and red arrows indicate the probability to switch adiabatic PES (large P) and to stay on the adiabatic PES (small P), respectively.

P may be statistically reinterpreted as the fraction of trajectories switching to another adiabatic state (*e.g.* the fraction hopping from the S_1 to S_0 PES). Alternatively, we will make frequent use of the term vibrational wavepacket or, simply, wavepacket to describe the temporal evolution of a compact ES population of molecules featuring phased nuclear motion. The reader is referred to Section 3.1 for a more detailed description of vibrational wavepackets and their implied in-phase nuclear motion (vibrational coherence).[69] The (center of the) wavepacket moves along a PES with a particular direction and magnitude of velocity, which correlates, similar to the trajectory description, to the efficiency of nonadiabatic decay according to eqn (5).

For barrierless photochemical reactions (such as those in Fig. 6b) v inversely correlates to the experimentally observable ES lifetime τ. For this reason, the relation between v and *P* has been used to explain a correlation between τ and QY.[70,71] This is because, in a one-mode interpretation, if the evolution of the ES wavepacket is such that it points to the CoIn and then, without changing direction, to the photoproduct, a velocity increase leads to a QY enhancement.[72] Hence, a larger velocity of the ES wavepacket towards the CoIn, or a shorter experimental τ, correlates with a higher photochemical QY. Many researchers have proposed the validity of such an inverse relation between lifetime and photochemical QY, such as for the reduced QY in isorhodopsin (QY = 0.22, τ = 600 fs) compared to rhodopsin (QY = 0.67, τ = 200 fs),[73] or the smaller QY for reverse photoisomerization in overcrowded alkene molecular motors (QY = 0.40, τ = 1770 fs) compared to the forward reaction (QY = 0.92, τ = 1400 fs).[74] Below we will see how such a relationship may fail in a number of cases.

2.1 Excited state and CoIn topographies

In this section, we focus on how ES PES and CoIn topographies affect photochemistry within the framework of the standard LZ model by consideration of the entry–exit direction and the magnitude of nuclear velocity v. However, as also mentioned above, it will become clear that applying the LZ formula is often not trivial due to the topographical complexity of the ES PES and CoIn and, therefore, the difficulty in obtaining information on the velocity magnitude and direction at the decay point. The LZ-related models that tackle the relations between ES PES and CoIn topographies and nonadiabatic decay rates can be found in the literature.[68,75–80] However, here we summarize their main results by considering six topographical factors (Table 1).

2.1.1 Barrier(less) ES reaction path. In Fig. 5c, an activation barrier separates the Franck–Condon (FC) region, *i.e.*, the ES structure generated *via* vertical excitation, from the CoIn. These processes are typically not ultrafast, unless the barrier is sufficiently small, and part of the excitation energy is converted into thermal energy, which increases the effective temperature. As the photochemical reaction is thermally activated, wavelength and temperature dependent effects occur. The application of the LZ formula is not straightforward as one has the problem of determining the coordinate driving the reaction after the TS on the ES has been overcome, thus the entry direction with which the molecule approaches the CoIn. Furthermore, as the velocity at the CoIn has no connection with the ES lifetime in this case, the inverse correlation between ES lifetime and reaction QY does not hold. Relevant information can be obtained by computing the minimum energy path connecting the TS to the CoIn.

2.1.2 Number of independent GS relaxation paths departing near CoIn. A CoIn is topographically classified as a single-path intersection when there is a single preferred relaxation direction on the GS PES that results in regeneration of the reactant (*i.e.* IC), whereas it is a bifurcating intersection if there are two such directions, one corresponding to the reactant and one to a photoproduct.[80,81] Whereas this represents a local CoIn classification (Section 2.1.3), we point out here the possibility of entering two different GS valleys, after population of the photoproduct path (see Fig. 4, right).[82] In this case one may have access to two photoproducts rather than only one. Accordingly, three GS relaxation paths are possible, whose directions are characterized by specific combinations of BP vectors. In this case it is not clear in which specific exit direction the LZ formula should be applied, although one may think of projecting the ES path direction pointing to the CoIn on the GS paths describing the exit from the CoIn. This would lead to wavepacket fragmentation, or population splitting, even in a situation of a peaked CoIn (see also below).[11,83,84]

2.1.3 Local CoIn topographies. We start by discussing the local topography of CoIns (usually MECIs) by defining the following projections

$$s_x = \mathbf{s}\cdot\hat{\mathbf{x}} \quad (6)$$

$$s_y = \mathbf{s}\cdot\hat{\mathbf{y}} \quad (7)$$

where the $\hat{\mathbf{x}}$ and $\hat{\mathbf{y}}$ vectors are the orthogonalized and normalized analogues of the $\mathbf{Q}_1$ and $\mathbf{Q}_2$ vectors we introduced in

Table 1 Summary of ES and CoIn topographies and which LZ factor they mainly impact. Whereas II–IV are topographical CoIn features, I, V and VI affect ES regions further from the relevant CoIn

Topographical factor	LZ factor	Illustration
I ES reaction path with *vs.* without barrier	Entry direction	Fig. 5c and 9d
II Number of independent GS relaxation paths departing near CoIn	Exit direction	Fig. 4
III Local CoIn topographies	Velocity and entry direction	Fig. 7–9
IV Location and energy of CoIn along the reaction path	Velocity[a]	Fig. 9
V ES Slope on the reaction path to CoIn	Velocity	Fig. 5e and 9
VI Electronic mixing with higher states	Entry direction and velocity	Fig. 10

[a] If a CoIn becomes energetically inaccessible, the entry direction might be changed to another CoIn.

eqn (3).[85] The seam coordinate **s** is the average gradient of the two states (here labelled as A and B)

$$\mathbf{s} = \frac{1}{2}\nabla(E_A + E_B) \tag{8}$$

The relative tilt σ parameter indicates the degree of slope and is defined as

$$\sigma = \sqrt{s_x{}^2 + s_y{}^2} \tag{9}$$

The local topography of CoIns can be further characterized by the ellipticity Δ (or asymmetry) and pitch δ (or strength) parameters, which are related to the difference and average length of the orthogonalized $\mathbf{Q}_1$ and $\mathbf{Q}_2$ vectors, $\widetilde{\mathbf{Q}_1}$ and $\widetilde{\mathbf{Q}_2}$:

$$\Delta = \frac{\widetilde{\mathbf{Q}_1}\cdot\widetilde{\mathbf{Q}_1} - \widetilde{\mathbf{Q}_2}\cdot\widetilde{\mathbf{Q}_2}}{\widetilde{\mathbf{Q}_1}\cdot\widetilde{\mathbf{Q}_1} + \widetilde{\mathbf{Q}_2}\cdot\widetilde{\mathbf{Q}_2}} \tag{10}$$

$$\delta = \sqrt{\frac{\left(\widetilde{\mathbf{Q}_1}\cdot\widetilde{\mathbf{Q}_1} + \widetilde{\mathbf{Q}_2}\cdot\widetilde{\mathbf{Q}_2}\right)}{2}} \tag{11}$$

For strongly elliptical CoIns (*e.g.* when Δ is ± 1) the CoIn is infinitely narrow and would appear as a near one-dimensional crossing, having a $3N - 7$ dimensional IS.[86] A CoIn having $\Delta = 0$ corresponds to a perfectly circular one. δ indicates how steep the CoIn is.

Switching to polar coordinates the energies of the two states, where the energy of the CoIn E^X is placed at the origin, are

$$E^A(r,q), E^B(r,q) = E^X + \delta r\left(\sigma\cos(\theta - \theta_s) \pm \sqrt{1 + \Delta\cos(2\theta)}\right) \tag{12}$$

where $r = \sqrt{x^2 + y^2}$ and $\tan\theta = \frac{y}{x}$ are the polar coordinates in the BP and Δ and δ are now defined as

$$\Delta = \frac{\Delta E_x(r)^2 - \Delta E_y(r)^2}{\Delta E_x(r)^2 + \Delta E_y(r)^2} \tag{13}$$

$$\delta = \sqrt{\frac{\Delta E_x(r)^2 + \Delta E_y(r)^2}{8r^2}} \tag{14}$$

in which $\Delta E_x(r)$ and $\Delta E_y(r)$ are the energy differences between the two states at a certain r along the x and y directions, respectively (Fig. 7a). Further, the relative tilt (now defined using polar coordinates) is defined as

$$\sigma = \frac{E_S(r)}{\delta \cdot r} \tag{15}$$

in which $E_S(r)$ is a plane of the average energy (green plane in Fig. 7a), which is tilted with respect to the xy plane (red plane in Fig. 7a). The angle for which E_S is maximum (at a given r) is θ_s, the direction of the tilt,

$$\tan\theta_s = \frac{s_y}{s_x} \tag{16}$$

Notice that for a ''model CoIn'' (*i.e.*) one that is linear in r, see eqn (12), the r dependence in eqn (13)–(15) can be eliminated yielding parameters Δ, δ, and σ independent of r. However, in real molecules, higher-order terms in the PES are present and the same parameters change as a function of r.

The motivation for introducing the parameters Δ, σ and θ_s is that they can be rearranged into two parameters, $\mathcal{P}$ and $\mathcal{B}$, which allow for a complete CoIn characterization (provided that $\Delta \geq 0$) by distinguishing between peaked or sloped, as well as between bifurcating or single-path,[80,81,87] respectively:

$$\mathcal{P} = \frac{\sigma^2}{1 - \Delta^2}(1 - \Delta\cdot\cos(2\theta_s))\begin{cases} < 1 \text{ peaked} \\ > 1 \text{ sloped} \end{cases} \tag{17}$$

$$\mathcal{B} = \sqrt[3]{\frac{\sigma^2}{4\Delta^2}}\left(\sqrt[3]{(1+\Delta)\cos^2(\theta_s)} + \sqrt[3]{(1-\Delta)\sin^2(\theta_s)}\right)\begin{cases} < 1 & \text{bifurcating} \\ > 1 & \text{single-path} \end{cases} \tag{18}$$

Several general topographical classifications can be made based on these conditions, which we illustrate in Fig. 7b–f. A circular CoIn ($\Delta \sim 0$) with zero tilt ($\sigma = 0$) is shown in Fig. 7b. As both $\mathcal{P} < 1$ and $\mathcal{B} < 1$, this situation represents a peaked bifurcating CoIn. The bifurcation is more obvious in the elliptical (peaked) CoIn from Fig. 7c, having two distinct preferential relaxation paths from the CoIn as determined by the larger slopes along those paths. The CoIns of Fig. 7b and c are peaked as they are a local minimum (but not a stationary point as the gradient is discontinuous and non-vanishing at the CoIn) of the energetically higher PES in the BP.

When σ is increased to 1.5 while setting Δ again to 0.01, we obtain a sloped single-path CoIn (both $\mathcal{P} > 1$ and $\mathcal{B} > 1$), as shown in Fig. 7d. In this case there is a true local minimum (*i.e.* a point where the gradient of the energetically higher PES with respect to the nuclear coordinates is zero) that is lower than the CoIn but located in its vicinity (Fig. 2b).[45,88] Atchity *et al.* further define an *intermediate* situation, in which the energetically higher PES has a zero slope on one side of the CoIn and the energetically lower PES has a zero slope on the other side (for simplicity purposes, this situation is not further illustrated).[45] The relevance of the distinction between peaked and sloped CoIns for photochemical reactions will be discussed below.

From the conditions set out in (17) and (18) it can be established that a CoIn is sloped for $\sigma > \sqrt{2}$ and peaked for $\sigma < \sqrt{2}$. Secondly, a CoIn is bifurcating when $\sigma < \Delta$. If now instead both σ is increased to 0.7 and Δ is increased to 0.5, *i.e.* both the tilt and ellipticity are increased with respect to Fig. 7b, a peaked single-path CoIn is obtained (Fig. 7e). Finally, a sloped CoIn that is also bifurcating is only possible for $\Delta > 1/3$, which is demonstrated in Fig. 7f. As this is not a common situation, sloped CoIns are often associated with a single-path on the GS (an example is shown in (Fig. 8b)), implying IC and therefore regeneration of the reactant.[89] Therefore, based

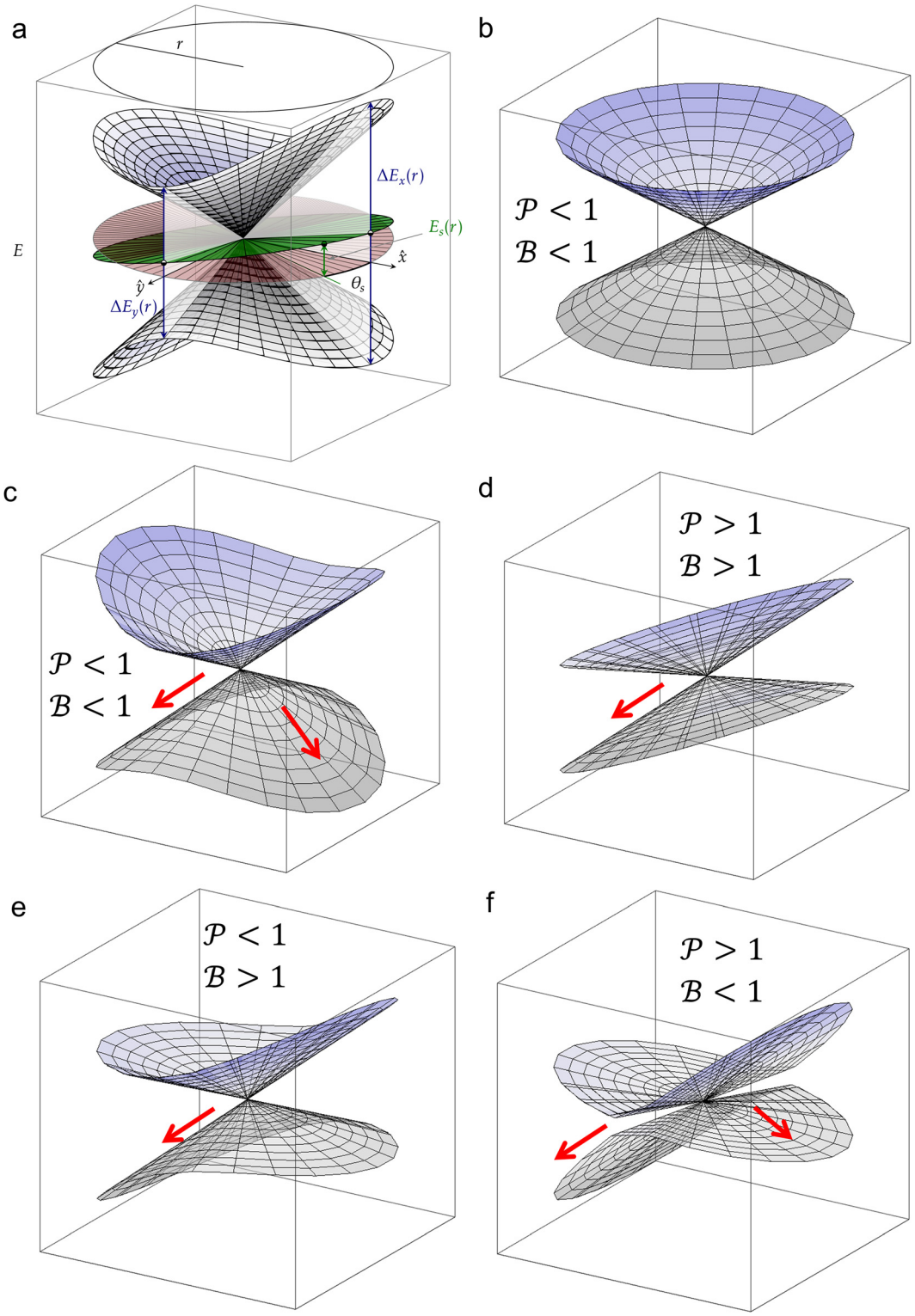

Fig. 7 (a) Graphical representation of PESs around a CoIn in the branching plane, defined by vectors, which are the orthogonalized and normalized analogues of the $\mathbf{Q}_1$ and $\mathbf{Q}_2$ vectors, respectively. The topographical CoIn classification (see text, and Table 1) is based on the characteristic parameters and variables shown in this figure. At a distance r from the intersection, the energy differences between the two states along the x and y coordinates are $\Delta E_x(r)$ and $\Delta E_y(r)$, respectively. The pitch δ and ellipticity parameter Δ are related to their sum and difference, respectively. The green plane is the average energy, which is tilted with respect to the xy (red) plane. The maximum average energy at a given r, $E_S(r)$, is defined at the angle θ_S, the direction of tilt. The relative tilt σ is defined by both $E_S(r)$ and δ. Figure (b)–(f) show different CoIn topographies as defined by the $\mathcal{P}$ and $\mathcal{B}$ descriptors, which are dependent on the parameters Δ, σ and θ_S. For all graphics θ_S was set to 6 rad and δ to 1. The latter is a scaling factor and does not affect the values of $\mathcal{P}$ and $\mathcal{B}$. Adapted from ref. 81, licensed under a Creative Commons Attribution 4.0 International License. (b) peaked/bifurcating (Δ = 0.01, σ = 0). (c) peaked/bifurcating (Δ = 0.5, σ = 0.01). (d) sloped/single-path (Δ = 0.01, σ = 1.5). (e) peaked/single-path (Δ = 0.5, σ = 0.7). (f) sloped/bifurcating (Δ = 0.99, σ = 1).

on this topographical difference, peaked CoIns are usually more photoreactive (*i.e.* higher photochemical QY) than sloped CoIns, which is why they are often referred to as photochemical funnels.[69,90]

For instance, through *ab initio* calculations it has been proposed that the distinction in peaked/sloped topography could explain the selective photoisomerization at the C_{11}=C_{12} bond of an abridged model of the protonated Schiff base of all-*trans* retinal, rPSBAT, (Section 3.1). The local CoIn dynamics, far from the FC-point, at both type of CoIns is illustrated in Fig. 8. Isomerization around the C_{11}=C_{12} bond is associated with a peaked CoIn, whereas isomerization around the C_{13}=C_{14} bond corresponds to a sloped CoIn, which is associated with a lower nonadiabatic efficiency and is therefore outcompeted by the ultrafast C_{11}=C_{12} isomerization.[91] The photochemical reaction path of the latter in fact proceeds, with higher probability, through an AC as shown by the one-dimensional slice along the torsional reaction coordinate. The same distinction has been used to explain the faster photoisomerization of a rPSB11 model in aqueous solution (peaked) compared to gas-phase (sloped).[51]

In general, peaked CoIns are associated with larger nonadiabatic transfer efficiencies compared to sloped CoIns, which Malhado *et al.* have proposed is not a result of their inherent topographical differences but due to dynamical factors.[68] Because a peaked CoIn represents a local minimum on the ES PES, the wavepacket approaches the CoIn with high nuclear velocity (eqn (5)) as the ES PES steers the wavepacket in the right downhill direction (Fig. 9a and b). In contrast, as there are uphill ES paths towards a sloped CoIn, the wavepacket might miss the CoIn as the ES PES steers the wavepacket away from it. Additionally, in peaked CoIns nonadiabatic transfer is likely to occur without any wavepacket fragmentation as the transition takes place in the first passage, which further enhances the nonadiabatic transfer efficiency due to the conservation of coherence of the ES population as we will more precisely describe in Section 3.1.[68]

Due to the smaller nuclear velocity that is generally associated with a ES wavepacket reaching a sloped CoIn (Fig. 9c), irreversible passage to the GS PES is not guaranteed as such a wavepacket can travel back along the ES PES (a process called "up-funneling", which reduces coherence), which manifests

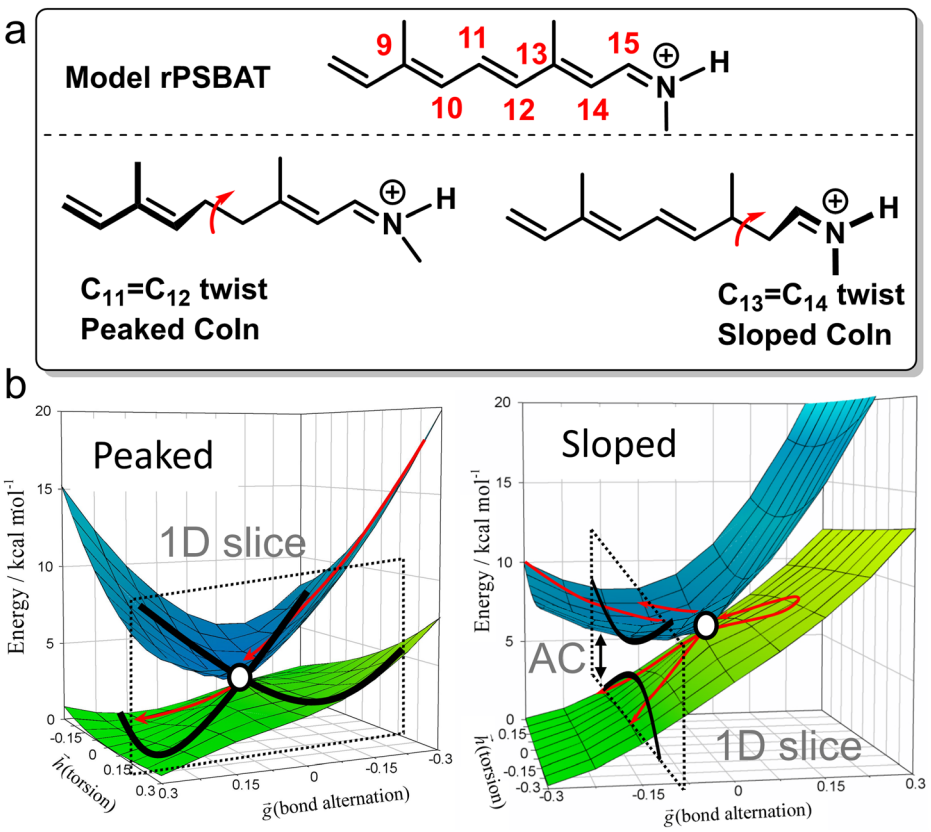

Fig. 8 Photoisomerization of model rPSBAT through two different routes. (a) Chemical structures of model rPSBAT and the MECIs corresponding to isomerization at the C_{11}=C_{12} bond and the C_{13}=C_{14} bond. The labelling of the carbon framework is chosen to be consistent with the photoisomerization of the complete chromophore, rPSB11, discussed in Section 3. (b) Adiabatic PESs involved for both reactions. Left: Isomerization at the C_{11}=C_{12} bond, corresponding to a bifurcating/peaked CoIn. Right: Isomerization at the C_{13}=C_{14} bond, corresponding to a bifurcating/sloped CoIn. Adiabatic PESs are computed at the CASSCF level, showing the energy as a function of the **g** and **h** vectors, which are the analogues of $\mathbf{Q}_1$ and $\mathbf{Q}_2$, respectively. The red arrows indicate the path of the ES wavepacket. Note the up-funneling process around the sloped CoIn.[91] When slicing these two-dimensional plots along one reaction coordinate, the curve representation analogues of Fig. 1 are retrieved. Adapted with permission from ref. 91. Copyright (2002) National Academy of Sciences, USA.

itself as oscillations between the ES and GS PESs near the sloped CoIn (see Fig. 8b).[48,91–94] Nevertheless, even if the sloped CoIn is reached with sufficient energy, this process may cause wavepacket fragmentation (*i.e.* partial loss of coherence), which itself decreases nuclear velocity.[92,95]

As a result of the slower nuclear dynamics and more significant loss of coherence, nonadiabatic transfer at sloped CoIns might occur under near-equilibrium conditions, where (partial) intramolecular vibrational energy redistribution has taken place.[96] In contrast, far-from-equilibrium conditions (fast nuclear velocity and coherence) are often maintained for peaked CoIns due to the steep gradient of the ES PES and therefore dominate the photochemistry.[69] In other words, photochemical reactions approaching a peaked CoIn are more prone to memory of the initial conditions imposed by the photoexcitation on other regions of the ES PES. One should therefore keep in mind that differences in photochemical reactivity between peaked and sloped CoIns are not only controlled by their local structure but also by these far-from-equilibrium conditions, as well as other topographical factors (Table 1).

2.1.4 Location and energy of CoIn along the reaction path. Since the peaked CoIn represents the critical structure of elementary photochemical reactions in analogy with TSs for elementary thermal reactions, they may be discussed also in terms of the Hammond postulate.[97] However, it is apparent that certain thermodynamic features of a TS should be reinterpreted in terms of far-from-equilibrium dynamic features. For instance, a reactant-like CoIn (R* and CoIn are closer in energy than P and CoIn, Fig. 9a) would probably project the wavepacket to the GS with a low velocity rather than featuring a small barrier (and fast kinetic) as in a reactant-like TS.[98] In contrast, a product-like CoIn (P and CoIn are closer in energy than R* and CoIn, Fig. 9b) probably has a large velocity upon decay rather than featuring a high barrier (slow kinetic) as in a product-like TS. According to the standard LZ model, the reactant-like CoIn would have a lower QY with respect to the product-like CoIn. If a particular CoIn is energetically inaccessible, the entry direction of two competing CoIns might be controlled by an ES barrier (factor I), as shown in Fig. 9d.

2.1.5 ES Slope on the reaction path to CoIn. Whereas the higher velocity of the photochemical reaction path in Fig. 9b compared to Fig. 9a is due to the relative position of the CoIn along the reaction path, the ES slope, *i.e.*, the ES force field that a normal mode relevant to the reaction coordinate experiences, may increase the velocity of R* approaching the CoIn as well (Fig. 9e).

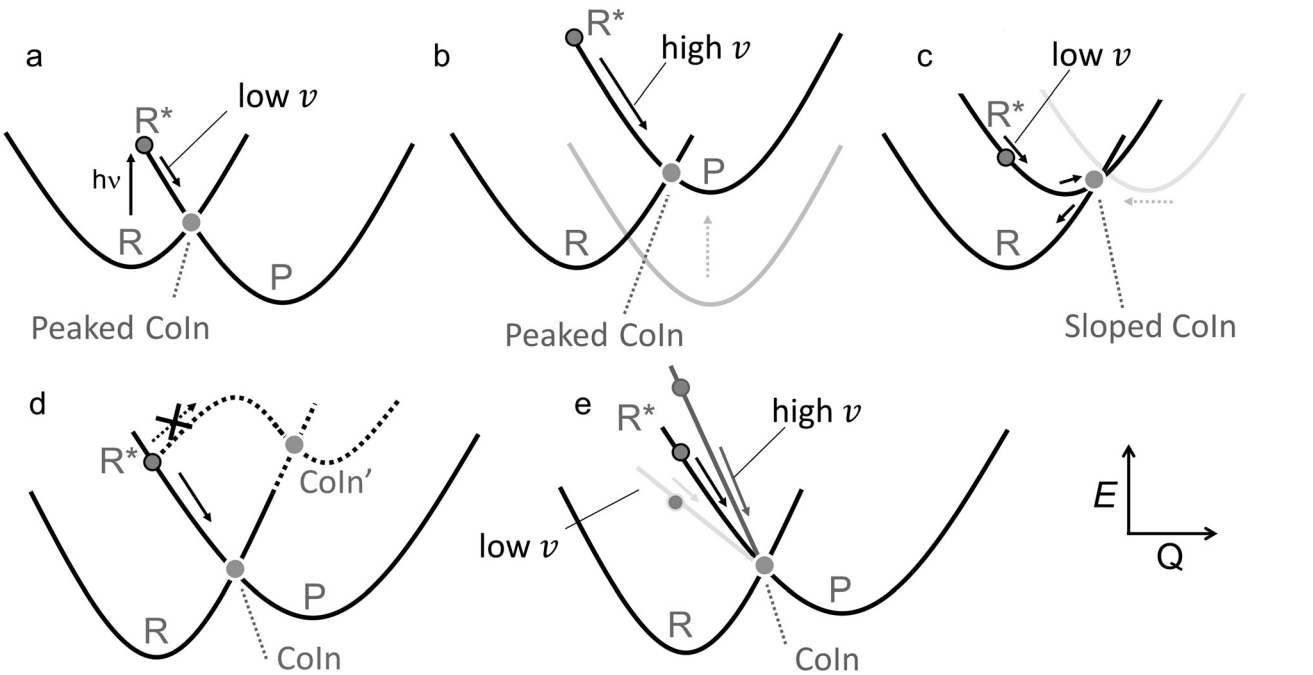

Fig. 9 Different CoIn and ES topographies, as classified in Table 1. Graphs a–d illustrate cases where the location and energy of the CoIn is modulated (factor IV), targeting mainly the nuclear velocity for graphs a–c and the entry direction for graph d. Graph e illustrates a case where the ES slope towards the CoIn is modulated (factor V), targeting the nuclear velocity. (a) peaked reactant-like CoIn. (b) Shifting the product parabola with respect to the reactant parabola up results in a peaked product-like CoIn. The relative position of the CoIn with respect to the FC-region (R*) results in different initial nuclear velocities and therefore product QY, as explained by the Hammond postulate. (c) Shifting the product parabola with respect to the reactant parabola to the left results in a sloped CoIn, demonstrating the intimate connection between factors IV and III. Note that sloped CoIns typically only result in regeneration of reactant. (d) the energetic position of CoIn with respect to CoIn' controls the direction of the photochemical path and therefore the type of CoIn (seam) that is approached. The energetic accessibility of the two CoIns may be controlled by an ES activation barrier (Fig. 5c), demonstrating the intimate connection between factors IV and I. This represents an important design rule for topographical substituent effects (Section 2.2) (e) an increasing ES slope results in higher nuclear velocity towards the CoIn, which may be caused by a protein environment (Section 3.1). The increasing ES slope may favor the entry direction towards one CoIn compared to another (Fig. 5e).

Such ES PES reshaping further from the CoIn is based on the gradient-directed effect, which implies that the excited molecule will follow the path of steepest descent.[20] ES slope tuning may be achieved through protein environment engineering, as suggested for the rPSB11 chromophore in rhodopsin (Section 3.1). According to the standard LZ model, steeper ES slopes and therefore higher nuclear velocities should result in higher photochemical QYs (see eqn (5) and related discussion).

2.1.6 Electronic mixing with higher states. Up until now all the topographical factors discussed inherently assumed a two-state model, whereas in practise there is always some degree of electronic mixing with a higher-lying electronic state. For instance, the photochemistry of butadiene (Scheme 3) and rhodopsin (below) involve a strong interplay of three electronic states, demonstrating again the more complicated nature of photochemical processes compared to thermal chemistry.

QM/MM based nonadiabatic nuclear trajectories demonstrated a key role for the protein environment in shaping the ES PES of rPSB11 (Fig. 10). In methanol solution the ES PES is relatively flat due to significant S_2/S_1 mixing, resulting in slow reaction dynamics *via* an energetically high CoIn.[99] Additionally, the flat ES PES reduces the coherence (both at the population and single-molecule level, Section 3.1.1), thus changing the entry direction. However, when rPSB11 is embedded in a protein environment, as in rhodopsin, the state mixing is reduced resulting in faster downhill progression through a lower-lying CoIn and eventually an ultrafast photoreaction. Additionally, the coherence on such a steep surface is preserved to a greater degree, increasing the velocity as well.[68] Interestingly, the state mixing in microbial rhodopsin is intermediate between these two situations, resulting in an intermediate ES lifetime. Even in the reference bovine rhodopsin and despite the diminished S_2/S_1 mixing due to the protein environment, there is still some degree of decoherence in the first few tens of femtoseconds as a result of the non-zero probability for wavepackets generated on the S_1 PES to be transferred to the S_2 PES (Section 3.1).[100]

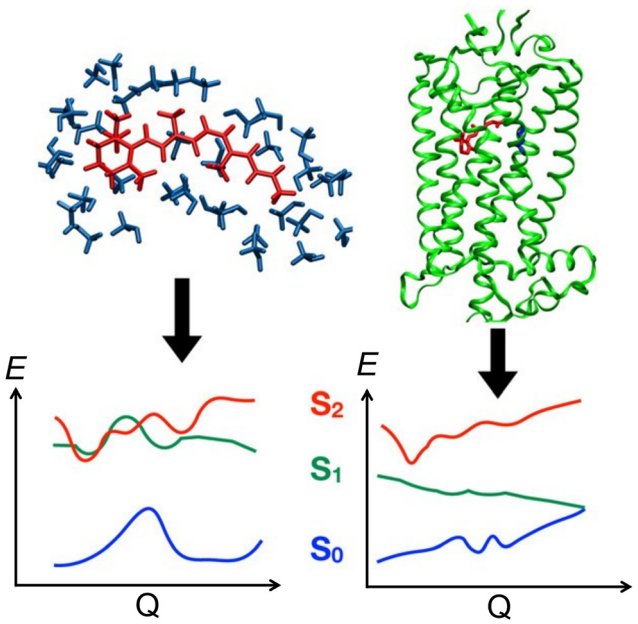

Fig. 10 Schematic S_2, S_1 and S_0 PESs for rPSB11 photoisomerization in methanol (left) and in an opsin environment (right).[99] In methanol solution the strong S_2/S_1 mixing results in flat ES PESs, which reduces the coherence and nuclear velocity. The opsin environment reduces this mixing significantly, resulting in steep ES slopes and therefore a high degree of coherence and a large nuclear velocity. Adapted with permission from ref. 99. Copyright 2017 American Chemical Society.

2.2 Effects of chemical substitution

Above we have seen that according to the LZ picture, ultrafast photochemistry is controlled by the direction and velocity with which the reacting system enters the BP of the CoIn that mediates decay to the GS. We have also seen that such direction/velocity can be affected by different topographies (factors I–VI, defined in Table 1) of the PES along the BP making the reactive event complex.

We now discuss the effect of chemical substitution on photochemical reactions by considering these topographical factors, still within the framework of decay at a single reference CoIn (*e.g.* a MECI). As the standard LZ model applies to regions only in the vicinity of the CoIn, we focus on chemical substituents that leave the spectroscopic properties of the chromophore largely unperturbed (*i.e.*, they will not alter the FC-state), but primarily alter the PES along the BP. While chemists often use chemical substitution as a strategy for controlling GS reactivity through modulation of an activation barrier (Fig. 5a), it is less obvious how to apply the same strategy to control reactivity in a (nonstatistical) photochemical process.[101] Topographical effects of CoIns caused by strong light-matter coupling in optical cavities are not discussed in this review paper, but have been demonstrated to significantly impact nonradiative decay rates[102] and singlet fission rates.[103]

Schuurman and Stolow distinguished between potential (meaning potential energy. However, in this text this is referred to as topographical for consistency purposes) and inertial substituent effects, where the first primarily controls branching of different ES reaction paths by tuning topographical factors (I–VI), and the second selectively alters the nuclear velocity of a relevant normal mode without modifying the PES topographies in the CoIn region.[20] The latter is achieved through addition of bulky substituents, such as methyl or *t*-Bu, which by first approximation leaves the electronic structure of the molecule, and therefore the force constant in the harmonic oscillator model, unperturbed. As we have discussed above, within the framework of the standard LZ model, an enhancement of nuclear velocity of the mode describing the reaction coordinate results in an enhanced decay probability and photoproduct formation. We will now see how certain substituent effects reveal a non-applicability of the one-mode mechanistic picture of ultrafast photochemical reactions defined above and, therefore, of the LZ treatment.

2.2.1 Functional group-based CoIn classification. We start by revising an approximate classification of a set of reported CoIns based on the organic functional group involved. In the

previous sections we have seen that the goal in investigating the structure of CoIns is to obtain information on the local reaction pathways characterized by the geometry of the MECI and topography of the ES and GS PESs along the BP. In the past, Bernardi, Olivucci and Robb described (mostly within a VB framework and, in many instances, with the help of a transformation of the CASSCF MO wavefunction into an Heitler-London VB wavefunction)[104] these features, as well as their connection to the electronic structure of the intersecting states, for a number of organic functional groups.[105] This work formed the classification of CoIns in four types: (1) three electron H_3-like triangle (2) *trans*-annular π-bonds (3) charge-transfer (CT) (4) n-π* re-coupling, to which we add another type, (5) n-σ* dissociation (Fig. 11).

Many of the CoIns discovered in organic photochemistry and characterized *via* the calculation of the MECI, BP vectors and local PES topographies may be assigned to these five types, yet some situations have been documented that reveal the limitations of such a classification. However, most reported CoIns are of type 1 and 3 and these types are therefore discussed in depth in the following. Fig. 11 displays, schematically, the S_1/S_0 MECI structures of all types, along with their equilibrium S_1 and S_0 geometries, as well as the type of photochemical reactions that they may control. The relevant geometrical rearrangements found in these MECI structures typically involve twisting, stretching and pyramidalization. The corresponding BP vectors are instead not discussed systematically here.

2.2.1.1 Type 1 CoIn. In this type the electronic structure is such that there are three weakly coupled unpaired electrons like in the well-known CoIn of H_3; an elementary CoIn that has the geometry of an equilateral triangle.[10,11,106] Therefore, in a molecule with an even number of "reacting" electrons, type 1 CoIn features a spectator unpaired electron that may be located in a fragment π-orbital. In butadiene the spectroscopically bright ππ* state (single HOMO → LUMO excitation of ^1B_u symmetry in MO language) is dominated by CT (closed-shell) character and is energetically slightly higher than the dark $(\pi\pi^*)^2$ state (multiconfigurational state of ^1A_g symmetry involving double HOMO → LUMO excitation, as well as HOMO−1 → LUMO and HOMO → LUMO+1 excitation) that is dominated by a covalent (diradical) character.[107–111] Therefore, after photoexcitation to the ππ* state, populating the $(\pi\pi^*)^2$ state through a $S_2(\pi\pi^*)/S_1(\pi\pi^*)^2$ CoIn is facile. As will be shown below, both $S_1(\pi\pi^*)^2/S_0$ and $S_1(\pi\pi^*)/S_0$ CoIns contribute to the ES decay dynamics of butadiene due to their energetic proximity. Focussing on the first for the moment, distinct spin pairing in the $(\pi\pi^*)^2$ state with respect to the GS facilitates a photochemical reaction. The $S_1(\pi\pi^*)^2/S_0$ CoIn then directs *via* the $\mathbf{Q}_1$ and $\mathbf{Q}_2$ vectors of the BP the repairing of the electron spins in a specific fashion that, in turn, determines which photoproducts will be formed. For example, BP vectors bringing two weakly interacting electrons located on different unbound carbon atoms of type 1 CoIn closer, could lead to spin pairing between these atoms, resulting in the formation of a cyclopropyl radical as a primary reactive photoproduct.[10] The $S_1(\pi\pi^*)^2/S_0$ type CoIn may lead to the simultaneous formation of two products (see Fig. 4 right) as it happens, for instance, in the case of hexatriene ring closure.[112] Type 1 CoIns control (electrocyclic) ring opening and closure reactions in polyene systems (Schemes 2 and 3) and nucleobases (Fig. 18, Section 3.3), as well as double bond

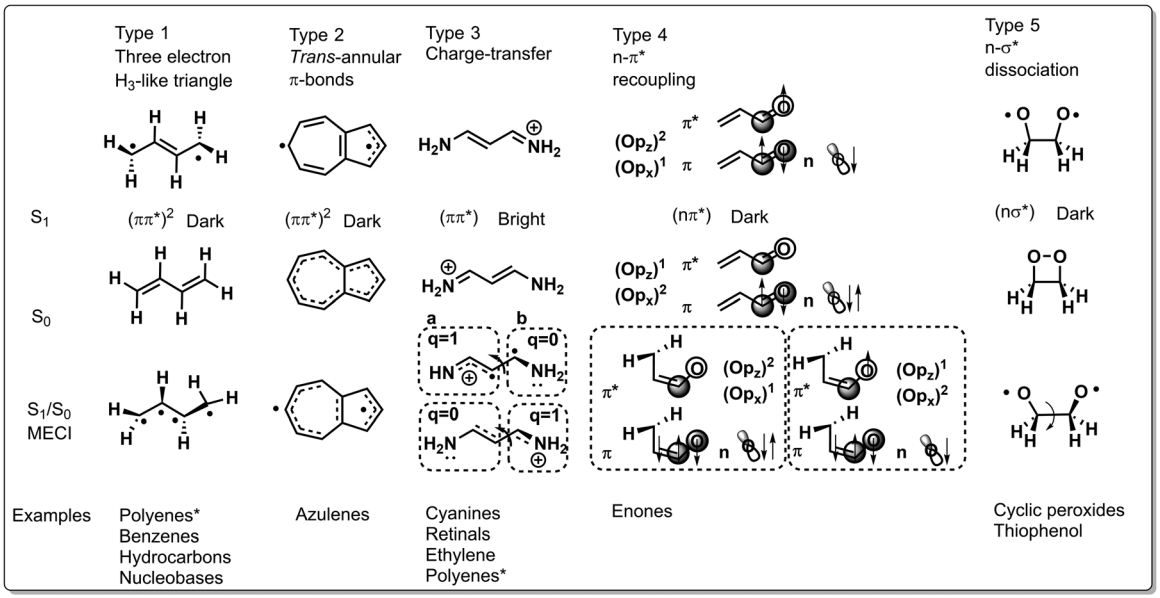

Fig. 11 Classification of CoIns into five types based on their electronic and geometrical structure. From top to bottom, the S_1 equilibrium, S_0 equilibrium and S_1/S_0 MECI structures are shown for each type. Note that this classification is approximate as not every reported CoIn can be included here, such as the π3s/ππ* CoIn in ethylene (Section 2.2.2). *Ordering of diradical and charge-transfer states is dependent on substitution pattern and alkene chain length.

photoisomerization reactions *via* a hula-twist mechanism, discovered in phytochromes and the green fluorescent protein (Section 3.2).

2.2.1.2 Type 2 CoIn. Due to the rigidity of azulenes in type 2 CoIns, the S_1/S_0 MECI is primarily characterized by stretching coordinates.[14] This CoIn may be rationalized by considering that S_1 is a biradical structure with a *trans*-annular π-bond, whereas S_0 only has a *trans*-annular σ-bond. Hence, compressing the S_0 equilibrium geometry along that bond lifts the S_0 PES, yet decreases the S_1 PES, reaching the S_1/S_0 MECI.

2.2.1.3 Type 3 CoIn. The photoisomerization of rPSB11,[113] related retinal chromophores[114] and cyanine dyes[115] are controlled by a type 3 CoIn, in which the lowest ES is a bright ππ* state (single HOMO → LUMO excitation) of CT character. The $S_1(\pi\pi^*)/S_0$ MECI of the latter will be discussed in detail. It appears around half-way through the isomerization coordinate, in which the two halves of the twisted molecule (indicated with fragment a and b in Fig. 11) differ by a charge of one electron. Hence, such a CoIn is similar to a twisted intramolecular charge transfer (TICT) state.[116] The degeneracy of the S_0 and S_1 states at this twisted geometry, and hence the occurrence of the CoIn, can be rationalized by their heterosymmetric biradicaloid nature.[90] The frontier π-orbitals at fragments a and b are weakly interacting and degenerate, which is why regardless of the location of the positive charge, the bottom and top resonance structures are energetically degenerate. Other than the extensively discussed double bond photoisomerization of rhodopsin (Fig. 10 and Section 3.1.2) and rhodopsin models (Fig. 8 and Section 3.1.4), type 3 CoIns control double bond photoisomerization of ethylene (Scheme 1), polyenes (Scheme 3) together with type 1 CoIns, the isolated chromophore of the green fluorescent protein (Fig. 17, Section 3.2), as well as the photochemistry of the ring-locked Me-FlOH, *N*-alkylated indanylidene–pyrroline biomimetic switch (Scheme 7, Section 3.2) and nucleobases (Fig. 18, Section 3.3).

2.2.1.4 Type 4 CoIn. The type 4 CoIn involves a $S_1(n\pi^*)/S_0$ CoIn, which is rationalized by the orbital occupation of n, π and π* and the associated atomic orbitals.[118] The in-plane Op_x (out-of-plane Op_z) orbital is doubly (singly) occupied in S_0, but becomes singly (doubly) occupied in $S_1(n\pi^*)$, which is a diradical state not due to a double excitation (as in Type 1 and 2) but due to the single occupation of two orthogonal atomic orbitals Op_x and Cp_z. These $(Op_z)^2(Op_x)^1$ and $(Op_z)^1(Op_x)^2$ configurations become degenerate when the carbonyl Cp_z is weakly interacting with Op_z, but strong with an adjacent carbon atom. The twisting of the terminal methylene group facilitates this stronger coupling between the two central carbon atoms, resulting in double-bond character. At the same time, this motion reduces the coupling with the carbonyl oxygen, resulting in a single bond. Type 4 CoIns control the photochemistry of α,β-enones (Fig. 12), involving double bond isomerization and electrocyclic ring-closure.

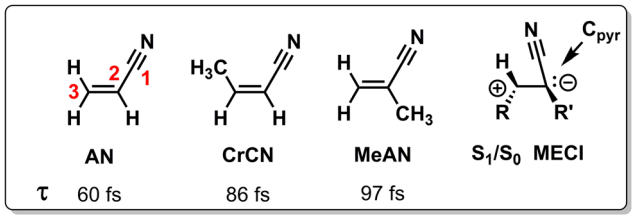

Scheme 1 Chemical structures of acrylonitrile (AN), *cis*-3-metharylonitrile (CrCN), *cis*-2-metharylonitrile (MeAN) and a schematic geometrical structure of the S_1/S_0 MECI. Also indicated are their ES lifetimes τ as measured with TRPES.[117]

2.2.1.5 Type 5 CoIn. Lastly, a type 5 CoIn occurs in molecules with low-lying nσ* states. Population of the antibonding σ* orbital results in a large degree of bond stretching, which is why photodissociation reactions are common for type 5 CoIns (see Scheme 5 and related discussion). Furthermore, type 5 CoIns have been identified in chemiluminescent reactions, where thermal decomposition of a strained ring results in an excited state species that luminesces.[119–122] For instance, the ring strain in 1,2-dioxetane causes significant O–O bond stretching, resulting in an energetically low-lying σ* orbital which may be populated by transferring an electron from an oxygen located n-orbital. Next to the O–O stretching motion creating a biradical, 1,2-dioxetane decomposition involves an asynchronous C–C stretch and O–C–C–O torsional motion as characterized by the $S_1(n\sigma^*)/S_0$ MECI.

2.2.2 Topographical effects of chemical substituents. The first example of rational design of CoIns is the methyl substitution on acrylonitrile (AN) at various positions (Scheme 1).[117] In this study, the lifetimes of several acrylonitrile derivates were measured with time-resolved photoelectron spectroscopy (TRPES) and their corresponding MECIs were computed with the CASPT2 method. Population of the $S_1(\pi\pi^*)$ state leads to an antibonding interaction between C2 and C3, inducing two main geometrical rearrangements: a twist around the central double bond followed by pyramidalization leading to a type 3 CoIn. The electronic properties of the CN group determine which carbon atom gets pyramidalized (*i.e.*, which carbon atom has the fastest pyramidalization motion), as it is best capable of stabilizing the associated negative charge of an adjacent pyramidalizing carbon atom. In fact, the calculations showed that all the MECIs corresponding to pyramidalization of C3 are about 1 eV higher in energy and are therefore less accessible from the FC-point, as illustrated by the dashed path to CoIn' in Fig. 9d.

Since the methyl group appears to be at the same carbon atom where the CN group is bound in MeAN, the pyramidalization motion is strongly hindered due to the destabilization of the forming lone pair (anionic centre) on that carbon, explaining the longer lifetime. This is a topographical effect and not an inertial effect as the relative energetic position of one CoIn is modulated, biasing the wavepacket towards one specific CoIn along the corresponding BP direction. In fact, one can assume that an inertial effect, due to the difference between the H and CH_3 masses, would not have a large effect on the pyramidalization at C3 when comparing the AN and MeAN cases, thus

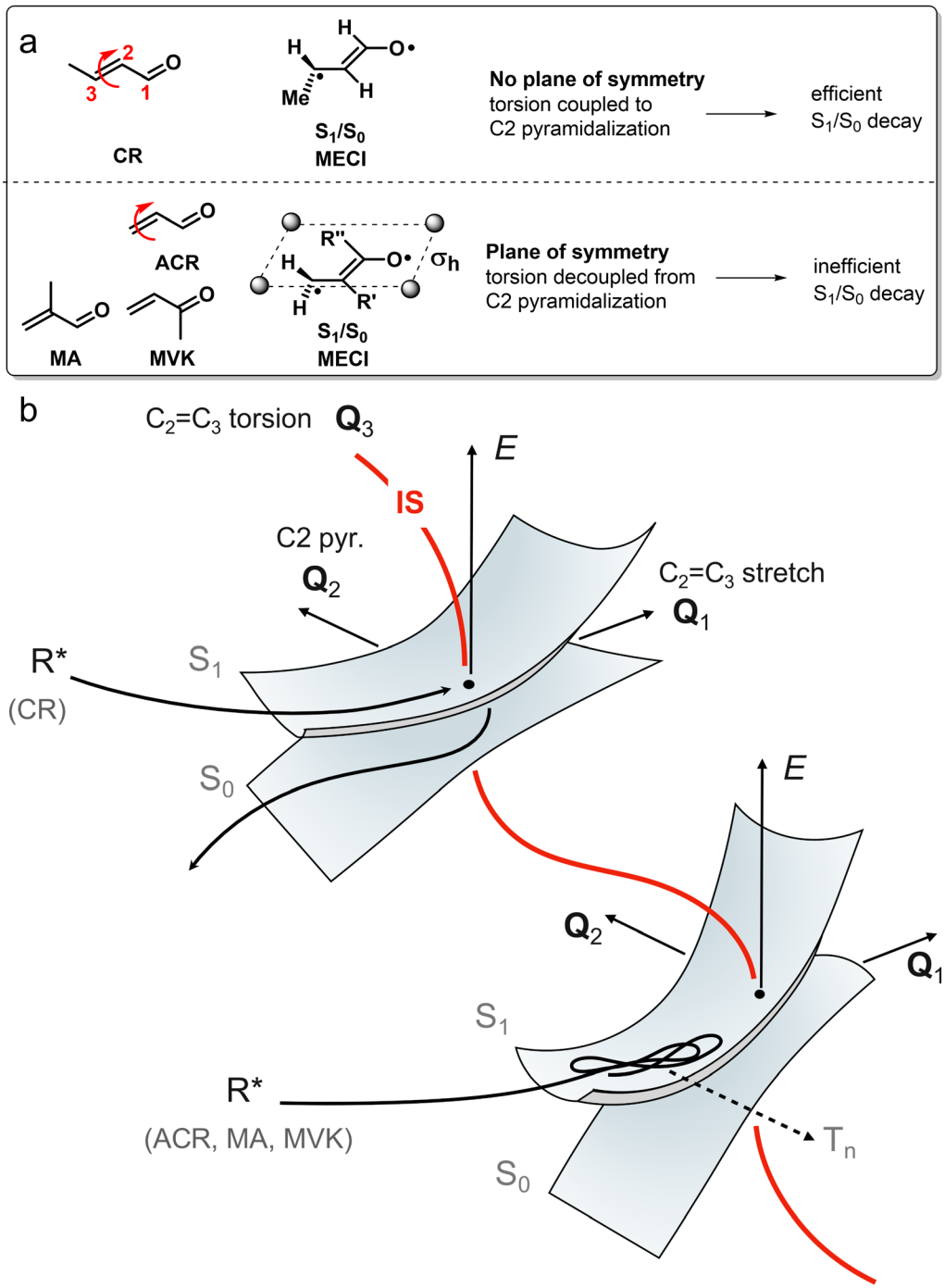

Fig. 12 Substitution effects on acrolein photochemistry. (a) Chemical structures of the acrolein derivatives studied: acrolein (ACR), crotonaldehyde (CR), methylvinylketone (MVK), methacrolein (MA). The red arrow indicates the torsional motion of the terminal methylene group. Schematic representations of CAS computed S_1/S_0 MECI geometries are shown as well. (b) Schematic $S_1(n\pi^*)$ and S_0 PESs showing the different reaction paths that the acrolein derivatives take after the sloped $S_1(n\pi^*)/S_0$ CoIn (type 4). Whereas CR undergoes efficient decay to the S_0 PES, ACR, MA and MVK stay on the S_1 PES which eventually results in triplet-state reactivity. The branching at $S_1(n\pi^*)/S_0$ is controlled by the degree of coupling between the torsional mode (which is part of the IS) and the $\mathbf{Q}_2$ mode. Since this coupling is largely absent in ACR, MA and MVK, nonadiabatic decay is inefficient, whereas the coupling is large in CR, resulting in efficient nonadiabatic decay to S_0.

resulting in similar lifetimes. Finally, the same topographical (substituent) effect is consistent with the standard LZ model as a decrease in nuclear velocity in the BP correlates to a less efficient decay.

A similar joint spectroscopy-theory study on methyl substituted ethylene derivatives showed how increasing substitution stabilized the Rydberg π3s state, resulting in an enhanced ES barrier to reach the π3s/ππ* CoIn, which is intrinsically not

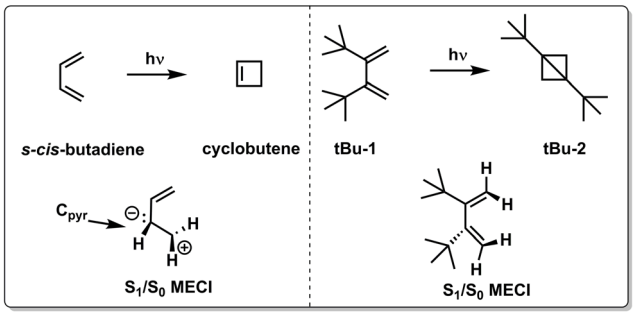

Scheme 2 Chemical structures and schematic geometrical structures of S_1/S_0 MECIs of reactants and photoproducts observed for the photochemistry of s-*cis*-butadiene and its di-*t*Bu substituted counterpart "*t*Bu-1".[123]

photoreactive, but populates the reactive ππ* state which dominates the photochemistry of short π-systems.[98] This would again be a topographical effect with a reaction scheme more similar to the one in the left diagram of Fig. 10.

Although the two examples above focus on how chemical substitution affects the nonradiative decay rate by topographical effects, chemical substitutions may also completely alter the photochemistry by enforcing nonradiative decay through alternative CoIns (see Fig. 5e and Scheme 2), as demonstrated by quantum chemical calculations on s-*cis*-butadiene derivatives. After photoexcitation to the spectroscopically bright $S_2(\pi\pi^*)$ state, both s-*cis*-butadiene and "*t*Bu-1" follow similar decay dynamics through a $S_2(\pi\pi^*)/S_1(\pi\pi^*)^2$ CoIn but follow different paths approaching the type 1 CoIn. Whereas the decay of $S_1(\pi\pi^*)^2$ in s-*cis*-butadiene is dominated by a fully asymmetric out-of-plane motion,[123] the bulky *t*Bu groups force (possibly also *via* an inertial effect, see below) a concerted synchronous conrotatory motion of the two terminal CH_2 groups that results in cyclopropane formation, followed by an additional ring closure yielding the extremely strained *t*Bu-2.[124] In another study, the photoisomerization dynamics and selectivity of s-*cis*-butadiene was investigated upon CF_3 substitution.[125]

Levine and Martinéz demonstrated the relevance of both type 1 (C2Tr) and type 3 (H1Br) CoIns in the ES dynamics of s-*trans*-butadiene using *Ab initio* Multiple Spawning (AIMS) simulations (Scheme 3).[126] Following advances in simulations of time-resolved X-ray absorption spectra capturing the evolving electronic wavefunction surrounding the IS,[127] Schuurman and co-workers showed a preference for decaying *via* the transoid C2Tr channel relative to the CT H1Br channel.[128] The branching between these two channels may be tuned by electronic tuning with the CN group (Fig. 5e).[129] Although it leaves the energy of the C2Tr MECI relatively unaltered, the energies of the CT type MECIs are significantly dependent on the position of the CN group, as determined by single-excitation multireference configuration interaction (MR-CIS) calculations. Similar to the acrylonitrile derivatives of Scheme 1, CN substitution favors pyramidalization at the substituted site in the corresponding MECI due to its stabilizing π-accepting character and presumably faster motion along the corresponding BP vectors. Simultaneously, the ES activation barrier for pyramidalization at C1 (C2) is significantly enhanced for 2-CNBD (1-CNBD). The position of the CN substituent therefore controls the entry direction of the CoIn. It is apparent that, in all examples above, the change in reactivity has been intrinsically interpreted in terms of a variation of the velocity (due to dominating topographic effects) along a single BP direction of a critical MECI and consistently with a LZ scheme.

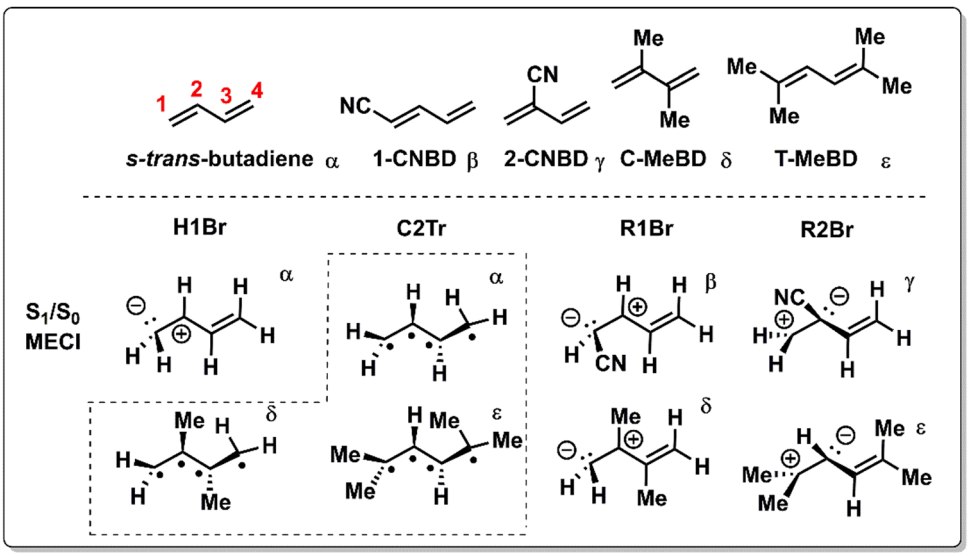

Scheme 3 Chemical structures and schematic geometrical structures of the S_1/S_0 MECIs for *trans*-butadiene, 1-cyano-1,3-butadiene (1-CNBD), 2-cyano-1,3-butadiene (2-CNBD), 2,3-dimethyl-1,3-butadiene (C-MeBD) and 2,5-dimethyl-2,4-hexadiene (T-MeBD). The H1Br, R1Br and R2Br names refer to the bridging of the H-1, R-1 and R-2 groups, respectively. These CoIns are of type 3 in Scheme 1. C2Tr refers to the transoid structure of the central C2 carbon and is a type 1 CoIn (Scheme 1). The Greek symbols are used to indicate which MECI geometries correspond to which molecule. All MECIs were calculated at the MR-CIS level of theory.[130]

2.2.3 Inertial effects of chemical substituents. Whereas CN substitution appears to mainly result in topographical effects, methyl substitution should result in dominating inertial effects. However, methyl substitution studies on s-*trans*-butadiene molecules (Scheme 3) demonstrated that the methyl group is not entirely ''topographically inert'', impacting non-radiative decay rates and branching ratios next to its inertial effect.[109,130,131] In fact, whereas the nonadiabatic decay from C-MeBD is dominated by a type 1 CoIn (C2Tr), T-MeBD has both contributions from a type 1 (C2Tr) and type 3 CoIn (R2Br), like s-*trans*-butadiene. To separate inertial from topographical effects, MacDonell *et al.* studied the ^{15}H substituted analogues of C-MeBD ($^{15}H_2$-BD) and T-MeBD ($^{15}H_4$-BD) with AIMS simulations, where ^{15}H is a theoretical substituent to mimic purely the inertial effect of a methyl group, having the same mass but not the electronic interactions of the methyl group.[130] Remarkably, a significantly different nonadiabatic decay distribution was discovered when comparing $^{15}H_4$-BD to $^{15}H_2$-BD. Moving the heavy ^{15}H substituents from the terminal C1 and C4 ($^{15}H_4$-BD) to C2 and C3 ($^{15}H_2$-BD) resulted in relatively more decay events through R1Br due to the increased pyramidalization velocity at C1. This trend caused by an inertial effect is continued when replacing the ^{15}H groups with methyl groups ($^{15}H_2$-BD to C-MeBD), in this case caused by a topographical effect. Through hyperconjugation the methyl group donates some π-electron density to the butadiene backbone, which destabilizes pyramidalization at C2, biasing the nonadiabatic decay distribution even more towards R1Br and away from C2Tr. Although these substituent effects clearly alter the dynamics in the vicinity of the CoIn, CASSCF calculations have shown that the methyl groups in C-MeBD also exert large inertial effects on the GS relaxation pathways after the CoIn (Section 2.1) by restricting the s-*cis* to s-*trans* motion on the GS surface,[82] resulting in larger QYs for cyclobutene formation.[132,133] Again, while the methyl substituent effects above have been described in terms of branching along different paths, the actual decay can still be interpreted in terms of a variation of the velocity along a single BP direction of a critical MECI.

The inertial effect of methyl groups has been applied to the photochemistry of α,β-enones as well, in which the position of a methyl substituent controls the velocity of the wavepacket through a sloped $S_1(n\pi^*)/S_0$ CoIn (Fig. 12) in acrolein derivatives.[85] The chemical structures of acrolein (ACR), as well as its substituted derivatives, crotonaldehyde (CR), methylvinylketone (MVK) and methacrolein (MA) are shown in Fig. 12a. The corresponding geometrical MECI structure is characterized by a double bond twist and pyramidalization and is of type 4 (Fig. 11). When the methyl group is positioned at the terminal carbon (C3), as in crotonaldehyde (CR), nonadiabatic decay is favored, resulting in either IC or singlet photochemistry. In contrast, having a methyl-free terminal methylene carbon (ACR, MA and MVK) results in less efficient decay to the GS PES, which extends the S_1 lifetime making these molecules more prone to undergo ISC to the T_n manifold, eventually yielding typical α,β-enone triplet state reactivity such as the Norrish type 1 reaction. The original rationalization for these differences in $S_1(n\pi^*)/S_0$ decay efficiencies was based on an inertial substituent effect of the terminal methyl group in CR, which induced (i) low $C_2{=}C_3$ torsional velocity (ii) high velocities along the BP (*i.e.* along $\mathbf{Q}_1$ and $\mathbf{Q}_2$). ACR, MA and MVK, on the other hand, have (i) high $C_2{=}C_3$ torsional velocity (ii) low $\mathbf{Q}_1$ and $\mathbf{Q}_2$ velocities. As the calculated $\mathbf{Q}_1$ and $\mathbf{Q}_2$ BP vectors correspond to $C_2{=}C_3$ stretching and C2 pyramidalization, according to this interpretation the torsional mode drives the wavepacket to a particular region along the IS that is, therefore, indirectly implied in the dynamics at the CoIn.[85] This provides a first example where, clearly the MECI and the motion along the corresponding BP are not sufficient to explain the experimental observations and an extra mode (locally an ''IS mode'') needs to be involved in the explanation (Fig. 12b). We reinterpret the distinct nonadiabatic decay behaviour of CR by noting that the large kinetic energy in the torsional motion picked up after $S_2(\pi\pi^*)$ excitation needs to be (partially) transferred to the C2 pyramidalization mode to facilitate the nonadiabatic transition from $S_1(n\pi^*)$ to S_0. This energy transfer should be facile in CR where the coupling between torsion and C2 pyramidalization is large due to the lack of symmetry at the S_1/S_0 MECI geometry. However, the S_1/S_0 MECI geometries for ACR, MA and MVK contain a plane of symmetry, which decouples the torsion from C2 pyramidalization, resulting in inefficient nonadiabatic decay to the S_0 PES as the $\mathbf{Q}_2$ mode is inactive. In conclusion, the coordinated interplay between torsional and pyramidalization normal modes is a manifestation of the multi-mode (*e.g.* one BP and one IS mode) nature of ultrafast photochemical reactions, which will be the topic of Section 3.

Because the torsional mode in the retinal chromophore of rhodopsin (rPSB11, Section 3.1) is a BP vector for its photoisomerization reaction through a type 3 CoIn and therefore directly involved in the efficiency of this nonadiabatic process, methyl substitution at the torsional skeleton should significantly slow down the reaction. Indeed, QM/MM simulations of a model all-*trans* retinal (rPSBAT) demonstrated how methyl substitution increased the ES lifetime, both in gas phase and non-polar solvents.[51] However, Kukura and co-workers experimentally found that photoisomerization of 10-methyl-rPSBAT (methylation at C10 in rPSBAT) in methanol is much faster than rPSBAT,[134] which has been verified using QM/MM simulations in both methanol[135,136] and in a protein environment[99] and was rationalized by a reduction in S_2/S_1 mixing resulting in steeper ES slopes (similar to the discussion related to Fig. 10), illustrating again that the methyl group is not a pure inertial substituent. Despite the faster ES decay (higher nuclear velocity), the isomerization QY is drastically smaller in 10-methyl-rPSBAT compared to rPSBAT, being inconsistent with the standard LZ model.[134] This result suggests that the actual reaction coordinate (presumably lying along the BP of the rPSBAT MECI), does not represent the real velocity direction at decay. In other words, a multi-mode mechanism also implicating motion with components along the IS must be considered. In Section 3 we will see that this is indeed the case.

Inertial tuning studies by methyl substitution have also been carried out on allene, where an increasing degree of methyl

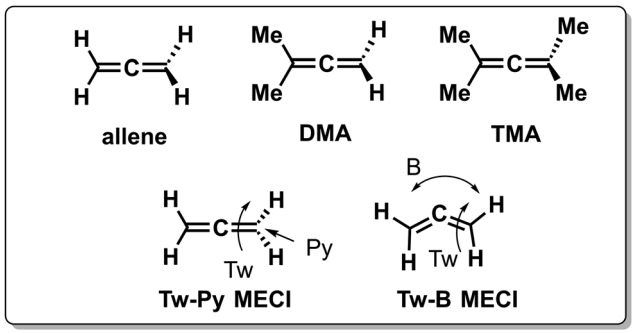

Scheme 4 Chemical structures of allene, 1,1-dimethyl-allene (DMA) and tetramethyl allene (TMA). Two relevant MECI geometries are shown at the bottom for allene, indicated with Tw-Py and Tw-B, the first one involving twisting (Tw) and pyramidalization (Py) motion, the second involving twisting and bending (B) motion.

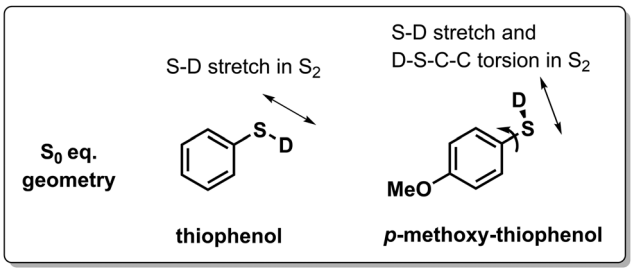

Scheme 5 Chemical structures of S_0 equilibrium geometries for deuterated thiophenol and para-methoxy substituted thiophenol. Arrows indicate the type of motion that is activated upon photoexcitation to the S_2 ($n\sigma^*$) state.

substitution correlated to longer TRPES measured ES lifetimes after $S_1(\pi\pi^*)$ excitation.[137] The distinct decay dynamics of these molecules has been rationalized with, again, a branching of two channels involving distinct $S_1(\pi\pi^*)/S_0$ MECIs, calculated at MR-FOCI level of theory (Scheme 4). Whereas decay through the Tw-Py MECI requires twisting and pyramidalization of one CH_2 unit (type 3 CoIn), the Tw-B requires twisting and bending of the C=C=C framework. AIMS simulations show that in all cases decay through the Tw-Py MECI is dominating. However, upon increasing methyl substitution the twisting motion is retarded, resulting in a greater propensity for C=C=C bending as mixing of the two π-bonds is weak in a weakly twisted geometry, which decreases the probability to reach the low-lying Tw-Py MECI. As decay through the Tw-B MECI is not efficient, the lifetime is extended significantly upon methyl substitution. This case appears to be consistent with the standard LZ model as the nonadiabatic decay efficiency decreases with a slower twisting motion approaching the MECI. Finally, increasing the bulkiness of substituents at the 5-position in cyclopentadiene rings leads to longer lifetimes as the vibrational dynamics relevant for ultrafast nonadiabatic decay were inhibited.[138]

Another strategy to tune the photochemical dynamics was carried out by Lim *et al.* who exploited the differences in GS conformational preferences between thiophenol and methoxy-substituted thiophenol (Scheme 5) to alter the ES wavepacket trajectories and consequently the S–D photodissociation rate by exciting the S_2 ($n\sigma^*$) state with short laser pulses.[139] In thiophenol, the equilibrium geometry is such that the S–D bond is coplanar with the phenyl ring, which results only in a S–D stretching motion upon photoexcitation. The wavepacket dynamics upon S_2 excitation is different when a methoxy group is added at the para position, since the S_0 equilibrium geometry becomes perpendicular, whereas the S_2 equilibrium geometry remains planar. This activates C–C–S–D torsional motion on the ES PES, next to the S–D stretch, which broadens the distribution of velocities (*i.e.* less coherence) on the ES PES, increasing the chance for the wavepacket to miss the (planar) $S_2(n\sigma^*)/S_0$ type 5 CoIn and consequently results in a less efficient nonadiabatic decay. Here a single MECI and BP picture is valid as the efficiency of photodissociation through the $S_2(n\sigma^*)/S_0$ CoIn decreases with a decrease in the nuclear velocity along the BP direction of a MECI.

2.2.4 Automated computational screening and design. Due to the complexity of ultrafast photochemical reactions and the multitude of topographical and dynamical factors involved, rational design approaches to tune photochemical reactions are not always fruitful. For this reason, methods with automated protocols are presently being developed and benchmarked in the computational photochemistry community. This has led to improved QM/MM models for the electronic structure of rhodopsin[140] and the discovery of previously unknown CoIns in the photochemistry of benzene.[58] Similarly, machine-learning based approaches have the potential to predict photochemical reactions by calculating the PESs and nonadiabatic couplings with much higher efficiencies.[141,142] However, these approaches currently still suffer from several drawbacks including the requirement of large datasets.[143] Even the description of a few PESs in small molecular systems rely on thousands of data points, limiting the application of machine-learning based nonadiabatic MD simulations to molecules with fewer than 12 atoms.[144,145] Another bottleneck is related to the limitations in transferability as most machine-learning models are molecule-specific.[146,147] An elaborate discussion about these methods and their challenges is out of the scope of this review.

In the nonadiabatic nanoreactor method developed by Martínez and co-workers, vast regions of the IS are explored and the BP vectors for many relevant CoIns are sampled.[58] From this study it has become clear that even for a simple molecule such as benzene, a complete characterization of its photochemistry involves the computation of different IS segments, each having distinct CoIn topographies and photoproduct distributions that are intimately linked to its topography as well as the position of the CoIn along the IS. We anticipate that such a method will be crucial for the discovery of multi-mode photochemical reaction mechanisms where, in general, it is insufficient to assume a single CoIn and BP to explain the photochemical QY. However, we acknowledge that currently the computational cost

associated with a nanoreactor hampers its application to larger molecules than benzene. Furthermore, although the nanoreactor characterizes the IS completely with CoIn-specific photoproduct distributions, it does not provide the total photochemical QY for a given set of initial conditions. The latter may, however, be computed using a swarm of nonadiabatic nuclear trajectories without the need for a complete IS characterization.[148–151]

2.3 Limitations of the standard LZ model

In the context of the "standard" model discussed above where decay at a single CoIn channel dominates, a key prediction is that a larger velocity towards the CoIn correlates with a higher QY, which is often reinterpreted in terms of the existence of an inverse relation between ES lifetime and QY. Such relationship has been investigated multiple times with both computational and spectroscopic approaches[70,71,73,74,152] and it has been an inspiration for almost all the rational design approaches to photochemical reactivity discussed in the present section. Although those approaches have often succeeded in changing the ES lifetime (related to the reaction or relaxation velocity), a discussion of their effect on QYs has often been omitted. Here a remarkable feature is that an opposite correlation has been found in a number of both computational and experimental studies, *i.e.*, longer ES lifetimes correlate with higher QYs.[153–156] One paper in particular, reporting on quantum-classical dynamics simulations for a series of rhodopsin proteins, found that the longest ES lifetime (visual rhodopsin) displayed the largest photoisomerization QY as well (Fig. 13).[156] In an experimental pump-probe study, Cheminal *et al.* measured an isomerization rate of 100 fs for a rPSB isomer present in Anabaena Sensory Rhodopsin, yet with a relatively low QY below 0.25.[154]

These failures of the standard LZ model imply that consideration of a single reactive mode, usually a torsional mode for double bond photoisomerization, is not sufficient. In all the above cases, the mechanistic principle generating such critical mode, and the nuclear velocity along such mode, has not been discussed. Most specifically, no attention has been paid to the fact that qualitatively different velocities (*e.g.* velocities with opposite sign) or spectrum of velocities could be generated during a coherent ES progression and due to established phase

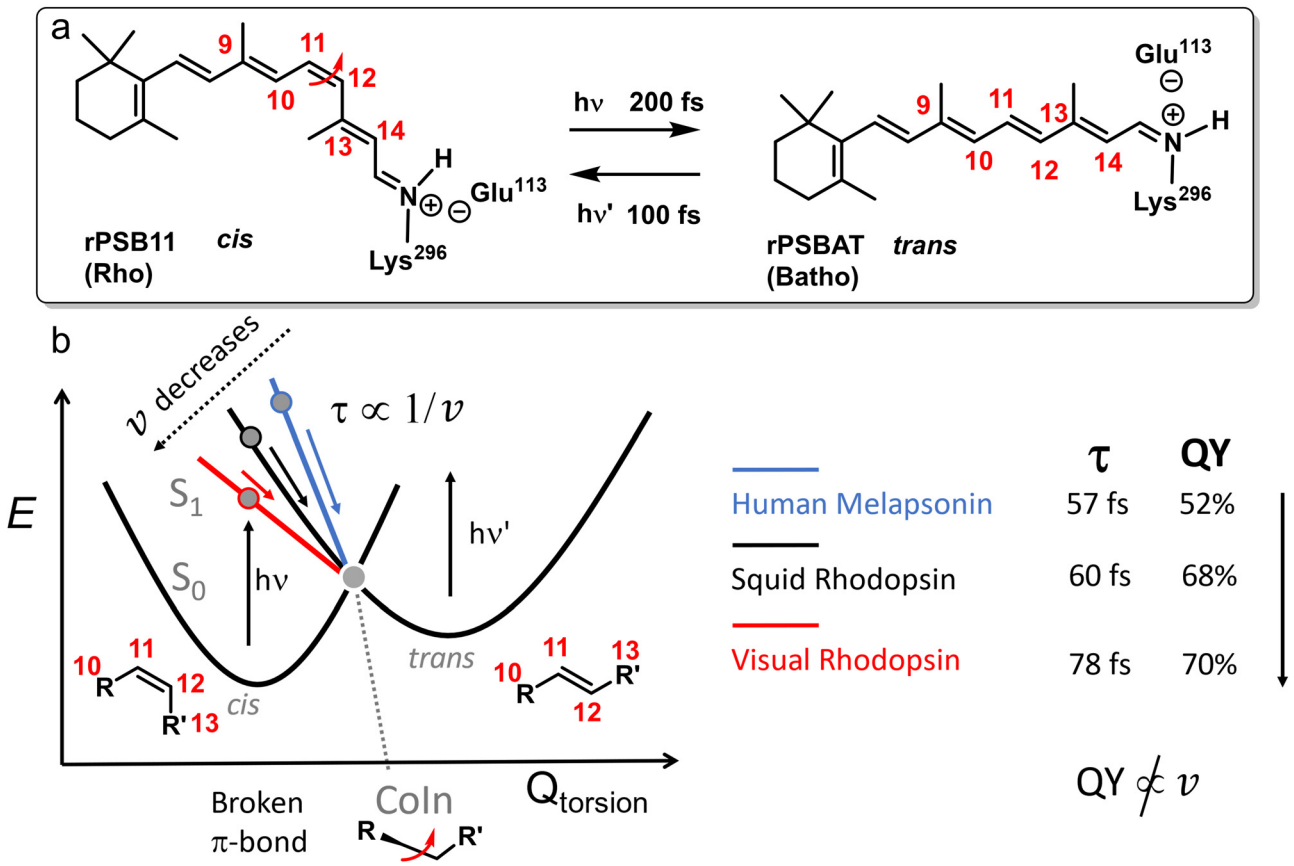

Fig. 13 (a) Photoisomerization of 11-*cis* retinal protonated Schiff Base (rPSB11) at the C_{11}=C_{12} bond to its corresponding all-*trans* form (rPSBAT). (b) A schematic one-mode representation of this reaction along the torsional coordinate, passing through a CoIn where the π-bond is broken. The ES lifetimes τ (inversely proportional to the reaction speed, ν) of various rPSB11 isomerization reactions in different protein environments are proportional to the isomerization QY, which is in contrast with the LZ model (Section 2). As experimental τ and QYs are not available for all systems, the computationally acquired values are shown.[156] Note that the ES lifetime is not equal to the total reaction time, which includes relaxation on the GS PES. The trend in ν is caused by different protein environments, corresponding to different ES forces exerted on the torsional mode.

relationships between modes initially orthogonal to the putative nuclear reaction coordinate. This makes the qualitative interpretation of the LZ theory effectively depending on the interplay between different modes prior to decay. However, notice that, in principle, this interplay is automatically accounted for in numerical simulations based on the propagation of classical trajectories with surface hopping,[157,158] such as the Landau–Zener surface hopping method,[159] or other methods based on nonadiabatic dynamics theory.[160] Despite this, the mechanistic principle resulting from LZ theory applied to a decay event intercepting a single CoIn along one direction with a specific velocity (*i.e.* the standard LZ model and the corresponding direct proportionality between the velocity of that mode and the decay efficiency) is still often applied without recognition of the interplay between multiple modes. The impact of such an interplay between modes is that not a single CoIn channel drives nonadiabatic decay, but multiple CoIn points from the reactive IS segment (Fig. 5f), each with a distinct direction and phase relationship between the relevant BP and IS modes.

Indeed, the experimental and computational observations on the acrolein derivatives discussed in Section 2.2 already suggest that the coupling between BP modes and IS modes is important for controlling nonadiabatic decay. This coupling may be readily reinterpreted as a need to consider decay at multiple CoIn points along the IS. The demand for a multi-mode understanding of photochemical reactions is further reinforced by experimental evidence from two-dimensional spectroscopy[161] and coherent control laser spectroscopy.[162] In the latter, shaped laser pulses were used to control the isomerization QY of rPSB11 through constructive and destructive interference of vibrational modes that are relevant for the reaction on the timescale of coherent chemistry, *i.e.*, before vibrational relaxation.

It should be noted that there are additional limitations to LZ theory and the standard model. One assumption of the standard LZ model that might fail in realistic circumstances is the conservation of vibrational coherence (*i.e.*, in the sense that all molecules of the same population would move along the same reaction coordinate on similar timescales). It is likely that there will always be some vibrational redistribution, which can alter the dynamics.[71] Other simplifications inherent to LZ theory that more advanced methods should deal with are the constant slope difference (F) and constant velocity (v) near the CoIn. Additionally, whereas passage of a wavepacket exactly through a CoIn would lead to a 100% efficient nonadiabatic decay according to the LZ formula, wider regions around the CoIn may be implicated in the decay.[163] This is because nonadiabatic transfer of wavepackets may be achieved even though the wavepacket does not travel exactly through the CoIn, as shown by Farfan and Turner with quantum dynamics simulations[164] and also stressed above when discussing the AC surrounding a real crossing point. Lastly, LZ theory does not consider the potential importance of Berry's phase effects which include modifications of the nuclear forces driving the nonadiabatic dynamics.[165]

3. Beyond the standard Landau–Zener model: vibrational motion in concert and the role of the intersection space

This section discusses the need of a different approach towards understanding what factors control the quantum yield (QY) in certain ultrafast photochemical processes. As anticipated in previous sections, in these cases a mechanism centred on a single MECI and BP has to be abandoned, as considering the decay along an entire IS segment becomes critical, leading to difficulties in correlating measured velocities (*e.g.* estimated *via* ES lifetimes) and QYs as indicated by the one-mode Landau–Zener (LZ) model.[60,62] Indeed, both spectroscopic and computational results acquired in the last 10 years indicate that for a proper description of ultrafast photochemistry, it is crucial to incorporate in the ES progression towards the IS: (i) modes that do not belong to (or have a limited projection on) the BP of a single critical CoIn and (ii) the phase relationship between these modes. Below we discuss several case studies illustrating these concepts.

3.1 Ultrafast double bond photoisomerization of rhodopsin

Double bond photoisomerization of rhodopsin, the first step in dim-light vision, has been the guinea pig to demonstrate the importance of the relative phase of vibrational modes in controlling the branching ratio at the CoIn. This discovery is based on three pillars, being the spectroscopic observation of vibrational coherence (VC) throughout the complete reaction pathway (I), computational insights into the coordinated interplay of the vibrational modes describing the progression towards the IS (II) and confirmation of such a multi-mode mechanism through the vibrational phase isotope effect (III).

Before we discuss these pillars, we summarize some relevant characteristics of the photochemistry of rPSB11 and rPSBAT, which are the chromophores of the rhodopsin (Rho) and bathorhodopsin (Batho), respectively (Fig. 13). The discovery that photoisomerization of rPSB11 takes place through a CoIn instead of an AC is connected to the wide variety of CoIns detected in common organic photochemical reactions.[10,19,105,114,166] Furthermore, a barrierless reaction path connects the FC-point to a CoIn whose local topography is peaked and is therefore a great example of the elementary photochemical reaction we set out in Fig. 5b.[114] Since this reaction completes in 200 fs, it is considered to be ultrafast.[167] The gradient of the S_1 PES drives the breaking of the π-bond between the C11 and C12 atoms, leading to an about 90° twisted type 3-like (Section 2.2) CoIn structure. However, it will become clear in this section that this reaction coordinate is not solely composed of a torsional deformation of the reacting double bond but includes other molecular modes as well.

3.1.1 Vibrational coherence. One of the first key spectroscopic studies that demonstrated the ultrafast and vibrationally coherent nature of rPSB11 photoisomerization, was performed by Wang *et al.*[73] In these pump–probe experiments, vibrational oscillations superimposed on the photoproduct

absorption kinetics were detected (Fig. 14a), which after subtraction of the electronic decay component followed by Fourier-transformation provided the Raman frequency content of those oscillations, corresponding to torsional modes of the photoproduct. In modern literature, such a time-domain Raman experiment is referred to as either impulsive stimulated Raman spectroscopy (ISRS)[168] or impulsive vibrational spectroscopy (IVS).[169] The reader is referred to those references for experimental details.

A key component of these experiments is the use of temporally compressed laser pulses, which can excite multiple vibrational eigenstates in the ES due to its large bandwidth. An ultrashort light pulse excitation projects the GS vibrational eigenfunctions onto the ES PES to generate a wavepacket with the same shape, provided that this pulse is temporally shorter than the vibrational periods of interest (pulses <10 fs are required to observe most vibrations of interest up to ~ 3000 cm^{-1}).[172] This FC excitation is the vibrational equivalent of an equilibrium structure vertical excitation and the region where the wavepacket is localized in configuration-space is called the FC-region. Because the wavepacket created on the ES PES is not a vibrational eigenstate anymore (in fact, the pump prepares a superposition of vibrational eigenstates), it will evolve in time according to the shape of the ES PES. From a classical point of view, this may be understood by considering that at the FC-point specific modes in the ES are displaced with respect to the GS and therefore experience a force by the ES PES, resulting in a time evolution described by Newton-like equations.[173] One important experimental consideration is that through the ISRS mechanism, VC is also created on the GS surface. Whenever it is not possible to spectrally resolve the contributions from excited and ground state, more sophisticated pulse schemes might be employed as described in ref. 168 and 174.

The initially created ES population or wavepacket is vibrationally coherent (*i.e.*, it displays the VC property) in two forms. One is the synchronized motion of molecules at the population

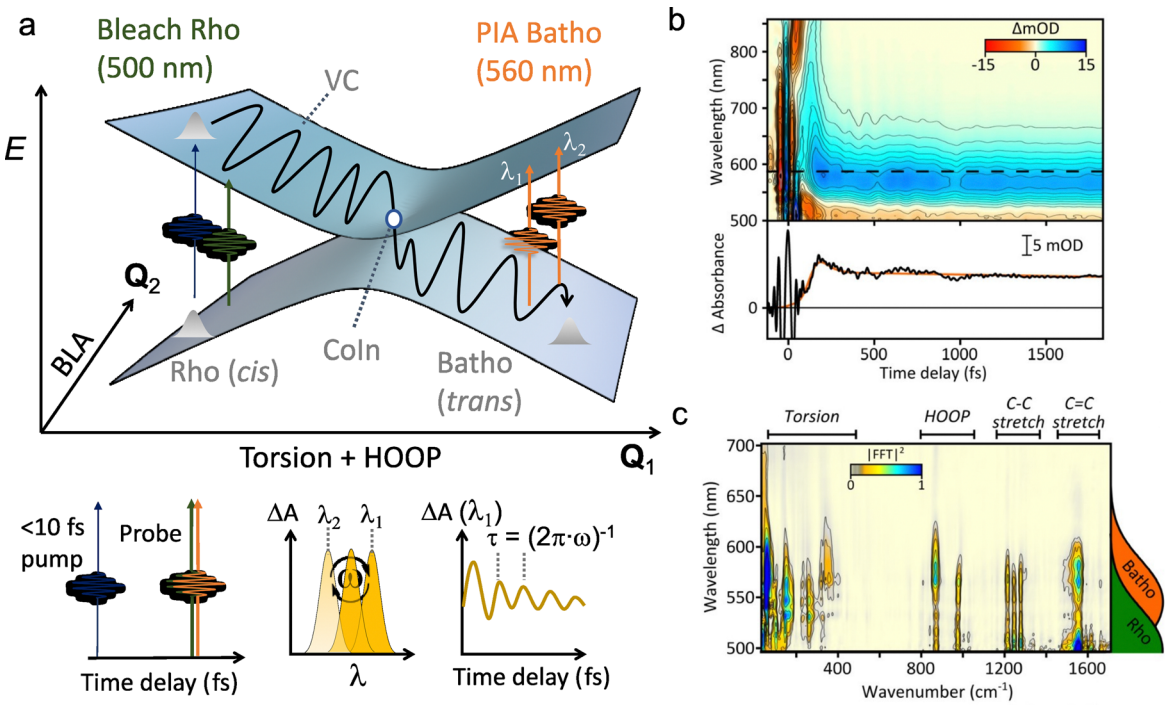

Fig. 14 Elucidating the mechanism of ultrafast multi-mode rPSB11 (Rhodopsin) photoisomerization to rPSBAT (Bathorhodopsin) with impulsive vibrational spectroscopy (IVS). (a) An ultrashort (<10 fs) laser pump pulse (blue arrow) generates VC on the ES PES, which is probed over time. The green arrow indicates the probe wavelength with which the GS bleach, *i.e.*, reduction in absorbance, of rPSB11 is detected. The photoinduced absorption (PIA) of the photoproduct Batho is indicated with the orange arrow. The differential absorption ΔA (or ΔOD) spectrum is modulated by a frequency ω that is determined by the relevant normal modes. This is illustrated for the PIA of Batho in the bottom schemes, where the intensity at the probe wavelengths λ_1 and λ_2 changes over time. The vibrational oscillations superimposed on the electronic kinetics become clear when the ΔA is probed at one wavelength λ_1 (see bottom right). Notice that in this schematic the wavepacket passes through only one point in the IS, which is not necessarily the MECI. (b) Differential absorption ΔA map of photoexcited rhodopsin with a 8 fs pump pulse at 500 nm. The dashed line at 560 nm indicates the maximum absorbance peak of the PIA, forming on a sub-200 fs timescale. The inset below shows the slice of the ΔA at this probe wavelength, which exhibits vibrational oscillations on top of the electronic kinetics. Reproduced from ref. 170 with permission. Copyright 2015 American Chemical Society. (c) Wavelength resolved Fourier power map obtained after subtraction of the electronic kinetics by global analysis, followed by fast Fourier transformation. The vibrational coherence (VC) observed in the ΔA map is composed of torsional (<400 cm^{-1}), HOOP (800–1000 cm^{-1}), C–C stretch (1200–1300 cm^{-1}) and C=C stretch (1500–1600 cm^{-1}) modes. The latter two are also collectively referred to as bond length alternation (BLA). These modes are included in the mechanistic drawing in (a) and visualised in Fig. 15. Although the IVS study suggested the HOOP mode to be the coupling mode (the equivalent of the $\mathbf{Q}_2$ mode),[170] CASPT2 calculations show that the BLA mode corresponds to $\mathbf{Q}_2$.[152,171] Reproduced from ref. 170 with permission. Copyright 2015 American Chemical Society.

level caused by the specific shape of the ES PES (*i.e.*, by the ES force field), or intermolecular VC. Thus, this coherence corresponds to a dynamical behaviour purely in a classical sense.[175] One consequence of such state is that, at the single molecule level, VC implies a specific phase relationships between two or multiple normal modes and can be called intramolecular VC. Conservation of VC throughout any photoinduced process implies the conservation of this phase relationship. Decoherence, on the other hand, implies partial randomization of vibrational energy amongst all normal modes, as well as dephasing of the initially vibrationally phased motion. As demonstrated in Fig. 14, VC manifests itself as a time-dependent modulation of a (photoinduced) transient transmission (recorded by a broadband probe pulse) with a frequency determined by the energy differences between the excited vibrational eigenstates, hence providing a spectroscopic marker to study structural dynamics in the ES.[169]

Based on the torsional intramolecular VC experimentally observed in the photoproduct, the extremely high reaction speed (200 fs) and the lack of fluorescence, Wang *et al.* concluded that rPSB11 photoisomerization in rhodopsin involves a CoIn (type a photochemical reaction in Fig. 1), which has been verified by subsequent studies.[28] When using the vibronic picture given by Fermi's Golden Rule, the CoIn strongly couples the ES vibrational eigenfunctions to those of the GS, which (i) provides an efficient funnel back to the GS, explaining the ultrafast (200 fs) reaction speed (which Fermi's Golden Rule can't quantitatively account for, being limited to small perturbations only) and (ii) rationalizes the survival of ES PES induced VC created at the FC-point throughout the complete reaction path.[73,176] Indeed, neither the adiabatic photoreaction (type c) nor the nonadiabatic photoreaction *via* a AC (type b) complement these observations, as these would involve a (partially) equilibrated ES intermediate.

Kukura and co-workers revealed many other mode-specific VCs in the photoproduct (Fig. 14c), including the FC-active (*i.e.*, displaced on the ES PES with respect to the GS PES) bond-length alternation (BLA) and hydrogen out-of-plane (HOOP) modes (see below).[170,177] In fact, the torsional mode VC is indirectly activated through energy transfer from FC-active modes and is therefore reaction-induced (see below). Further support for a vibrationally coherent CoIn driven mechanism was provided by the transient grating experiments from Miller and colleagues.[178]

The above results suggest a coherent picture not only at the population level, but also at the single molecule level in which the temporally vibrationally phased motion of multiple modes directs the molecule to the IS with the correct trajectory in phase-space, facilitating an efficient nonadiabatic transition directed towards the product.[152] Accordingly, because the initial phase-space trajectory involves the cooperative motion of multiple modes, and because such motion is determined by the slopes of the ES at the FC-point, rational design of CoIns to control the velocity and QY of a photoreaction should take into account the phase relationship of the relevant normal mode basis.[179,180] During these studies the researchers were thinking of a rather compact propagating ES population maintaining such compactness while heading to a single favoured CoIn region (notice the single CoIn point in Fig. 14a). Below we will see that a partial decoherence of the population may cause decay at geometrically different CoIns of an IS segment, each CoIn point being associated with different phase relationships between critical modes.

3.1.2 Cooperative motion of three vibrational modes. From the previous subsection it is clear that the first step in vision is a vibrationally coherent ultrafast process. Additionally, the relevance of a specific set of normal modes has been illustrated, although it has not been clarified yet how exactly these normal modes affect the reaction outcome. This subsection will show computational results that support an ES progression involving three relevant normal modes. The interplay between these modes determines both the ES decay, as well as the stereochemical reaction outcome, *i.e.*, the *trans* : *cis* ratio.

The initial vibrational dynamics of excited rPSB11 is dominated by the bond length alternation (BLA) mode which is quantified by the difference between the average double-bond lengths and the average of the single-bond lengths of the conjugated chain. This initial relaxing motion can be rationalized by considering the CT nature of the S_1 wavefunction, which shows a positive charge build-up at the β-ionone fragment (Fig. 15a), resulting in a driving force to unlock the double bonds and lock single bonds.[113] As a result of this bond length inversion, a torsional mode about the $C_{11}{=}C_{12}$ bond becomes facile, which is accompanied by a torsional motion along the adjacent $C_9{=}C_{10}$ bond.[114,181] This volume-conserving mechanism was referred to as the bicycle-pedal mechanism by Warshel and is able to explain how an isomerization can take place within a tight protein cavity.[182] However, this motion is aborted after decay to the GS, ensuring that only isomerization at the $C_{11}{=}C_{12}$ double bond takes place, as was confirmed by CASSCF-based QM/MM calculations.[181,183]

Up until the early 2000s, this two-state two-mode mechanism involving the torsion that follows the BLA was considered to be the mechanism for the photoisomerization of rPSB11.[184] In fact, this was found to correspond to motion along the BP of a single MECI point. Only when quantum-classical trajectories computed using a complete QM/MM model of rhodopsin and an *ab initio* multiconfigurational wavefunction (Fig. 15b), became computationally feasible, the relevance of the HOOP mode (Fig. 15c) in the coherent photochemical reaction was recognized.[113,185] The HOOP motion that appears to be primarily one of the IS coordinates at the MECI, provides a measure of the pyramidalization at the C11 and C12 atoms, reflecting their sp^3 character. Both the BLA and HOOP modes facilitate the breaking of the π-bond, even before the torsional mode is activated. Consistent with previous calculations, the first 5 fs of the quantum-classical trajectories are dominated by BLA motion (Fig. 15b). The HOOP motion becomes active after 15 fs when the BLA mode has almost finished a quarter of an oscillation and shows a periodic oscillation in the HOOP-torsion subspace throughout the complete trajectory approaching the CoIn (grey line), which implies the presence of a phase

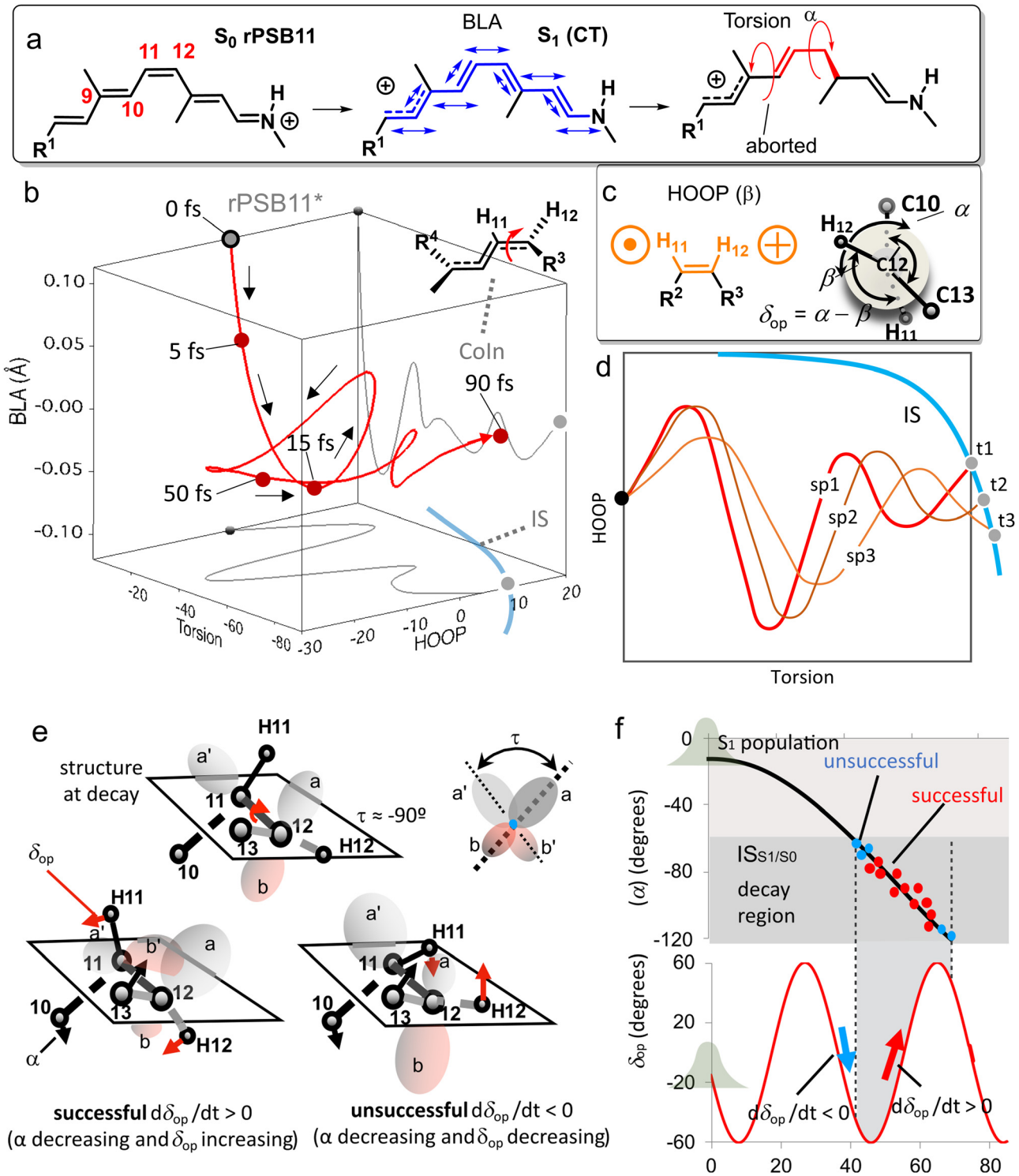

Fig. 15 Mechanism of rPSB11 to rPSBAT photoisomerization. (a) Two-state two-mode model. Initial charge redistribution upon photoexcitation is accompanied by bond-length alternation (BLA) and followed by the torsional bicycle pedal motion. (b) QM/MM ES trajectory displaying the center of a coherent wavepacket (red line) is described by three relevant normal modes: BLA, torsion and HOOP. The geometrical CoIn structure is shown at the top right. The grey curves are the projection of the red trajectory on two normal mode coordinates. The dashed curve is the projection of the IS on the torsion-HOOP subspace. Adapted with permission from ref. 113. Copyright 2017 American Chemical Society. (c) Definition of HOOP mode (β) and δ_{op}. Relative motion of HOOP with respect to the torsion (α) is indicated with δ_{op}. (d) Schematic illustration of the effect of partial decoherence on the phase relationship between HOOP and Torsion. As also detailed in ref. 100, this process can be described as the splitting of the initial populations (*e.g.* sp1 to sp3) each reaching the IS at different times (*e.g.* t_1 to t_3). As a result, different populations decay with different phase relationships between HOOP and torsion. (e) Relation between relative phase HOOP and torsion modes and orbital overlap required for π-bond reconstitution at decay point, represented by the CoIn structure on the top right where τ indicates the dihedral angle between the bisectors a and a′ ($\sim -90^\circ$ at CoIn). a + b and a′+ b′ indicate the phases of the p-orbitals at the two central

carbon atoms, C12 and C11, respectively. Successful isomerization is achieved with out-of-phase motion of δ_{op} and α through overlap of the a and b′ lobes to form the *trans* π-bond, whereas in-phase-motion prompts unsuccessful isomerization through orbital overlap between the a and a′ lobes which forms the *cis* π-bond. (f) S_1 wavepacket trajectory, represented by a Boltzmann population, evolving coherently along α and δ_{op} coordinates. Most successful decay events (*i.e.* the largest isomerization QY) are achieved when $d\delta_{op}/dt > 0$, whereas unsuccessful decay events occur when $d\delta_{op}/dt < 0$.[100,113]

relationship between these two modes. Albeit less perfect, such a periodic oscillation mixes with motion along the BLA-torsion subspace as well, clearly hinting towards a two-state three-mode mechanism (*i.e.* implicating both the BP and the IS). Although there appears to be a sequential activation of these normal modes, which is due to the shape of the ES PES, the periodicity of these two bimodal subspaces during the trajectory is striking. Apparently, the FC-active BLA mode transfers its energy to the torsional and HOOP modes, presumably through anharmonic coupling. Such an anharmonic coupling-driven activation of FC-inactive modes was also observed as a reaction-induced VC in the ES dynamics of bacteriorhodopsin by comparison of IVS and resonant Raman spectroscopy, in which the first probes any ES active mode, whereas the latter only probes FC-active modes.[186] What these quantum-classical trajectories thus show is that not only the ES PES force field may generate VC (since the initial conditions are according to Boltzmann statistics the role of femtosecond pulses is ruled out), but also conserve it, as the wavepacket moves through the $(3N-8)$-dimensional IS. The geometrical structure of the CoIn reached in ~90 fs[187] (*i.e.* different from the MECI) is schematically shown at the top right in Fig. 15b and shows pyramidalization at C12, along with torsional and stretching deformations with respect to the FC-point, showing clear type 3 CoIn characteristics (Section 2.2). It should be pointed out here that the red trajectory represents the center of a wavepacket, hence assuming VC at the population level. However, multiple trajectories leading to the photoproduct are possible. Furthermore, the CoIn structure shown in Fig. 15b only corresponds to a CoIn point, which is part of an IS. Indeed, multiconfigurational quantum chemical calculations show that multiple CoIn points associated with the same IS may be approached.[113] Hence, the ES decay does not follow a single pathway, but rather follows a variety of trajectories that may proceed through different CoIn points belonging to the same wide, in terms of C_{11}═C_{12} torsion (~60° variation),[100] IS segment.[188] This explains the HOOP deformation featured by the CoIn point of Fig. 15b and it shows that the trajectories lead to CoIn points where the HOOP mode is now mixed with the torsional mode yielding a local BP oriented differently from the BP at the MECI (see Fig. 3b for a schematic illustration).

The above process may be interpreted in terms of the widening of an initially narrow wavepacket during the ES propagation, caused by partial vibrational decoherence. This process would then lead to different population fractions (or subpopulations) decaying at different times at different CoIns along the IS (see Fig. 15d). Each subpopulation will then decay with a different phase relationship between the HOOP mode and the torsion.

Now that it has been established that three modes are involved in the ES decay of rPSB11, the next goal is to understand how they control the QY and the stereochemical outcome. According to the standard LZ model, a higher velocity of a single reaction coordinate on the S_1 PES towards the CoIn would correlate with a higher QY.[61] However, the results described above, along with the discussion in Section 2.3, strongly hint towards a multi-mode explanation that can also be interpreted, as mentioned above, in terms of variations in the $\mathbf{Q}_1$ and $\mathbf{Q}_2$ BP vectors at the "'reactive" IS segment.[154,189] Different combinations of the C_{11}═C_{12} torsion and HOOP motion correspond to the $\mathbf{Q}_1$ vector (the opposite combination will instead move the molecule along the IS),[1] whereas a BLA mode remains the $\mathbf{Q}_2$ vector.[171]

To understand how these modes work cooperatively to control the branching between the *trans*-photoproduct (rPSBAT) and the *cis*-reactant (rPSB11) and therefore the QY, it is important to understand the mechanism of π-bond reconstitution. In Fig. 15e, it is shown how the relative motion of the HOOP (β) compared to the torsional mode (α) controls the *cis*/*trans* isomer ratio starting from a structure similar to the CoIn which can originate from both the forward as well as the reverse photoisomerization direction.[113] An out-of-phase motion ($d\delta_{op}/dt > 0$, in which δ_{op} is equal to α–β) leads to a–b′ and b–a′ orbital overlap, resulting in successful isomerization (*i.e.* the *trans*-product), whereas an in-phase motion ($d\delta_{op}/dt < 0$) leads to a–a′ and b–b′ orbital overlap and therefore an unsuccessful isomerization (*i.e.* the *cis*-reactant). These two contrasting situations are also illustrated in Fig. 15f, where photoexcitation to the S_1 state generates a wavepacket that coherently evolves with a decreasing α and approaches the $IS_{S1/S0}$ with a distribution of δ_{op} values and an α value of roughly −90°. Successful isomerizations (indicated with red dots) require a HOOP motion with positive velocity while α is becoming more negative. In contrast, unsuccessful isomerizations occur when the HOOP motion is also becoming more negative, *i.e.*, in-phase with the torsional motion. Computational support for this HOOP-phase control was acquired by artificially delaying the HOOP mode by decreasing either its frequency or phase, which indeed resulted in smaller QYs.[113] Furthermore, other nonadiabatic molecular dynamics studies of rhodopsin have confirmed that the phase of the HOOP motion is crucial in determining the reaction outcome.[181,188,190,191] Again, this dependency on the phase of the HOOP component of the motion leading to decay can also be interpreted in terms of subpopulations decaying at different locations along the IS, each location reached at different times as illustrated in Fig. 15d. A recent computational study demonstrated this concept, showing the effect of the degree of decoherence acquired by the population during ES propagation on the decay dynamics and QY.[100]

Although it has been mentioned already that the BLA mode initially drives the wavepacket out of the FC-region, we now

clarify its role in driving the photoreaction in the CoIn region. Immediately after decay at the CoIn, the BLA mode determines whether the GS wavefunction will be of diradical/covalent (diabatic) character and therefore suitable for double bond reconstitution, or of unbound CT character.[113] In the forward direction (rPSB11 to rPSBAT), the wavefunction switches to a bonding diradical character only 20 fs after decay to S_0, allowing the HOOP motion to perform half an extra oscillation. At this point, the HOOP motion is out-of-phase with the torsional motion, yielding predominantly rPSBAT. In the reverse direction (rPSBAT to rPSB11) the wavefunction switches to bonding character near the CoIn and therefore the HOOP-phase control is already exerted much closer to where nonadiabatic decay occurs. The critical role of the relative HOOP phase could potentially enable a HOOP-phase driven approach to improve QYs by either tuning the HOOP frequency or phase through protein environment engineering, either retarding or speeding up the HOOP motion relative to the torsional motion, provided that the change of the HOOP amplitude is fast compared to the change in torsion.[152] Another way to change the relative phase of the HOOP and torsional modes and thereby the QY is to fix the HOOP frequency, but vary the torsional frequency. In fact, it is likely that in nature the relative nuclear velocity of the torsional mode is varied in different rhodopsins, resulting in a variety of QYs amongst these proteins.[152] While this appears a viable modulation effect implemented by the natural selection, in the next subsection we will see that in the lab it has been possible to modulate QY by changing the HOOP frequency. A major takeaway is that QYs can be improved by tuning the relative phase and/or frequency of normal modes. Therefore, any rational design method that aims to optimize QYs in ultrafast photochemical processes, should consider the engineering of VC effects. It should be mentioned that the degree of VC itself also influences the QY, as was already mentioned in Section 2.[192,193]

In the current analysis the contribution of the S_2 state has been disregarded, whereas recent mixed quantum-classical simulations of rhodopsin indicate that S_2/S_1 mixing, governed by opsin electrostatic interactions, in fact results in population splitting on a 10–30 fs timescale.[100] Such an event can be viewed as a partial vibrational decoherence resulting in a widening of the relaxing ES population in terms of temporal width. As a result, the isomerization QY is the sum of the fractional contributions from different subpopulations that pass the $IS_{S1/S0}$ at different times (see Fig. 15d and f), due to the different dynamics at the $IS_{S2/S1}$. Even though the S_2 state is involved in the initial relaxation dynamics and the decoherence that results from the population splitting, the S_1 PES topography and the associated vibrational phase matching rules that follow on a 30–150 fs timescale still determine the *cis*:*trans* branching at the $IS_{S1/S0}$ as illustrated in Fig. 15e. Nevertheless, the impact of the S_2 state on the isomerization QY once more illustrates the general complexity of ultrafast photochemical reactions, as the inclusion of another electronic state opens a variety of additional reaction pathways of which their vibrational dynamics should also be considered.

3.1.3 Vibrational phase isotope effect. The HOOP frequency and phase changes discussed in the previous section, imposed by hypothetical changes in the protein environment surrounding rPSB11, were computationally shown to affect the photoisomerization QY. As proposed by Schapiro *et al.*, this offers a method to rationally design photochemical reactions by tuning the relative phase of relevant normal modes.[113] Experimental evidence of such tuning was acquired in 2018, where a team of Olivucci, Kukura, Mathies and colleagues showed that by deuterium substitution, the phase relationship between the HOOP motion and the reactive torsional motion could be altered, increasing or decreasing the QY depending on the substitution pattern.[194] They used the term vibrational phase isotope effect to describe this phenomenon. This subsection will elaborate on this effect and discuss its importance for controlling ultrafast photochemistry.

By synthetizing several deuterium-substituted rPSB11 analogues (Scheme 6) and regenerating these chromophores in the opsin protein, followed by spectroscopic measurements to track the QY and isomerization kinetics, they were able to study the effect of isotopic substitution on the photochemistry of retinal. Whereas the effects on the QY were great, the effects on the isomerization kinetics were relatively minor. Both the QYs of 11-D and 12-D decreased significantly (0.45 and 0.48 respectively), whereas the QY of 11,12-D_2 was even slightly improved (0.69) compared to native rhodopsin (0.63). Traditional secondary kinetic isotope effects cannot explain this trend, as deuterium substitution would then lead to a decrease in reaction rate. Additionally, from a simple LZ model, for instance considering a reaction coordinate dominated by a single torsional (or mixed torsional/HOOP) mode, it would be expected that the HOOP motion would be retarded significantly

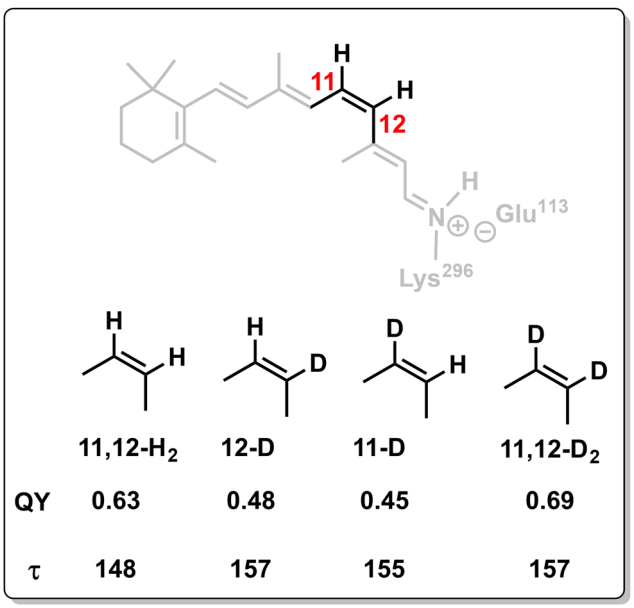

Scheme 6 QY and τ (lag time, time to reach the CoIn from the FC-point) values for different isotopomers of rPSB11.[194]

upon deuterium substitution, decreasing the nonadiabatic transition probability and QY.

Supported by nonadiabatic trajectory calculations, these substitution trends were explained by an intramolecular vibrationally coherent mechanism that involves a correctly phased motion of α (C_{10}–C_{11}–C_{12}–C_{13} torsion) and δ_{op} (H–C_{11}=C_{12}–H HOOP) at the CoIn. As was explained by Schapiro *et al.*, it is the timing of the two motions at the point where the wavefunction switches from antibonding to the bonding status that controls the stereochemical outcome.[113] Whereas the substitution has a minor effect on the torsional mode, since the torsion is predominantly localized on the carbon skeletal framework, it exhibits a greater effect on the HOOP motion.[190,195] As it is mainly the torsional mode that drives the wavepacket through the CoIn, modest changes in the reaction rate are observed. Although changes in the HOOP motion do not affect the reaction rate significantly, they do affect the branching ratio at the CoIn (Fig. 15e). This is because in 11,12-H_2 and 11,12-D_2, the C_{11}-H/D and C_{12}-H/D out-of-plane motions are coupled, resulting in symmetric and anti-symmetric HOOP vibrations, which maintain a certain phase relationship with the torsional motion. Interestingly, it appears that the double deuterium substitution results in an even improved phase matching as demonstrated by its higher QY. In contrast, partial deuteration reduces the vibrational coupling, leading to more isolated C–H and C–D out-of-plane motions and consequently less symmetric and anti-symmetric HOOP motion, which has been measured using resonance Raman spectroscopy.[196] This in turn leads to a poorer phase matching with the torsional mode, inhibiting photoproduct formation. Furthermore, nonadiabatic trajectory calculations revealed that the partially deuterated 11-D and 12-D chromophores were more sensitive to the initial velocities than their symmetrically substituted counterparts, as was shown by their more de-phased HOOP motion and hence smaller VC.[194] In contrast, the 11,12-H_2 and 11,12-D_2 chromophores displayed nonadiabatic trajectory dynamics that were relatively independent of the initial conditions, demonstrating that the ES topography rather than initial velocities dominate their ES evolution.

As these QY measurements were performed with incoherent light sources, the impact of VCs at the single-molecule level and its application in real-life systems irrespective of light conditions is confirmed. Furthermore, the nonadiabatic trajectory calculations with several initial Boltzmann conditions reproduce the QY trend in isotopic substitution, even though in the femtosecond laser experiments a specific vibrational wavepacket is prepared. Both the spectroscopic and quantum chemical results discussed in the current section therefore point towards a fully vibrationally coherent mechanism of rhodopsin photoisomerization, which strongly relies on a coordinated interplay of HOOP and torsion modes at the CoIn (Fig. 16).[197]

3.1.4 Rhodopsin models. The high QY of the photoisomerization of rPSB11 in rhodopsin has been attributed to a correctly phased-matched HOOP and torsional motion.[113] The surrounding opsin protein is crucial in shaping the S_1 PES and

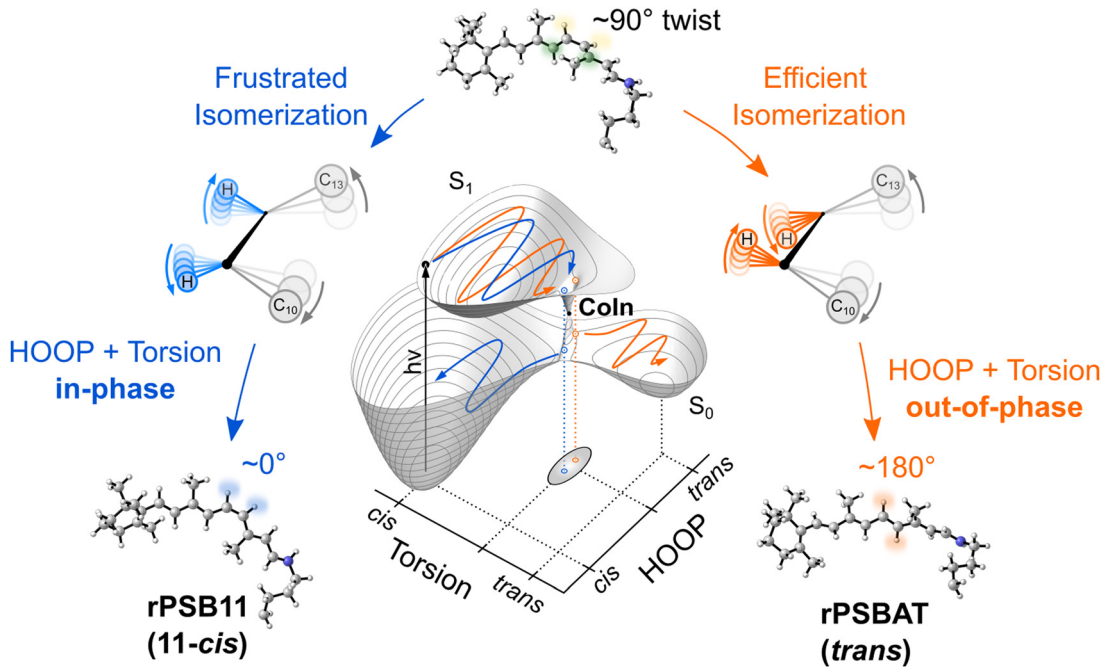

Fig. 16 Vibrationally coherent and ultrafast rhodopsin photoisomerization. Compared with the one-mode representation of Fig. 14, this multi-mode model includes both the torsional and HOOP modes (Fig. 15). After photoexcitation of rPSB11 (11-*cis*) to the FC-point on the S_1 PES, the coordinated motion of these modes with conserved relative phases guides the wavepacket to the CoIn, where the torsional angle is approximately 90°. The dynamical phase relationship of these modes controls the branching at the CoIn. Efficient isomerization to the all-*trans* product (rPSBAT) relies on an out-of-phase mode relationship (orange path). An in-phase relationship, however, results in frustrated isomerization, yielding the reactant 11-*cis*. Adapted with permission from ref. 197.[197]

therefore the relative phase of these two modes. Changes in the protein environment are therefore expected to alter the QY significantly. One way that this can be mimicked is through the application of external forces at specific parts of a molecule. This strategy has been explored by Valentini *et al.* who studied the rPSBAT to rPSB11 photoisomerization using a reduced model with nonadiabatic trajectory simulations (Scheme 7).[198] When pulling forces (see F_{ext} in the scheme) were applied axially to the terminal groups, the QY of C_2═C_3 isomerization was enhanced, which is counterintuitive since the product is a more compressed molecule. The explanation provided involved the relative phase of the torsional motions of the C_1–C_2–C_3–C_4 and H–C_2–C_3–Me dihedral angles that was modulated by this mechanical force. Specifically, the force can be tuned such that motion of these torsional coordinates at the nonadiabatic decay point is in-phase, favoring the branching at the MECI towards the product.

Another clear manifestation of the phase matching rule was discovered in the 13-*cis* (rPSB13) to all-*trans* photoisomerization of Channelrhodopsin 2, which is a protein widely applied in optogenetics (this is a microbial rhodopsin with an ion-gating function, but here we discuss it as a rhodopsin analogue).[199] Based on nonadiabatic molecular dynamics simulations, a positive (negative) HOOP velocity at the nonadiabatic decay event correlated to the *trans* (*cis*) isomer. A similar QY was found for a mutant protein that changes the electrostatic environment of the rPSB13 chromophore significantly. In contrast with the standard LZ model, a longer lifetime was found in the mutant, which was explained by the introduction of an ES barrier prior to the CoIn (see Fig. 5c).

Filatov *et al.* studied a rPSBAT model using direct nonadiabatic dynamics, confirming the role of relative phase in controlling the QY.[200] In short, they pointed out that the QY for the photoisomerization at the central C_2═C_3 bond is not only controlled by the HOOP motion, but also by its synchronization with two lower frequency modes, being a C–C torsional mode and a scissoring (bending) mode of the allyl and vinylamine moieties around the C_2═C_3 bond. More specifically, anti-synchronization between the scissoring mode and the $\mathbf{Q}_2$ vector, which is a combination of the C–C torsion and HOOP, results in a higher isomerization QY at the C_2═C_3 bond. In contrast, when the trajectories are less synchronized, a greater propensity for the backward direction (IC) was observed. CASSCF nonadiabatic molecular dynamics calculations on a similar model compound show consistency with these results, highlighting the synchronization of HOOP and torsion for controlling the QY.[201,202]

In a different and more simplified rPSB model (Scheme 7), Vukovic *et al.* showed with nonadiabatic dynamics how the photochemistry of double bond isomerization could be controlled by predistorting certain dihedral angles.[203] The cooperative motion of the corresponding torsional modes was shown to be a prerequisite for forcing a double bond isomerization at a N═C_1 bond instead of a C_2═C_3 bond. The protein environment controls the isomerization QY by imposing different predistortions, resulting in different torsional velocities due to the modified ES slopes. As the torsional modes are distorted to different extents their phase relationships are altered.[69,204]

The importance of the coupling between the HOOP mode and the torsional mode was highlighted by Bovee-Geurts *et al.*

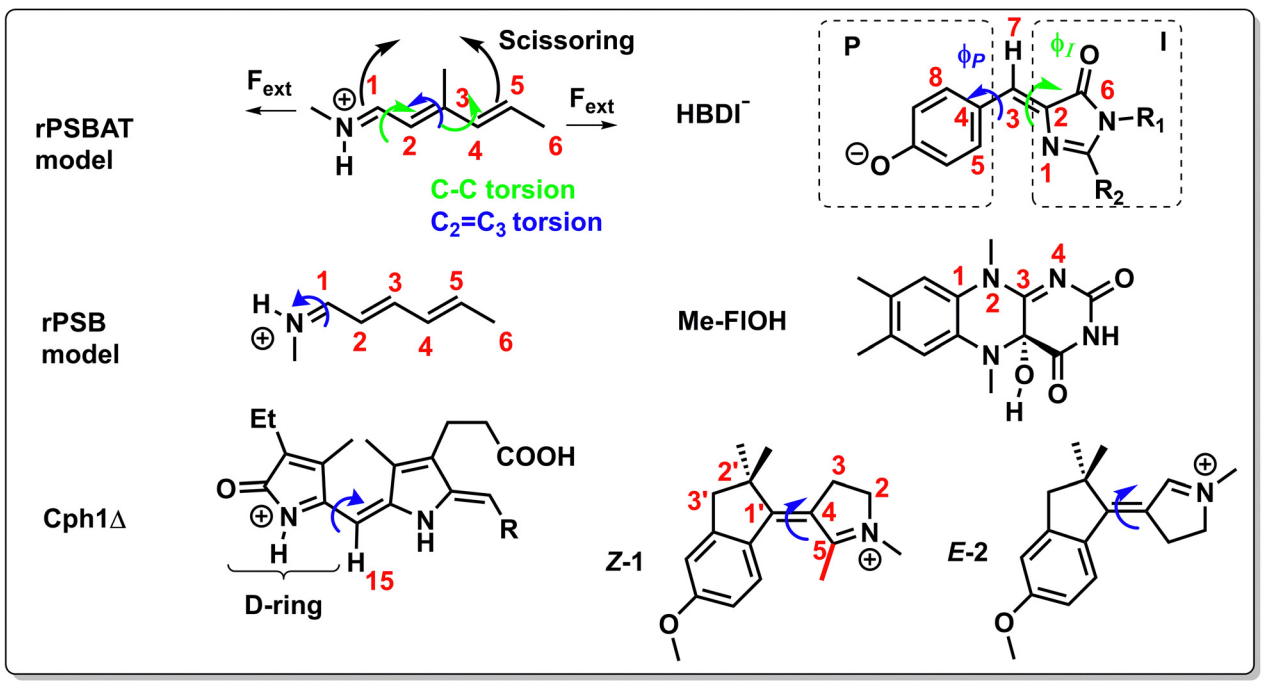

Scheme 7 Chemical structures of chromophores and molecular switches discussed in Sections 3.1.4 and 3.2. The blue and green arrows indicate relevant single or double bond rotations. The black arrows in the upper left structure indicate a scissoring mode.

in their Fourier-Transform Infrared study on several analogues of rhodopsin and isorhodopsin, which incorporates the *cis*-double bond at the 9-position instead of the 11-position.[205] The smaller QY of isorhodopsin (0.26) compared to rhodopsin (0.67) was explained by the distortion of the HOOP mode and consequently poorer coupling to the torsional mode. Interestingly, this coupling was improved again by introduction of a cyclopropyl group at the 9-position in isorhodopsin, resulting in a higher QY (0.39).

3.2 Other ultrafast double bond photoisomerizations

Ultrafast double bond photoisomerizations appear in a wide variety of both biological and artificial molecular systems. This section demonstrates how mechanistic details acquired for rhodopsin photoisomerization, which we outlined in the previous section, apply to other systems as well.

The ES VCs that were spectroscopically observed throughout the ultrafast (175 fs) *E* to *Z* photoisomerization of the truncated Cph1Δ form of phytochrome Cph1 (Scheme 7, *E* is shown) suggest that a phase relationship between modes that facilitate the nonadiabatic transition is conserved.[206] Furthermore, one of these oscillations was assigned to a retinal-like HOOP (H15) motion, whereas another has been inconclusively assigned to a D-ring torsional rotation.[207] In addition, these modes were assigned to $\mathbf{Q}_2$ and $\mathbf{Q}_1$, respectively. Despite these observations, it is not clear yet how the isomerization QY (0.10) is controlled by the relative phase of these modes. This will need to be addressed in the future.

The hula-twist mechanism for double bond photoisomerization provides another example where the cooperative motion of multiple modes (concerted single-bond and double bond rotation) drives photochemical reactions and has been observed in vitamin D, polyenes and stilbene, all involving a type 1 CoIn.[107,208–210] Given the type of molecular skeleton of the chromophore and the protein constraints a hula-twist mechanism (aborted or not aborted) may also operate in phytochromes. Additionally, such a mechanism has been discussed in the family of green fluorescent proteins (GFPs),[211] which act as a live-cell fluorescent imaging tool to monitor cellular processes,[40] although involving an electronically distinct $S_1(\pi\pi^*)/S_0$ CoIn due to the CT nature of the ES (*i.e.* a type 3 CoIn). The high fluorescence QY in wild-type GFP is explained by a restricted ϕ_P torsional motion in the *p*-hydroxybenzylidene-2,3-dimethylimidazolinone ($HBDI^-$) chromophore due to strong electrostatic interactions, which are diminished in the isolated chromophore,[212] leading to enhanced torsional motion and consequently a fluorescence quantum yield of practically zero.[213] Due to the variety of protein environments and chemical modification of its chromophore, GFPs may display a variety of functionalities, including photoisomerization.[214] As an example, Zhang *et al.* performed QM/MM based trajectories on a mutant-GFP which, after generation of the anionic fluorophore through ultrafast proton transfer, undergoes photoisomerization through a concerted hula-twist mechanism involving asynchronous P-bond rotation (ϕ_P, C_5–C_4–C_3–C_2 dihedral angle) and I-bond rotation (ϕ_I, C_4–C_3–C_2–C_6 dihedral angle) (Scheme 7).[215] Although these two modes are asynchronous, *i.e.* they do not start simultaneously, they maintain a certain phase relationship upon reaching the CoIn. Furthermore, the synchronized motion of the H15 HOOP mode with the ϕ_I mode was deemed important to lower the ES barrier to reach the CoIn.

A recent combined spectroscopic and computational study on the ES dynamics of isolated $HBDI^-$ investigated the relevance of the relative phase between the HOOP mode and the ϕ_I mode in controlling the QY of the isomerization of the $C_2{=}C_3$ bond (see Scheme 7) through the corresponding energetically uphill IS (Fig. 17).[96] The distribution of nonadiabatic events (spawns) along the HOOP and I-torsion coordinates shown in Fig. 17a has maxima centred around out-of-phase configurations (Fig. 17c), where the direction of pyramidalization of the methine carbon (C3 in Scheme 7) is opposite to the torsional direction relative to 90°. The localized orbitals in Fig. 17d demonstrate how the out-of-phase direction of the HOOP mode relative to the torsion maintains the electronic degeneracy, forming the MECI-I (type 3, Section 2.2). Depending on the sign of the I-torsion, either the MECI-I^+ (positive) or MECI-$I2^+$ (negative) is reached, which are connected on the IS through a certain linear combination of HOOP and I-torsion (see black lines in Fig. 17a). Because the latter CoIn is closer to the FC-point (Fig. 17b), the majority of nonadiabatic events occur in this region. However, whereas nonadiabatic decay through MECI-I^+ predominantly yields the *E* isomer (photoproduct) due to the negative HOOP phase, passage through MECI-$I2^+$ results in formation of predominantly the *Z* isomer (reactant) due to the positive HOOP phase. Therefore, a HOOP-phase control similar to the one described in the rhodopsin photoisomerization (Section 3.1) appears to operate in the $HBDI^-$ chromophore and potentially in GFP variants.

The $C_3{=}N_4$ double bond in Me-FlOH, a model compound of the fluorophore in bacterial luciferase (Scheme 7), is ring-locked, allowing only IC as a relaxation pathway that involves a highly twisted $S_1(\pi\pi^*)/S_0$ CoIn (type 3, Section 2.2) through large dihedral angle distortion of C_1–N_2–C_2–N_4. The barrierless pathway towards this CoIn involves a sequential BLA stretch and out-of-plane deformation of the pyrimidine ring, that is similar to the relaxation pathway in cytosine and other pyrimidine bases.[216–218] Despite the clear requirement of cooperative motion of two modes for nonradiative decay in these systems, it has yet to be investigated how the relative phase of these modes drives IC.

The photoinduced double bond isomerizations present in biological systems have inspired chemists to design biomimetic switches that can perform the same function, in particular the optomechanical energy transduction found in rhodopsin.[73,167] One major asset that these switches should demonstrate is VC throughout the complete reaction path, since a phase relationship between relevant modes should be conserved to achieve high QYs (Section 3.1). Since wavepacket decoherence is more significant on flat PESs, a prerequisite for conservation of VC is a steep gradient towards the CoIn. Chemical modification can be used to engineer VCs as

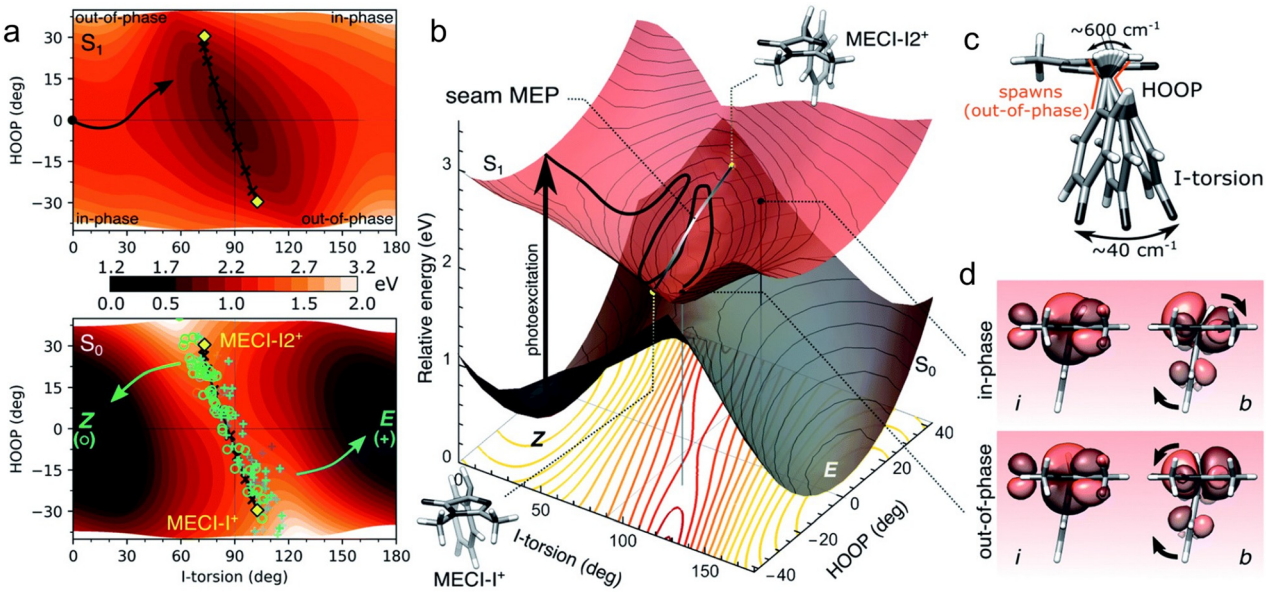

Fig. 17 Phase relation between HOOP and I-torsion in HBDI$^-$ chromophore in the vicinity of the I-torsional IS.[96] (a) S_1 and S_0 PES contour plots as a function of HOOP and I-torsion coordinates. The black arrow in the top panel indicates the minimum energy reaction path after photoexcitation to the FC-point. The yellow diamonds display the locations of two relevant MECIs (type 3, Section 2.2) along the I-torsion IS (black line connecting the two diamonds), MECI-I$^+$ and MECI-I2$^+$ (their geometrical structures are also shown in (c)), where the + sign indicates the enantiomeric direction (the other direction is not considered here). Nonadiabatic S_1 to S_0 transfer events (spawns) were computed with the AIMS method. The open green circles represent events resulting in the *Z* isomer, whereas the blue plus signs indicate events resulting in the *E* isomer. (b) Three-dimensional representation of the contour plots in (a). The black line again indicates the minimum energy reaction path from the FC-point to the I-torsional IS. The yellow points indicate the MECI structures that are connected by the grey line (the IS). The two black dots on the S_1 PES correspond to in-phase and out-of-phase configurations at the same I-torsional angle (see (d)). The red lines demonstrate the coordinates where the S_1 and S_0 PESs become degenerate, *i.e.*, form the IS. (c) Schematic representation of HOOP and I-torsion modes (ϕ_I in Scheme 7), indicated with their frequencies as estimated from the dynamics. (d) Localized orbitals on the I-ring (i) and methine bridge (b) for the in-phase and out-of-phase configurations indicated in (b). At this large I-torsional angle (~90°), these two orbitals are orthogonal, which results in an electronic degeneracy between S_1 and S_0. This degeneracy is lifted with I-torsional motion but is counteracted by the out-of-phase HOOP motion, which conserves the orthogonality between i and b. Reproduced with permission from ref. 96. Copyright 2022 Royal Society of Chemistry.

demonstrated in a *N*-alkylated indanylidene–pyrroline (NAIP) biomimetic switch (Scheme 7).[155] Whereas in *Z*-1 VC of a normal mode created on the S_1 PES was conserved in the photoproduct, the VC generated on the ES PES for the demethylated *E*-2 was not observed. The corresponding QM/MM energy profiles and nonadiabatic trajectories rationalized this by an initial twist present in *Z*-1 that shapes the S_1 and S_2 PESs such that they are separated in energy so that the FC-region on the S_1 PES displays a steep gradient towards the $S_1(\pi\pi^*)/S_0$ CoIn (type 3, Section 2.2).[155] This twist is not present in *E*-2, resulting in a flatter ES PES and therefore reduced VC, presumably due to enhanced S_2/S_1 character mixing similar to rPSB11 isomerization in methanol compared to the opsin environment (Fig. 10).[99]

Although only the torsional mode VC was spectroscopically detected for *Z*-1, the nonadiabatic trajectories showed a coordinated interplay of modes similar to rhodopsin.[173,219] An initial BLA stretching relaxation (10 fs) is followed by large out-of-plane pyrrolinium ring deformations and double bond torsion. It has been hypothesized that C3 (see Scheme 7), and less likely C2′ (due to the bulkier substituent), out-of-plane motions (COOP) mimic the HOOP motion in rhodopsin by restoring the p-orbital overlap through pyramidalization of C4 (and C1′).[220] However, since the COOP motion is lower frequency than HOOP, the phase of the COOP mode might not change significantly upon reaching the CoIn. A poorly phase-matched COOP motion with respect to the torsional motion around the $C_{1'}{=}C_4$ double bond could then be the reason that the QY in these compounds remain as low as 0.20. Alternatively, the phase matching rule may not be valid if the COOP velocity is too low, even though the relative phase is correct. On top of this, as the substituents at the reactive double bond are almost identical, the torsion and COOP modes are more strongly coupled than the torsion and HOOP in rPSB11, which could result in a slower torsional motion. The slower propagation along the reaction coordinate could lead to a broader population decaying on a longer time scale and, possibly, to a full range of phase relationships rather than a single favorable one.

The reasoning above suggests that turning on VCs by chemical substitution, along with optimization of the phase relationship between relevant normal modes, is a promising tool to control QYs.[221,222] For double bond isomerization, these relevant normal modes typically involve torsional modes that are coupled to a pyramidalization mode, as has been observed for molecular motors as well.[74,223] For instance, a recent quantum dynamics study on a chiral *N*-alkyl imine motor

showed how the interplay of carbon pyramidalization, nitrogen out-of-plane, and torsional modes may control the C=N photoisomerization QY and therefore the bias for unidirectional rotation.[224]

3.3 Other photochemical and photophysical processes

The current section aims to investigate the applicability of the phase matching rule for rhodopsin photoisomerization (Section 3.1) to any ultrafast vibrationally coherent ES process. The first reaction-induced VCs, *i.e.* generated by the ES PES far from the FC-region, have been measured by femtosecond laser pulse experiments on photodissociation reactions in the late 80s and 90s.[225–229] As these reactions frequently involve a single stretching coordinate, one can, in principle, apply the standard LZ model (Scheme 5). On the other hand, since photochemical pericyclic reactions often involve multiple PESs and CoIns, analysis of the vibrational dynamics in these reactions may be challenging.[9–11,105,230] Nevertheless, the concerted nature of these ultrafast reactions has been demonstrated and VCs have been detected for relevant reaction coordinates, such as in the electrocyclic ring-opening of 1,3-cyclohexadiene to *Z*-hexatriene (more specifically to its *cis-Z-cis* conformer).[23,231,232] However, the direct assignment of the detected VCs to the *Z*-hexatriene product motion remains speculative for this particular reaction, which occurs within 68 fs upon $S_1(\pi\pi^*)$ excitation, as was recently observed with TRPES.[23] The retro-Diels–Alder reactions of several cationic cyclic alkenes exhibited VCs, which could be identified as product VCs by mass-resolved detection, indicating a concerted mechanism.[233]

Haiser *et al.* performed a joint time-resolved spectroscopic-quantum chemical study on the photochemically allowed disrotatory 4π-electrocyclization in lesion dinucleotides (simplified structures are shown in Fig. 18a) to understand UV-induced processes in DNA, clearly demonstrating the cooperative motion of multiple modes (red path in Fig. 18b).[234] This reaction presumably proceeds through a type 1 CoIn involving an in-phase and out-of-plane (disrotatory) motion of N3 and C6 (the carbon atom making the new σ bond) after formation of an ES minimum in the $(\pi\pi^*)$ state. Despite the activation barrier on this path, which is associated with a long ES lifetime (130 ps), the reaction QY is not negligible (0.082).[235] Note that in this case the inverse correlation between ES lifetime and reaction QY predicted by the standard LZ model does not apply as it assumes a barrierless reaction path (Fig. 5b). Cleaving the phosphodiester backbone results in the formation of an energetically more accessible CoIn that forms an efficient funnel back to the reactant (green path in Fig. 18b) through out-of-plane motion of N3 accompanied by C4 pyramidalization,[236] similar to the aborted double bond isomerization for the CoIn (type 3) found in 5-methylpyrimidinone (5M2P, see structure in Fig. 18a).[217,237] The latter motion cannot occur in the intact backbone lesion structure, due to the ring strain from the rigid macrocycle, forcing the ES wavepacket to change its direction to $CoIn_{Dewar}$ (red path). Although this mechanism implies competition between population of similar molecular modes, it represents a case distinct from the one discussed above for rhodopsin where the HOOP and isomerization mode of rPSB11 contribute to propagation towards a single reactive IS segment. Instead, this case is more reminiscent of a situation like the one depicted in Fig. 5e where the intact backbone modifies the topography of the ES PES to favour one type of CoIn (type 1) rather than the other (type 3).

Singlet fission is a photophysical process that converts a singlet ES (S_1) molecule into two triplet ES (T_1) moieties *via* a correlated triplet pair intermediate (^{1}TT) (Fig. 19a), which has the potential to increase the theoretical power conversion efficiency in organic photovoltaics (OPVs).[238] Multiple studies on thin film singlet fission materials have shown that not only both intramolecular and intermolecular nuclear motions are relevant for driving the singlet fission, but also that the ultrafast S_1 to ^{1}TT conversion is vibrationally coherent,[239–242] which might be switched off by solvent effects.[243] For a complete overview of the vibronic coupling mechanisms in ultrafast coherent ^{1}TT formation, the reader is referred to the recent review by Kim and Musser.[244] As an illustration, we focus here on one study where the nature and coordinated interplay of the critical normal modes in a pentacene dimer have been elucidated using a combination of IVS and fully quantum mechanical tree-tensor network state simulations (TTNS).[245] By tracking the impulsively generated VCs after photoexciting the $S_1(\pi\pi^*)$ state, Schnedermann *et al.* concluded that the wavepacket survives the nonadiabatic transition, hypothetically through a CoIn.[103] Combining the spectroscopic data with the TTNS method,[246] a detailed molecular movie of the first 200 fs of this singlet fission trajectory could be produced, showing a periodicity in the tuning-coupling mode (practically the $\mathbf{Q}_1$ and $\mathbf{Q}_2$ vectors of the BP, respectively) subspace that indicates the conservation of a phase relationship between these modes (Fig. 19c). The initial 75 fs are dominated by the tuning mode (vertical orange displacement) that relaxes the wavepacket out of the FC-region by in-plane ring deformations, stretching the central pentacene–pentacene bond length effectively. In the next 125 fs, the activity is shifted towards the coupling mode (horizontal green displacement) that twists this central bond, enforcing a deviation from orthogonality between the pentacene moieties which causes transient overlap between their orbitals, eventually forcing the nonadiabatic S_1 to ^{1}TT transition.[247] Even though the reaction appears as a subsequently coordinated process in which the photon energy is initially funneled into the tuning mode (A_1) after which *via* energy transfer the B_1 mode becomes active, similar to the BLA and HOOP-torsion sequence in rhodopsin (Section 3.1), at every stage there is a cooperative motion of these modes that implies an intramolecular vibrationally coherent process. However, from these simulations it is not evident yet how the relative phase of the tuning and coupling modes controls the near ideal efficiency of 192% for the singlet fission process, which has been quantified by the triplet QY in toluene.[248] The phase relationship described in this case appears to focus on the change in the reaction coordinate along the ES PES of the system. Nevertheless, it is likely that the understanding of the QY also requires the comprehension of the decay at an IS

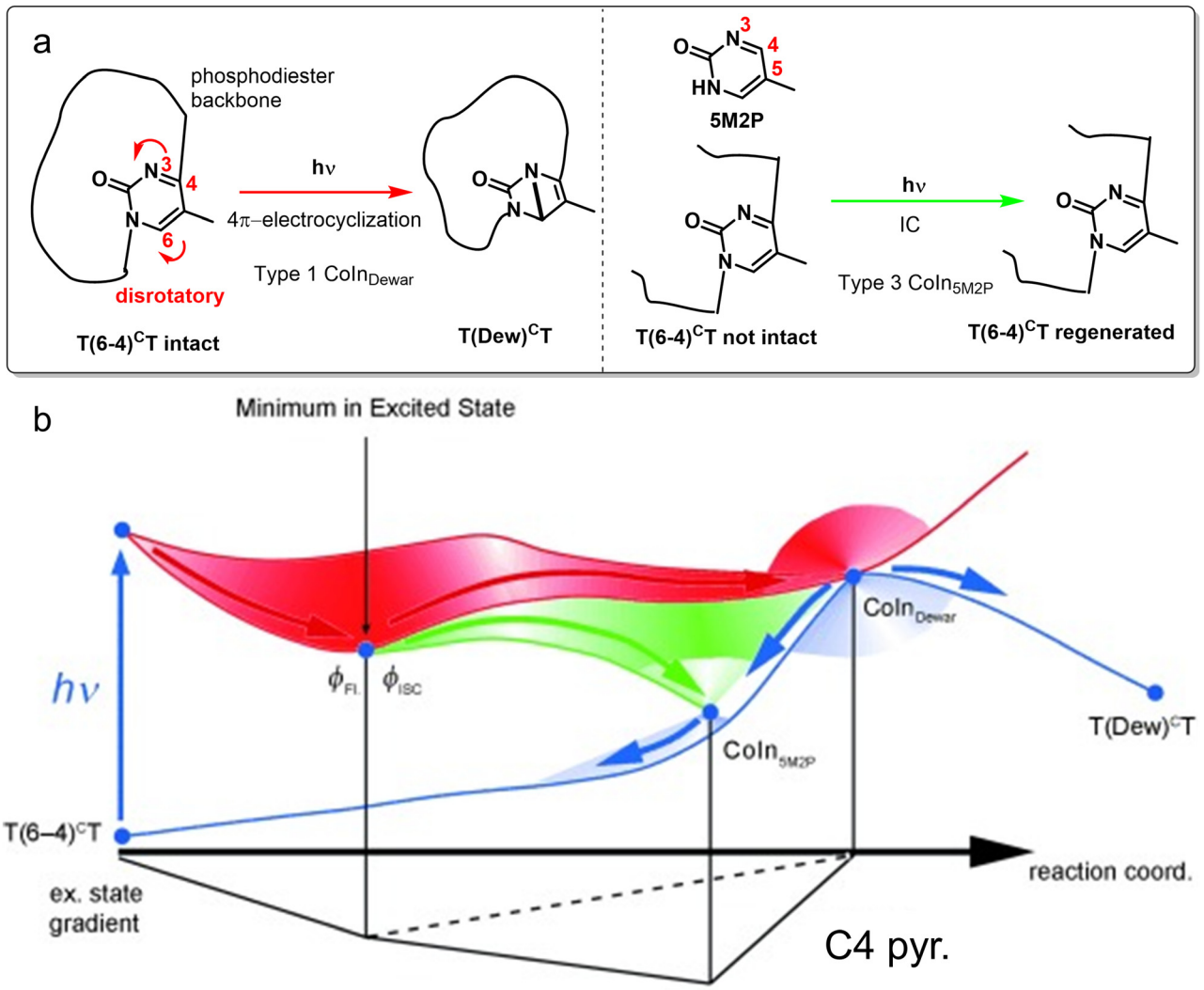

Fig. 18 (a) Reaction schemes for photochemical dynamics of dinucleotides *T*(6-4)^{C}T with an intact and cleaved DNA backbone. Note that only the photochemically active core of T(6-4)^{C}T is shown, indicating the remaining part of the DNA backbone with a black line. Photoexcitation of T(6-4)^{C}T with an intact DNA backbone results in formation of the Dewar valence isomer, whereas T(6-4)^{C}T with a cleaved DNA backbone results in IC, having a similar CoIn mediated decay mechanism as 5-methyl-pyrimidone (5M2P). (b) Photochemical and photophysical pathways on the ES PES illustrated for these structures. After photoexcitation to the ππ* state, an initial relaxation on the S_1 PES leads to an ES minimum for both the intact and cleaved (without the phosphodiester group) backbone structures. From there, the cleaved structure follows the green pathway to reach CoIn$_{5M2P}$, which is an efficient funnel for IC. In contrast, for the intact structure this CoIn is not accessible and hence follows the red pathway to a type 1 CoIn$_{Dewar}$ that leads to either formation of the Dewar valence isomer or the reactant (IC).[234] Adapted with permission from ref. 234. Copyright 2011 John Wiley and Sons.

segment and, therefore, the participation of one or more extra vibrational modes in the decay process.

Several recent studies focus on the interpretation of the VC spectral evidence in terms of wavepacket evolution along different vibrational modes. The importance of VCs and their link with CoIns has been recognized in OPVs, where energy transfer and electron transfer should be controlled.[249–252] For instance, it has been suggested that VC enhances the efficiency of energy transfer in a photosynthetic dimer model system[253] and charge separation at a donor-acceptor interface.[254] Moreover, the intimate coupling between vibrational modes and energy transfer in photosynthetic functions is gaining more attention over the years, driven both by (two-dimensional electronic) spectroscopic achievements[255–258] as well as mixed quantum-classical simulations, which clearly show a cooperative effect of multiple modes.[259,260] Despite this, often a single mode is assumed to be relevant in the description of vibronic coupling.[261–263] However, as has been illustrated multiple times now in this review, there may be coupling of electronic states to multiple vibrational modes, strongly affecting the dynamics and involvement of CoIns.[264] Tracking reaction-induced VCs in photoexcited donor–acceptor–donor (D–A–D) dyes has been used to distinguish between the formation of excimer and charge transfer (CT) states,[265] and to elucidate the (bimodal) reaction path of ultrafast intermolecular electron transfer in an electron-donating solvent[266] and at dye-semiconductor

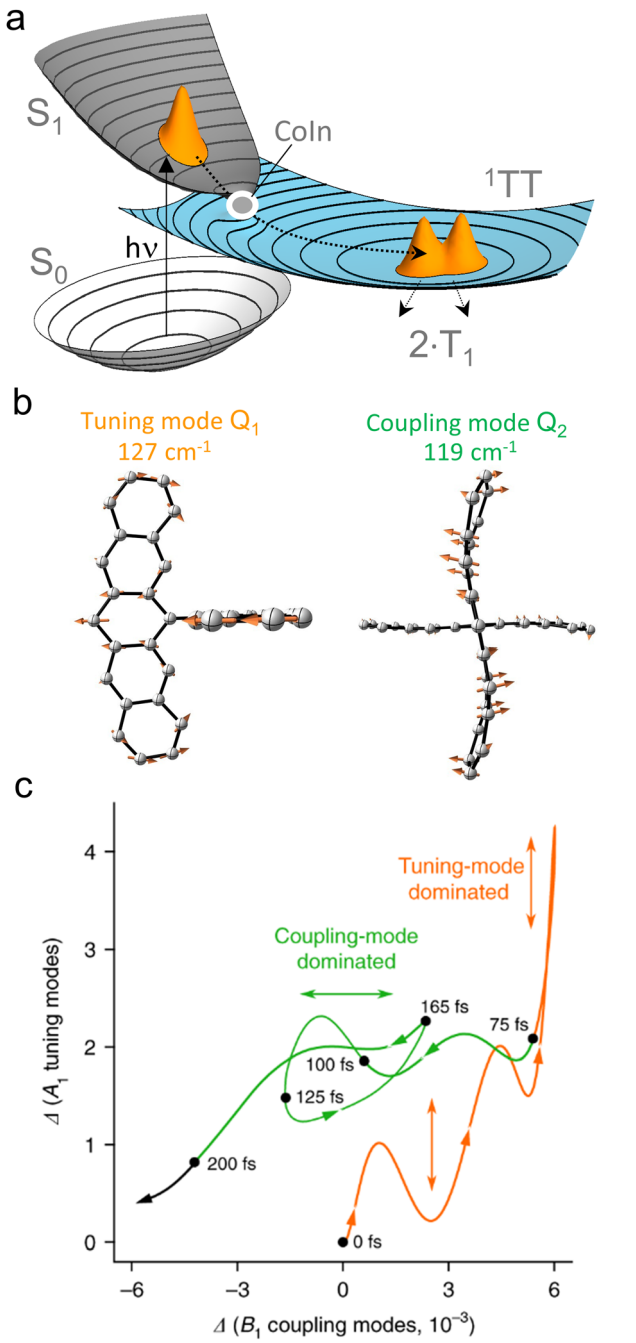

Fig. 19 Multi-mode mechanism for ultrafast singlet fission. (a) PES visualization for a general singlet fission reaction. After photoexcitation to the S_1 state, the correlated triplet-pair ^{1}TT is populated on an ultrafast timescale through a CoIn, which on a slower timescale decoheres into two triplet states T_1.[241] Adapted with permission from ref. 241. Copyright 2015 Springer Nature. (b) Vector visualization of the relevant tuning (A_1) and coupling (B_1) modes for the S_1 to ^{1}TT conversion in the pentacene dimer DP-Mes, shown as truncated molecular structures for clarity purposes. (c) Correlation plot for the amplitudes of the A_1 and B_1 modes during the first 200 fs of the singlet fission trajectory. Indicated in orange is the tuning-mode dominated regime and indicated in green is the coupling-mode dominated regime. The arrows indicate the direction of the trajectory. The quantum dynamics calculations made use of a tree-tensor network state simulation (TTNS).[245] Adapted from ref. 245, licensed under a Creative Commons Attribution 4.0 International License.

interfaces.[267,268] Increasing the electron-donating character by chemical substitution resulted in faster electron transfer reactions in naphthalenediimide (NDI) dyes (Fig. 20a), which was rationalized by the conservation of VC throughout the reaction.[269] Crucially, the dye with the fastest electron transfer (shown in Fig. 20a) displayed two relevant VCs in the product involving NDI ring distortion and stretching coordinates, modulating the coupling between D and A. However, the detailed structure of the CoIn and mechanism of cooperation between these two modes, possibly involving an IS segment, could not be determined with just these one-dimensional spectroscopic techniques. Experimental methods that may elucidate the role of multi-mode vibronic couplings in ultrafast ES processes are two-dimensional techniques, such as 2D electronic,[161,270] 2D vibrational[271,272] and 2D vibrational–electronic spectroscopy.[273–275] However, even these techniques reach their full potential when combined with nonadiabatic molecular dynamics simulations to elucidate the IS structure,[276] as was demonstrated by the recent 2DES study from De Sio *et al.*, who discovered the first intermolecular CoIn and the relevant coupling and tuning modes in an organic A–D–A oligomer.[277] The reader is referred to the excellent review by Scholes and co-workers for an overview of 2DES techniques as well as their application to a number of case studies.[278]

Despite this finding, CoIns in OPVs and other optoelectronic materials have generally been regarded as funnels for IC, leading to charge losses. Theoretical investigations on the structure of CoIns and the relevant vibrational dynamics are again key to avoid these unfavorable decay channels, as tentatively demonstrated for fluorescent molecular crystals,[39] D–A dyes[36] and (nano)materials, in which defect-induced CoIns (DICIs) are associated with fast nonradiative decay.[37,280–284] The relatively low IC rates in lead-halide perovskites,[285] which are organic–inorganic hybrid materials considered for next-generation PV applications, have been computationally explained by the energetic inaccessibility of CoIns in molecular and nanomaterial sized models.[286]

Molecular inorganic systems often find applications in photocatalysis, in which photoinduced electron transfer might be in competition with IC. Retarding specific vibrational modes by rigidifying the chemical structure to facilitate photoredox chemistry is a strategy that was recently applied by McCusker and co-workers with the aim of extending the MLCT lifetime in a Fe(II) complex.[287] IVS was used to identify the modes involved in IC, as these appeared as vibronic coherences. The term vibronic is used here instead of vibrational to emphasize that the coherence is maintained across two electronic states. These vibronically coherent modes were synthetically modified to decouple them from the IC reaction coordinate (Fig. 20b),[279] resulting in a 20-fold lifetime increase. Targeting vibronic coherences has great potential to understand and control other ultrafast ES processes, such as ISC,[288,289] proton-coupled electron transfer[290] and singlet fission.[291]

Although ISC is often regarded as a much slower process than IC due to the spin-forbidden character of this nonadiabatic transition, in some cases it may be ultrafast even in

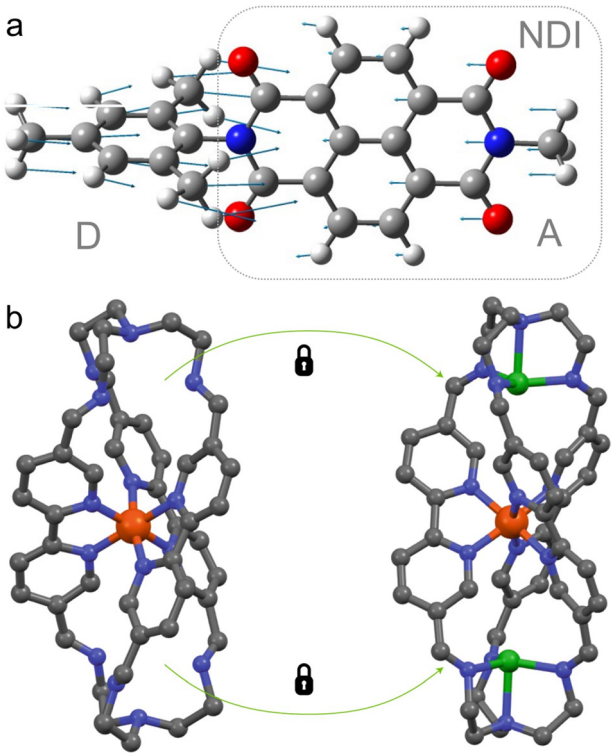

Fig. 20 (a) Vectorial representation of a vibrational mode from a D–A dye involving C–N stretching and NDI ring distortion, which was observed as a VC in the product of an ultrafast electron transfer reaction. Not shown is the antisymmetric analogue of these two reaction coordinates which was detected as a product VC in this D–A dye as well.[269] Adapted with permission from the ESI of ref. 269. Copyright 2021 American Chemical Society (b) Fe(II) complex with polypyridyl ligand (left structure) shows large-amplitude motion which facilitates fast nonradiative decay when excited to the MLCT state. Blocking these modes through addition of copper (right structure) results in a significantly longer MLCT lifetime.[279] Grey: carbon. Blue: nitrogen. Orange: iron. Green: copper. White: hydrogen. Red: oxygen. Reproduced with permission from ref. 279. Copyright 2020 Springer Nature.

the absence of heavy-atom induced strong spin–orbit coupling.[292–294] In a nonrelativistic description ultrafast ISC involves a singlet–triplet crossing, which is topologically not a CoIn (in a fully relativistic description this can be seen as a CoIn)[295] but rather a linear—*i.e.* not conical—crossing part of a $3N-7$ IS as the off-diagonal elements are zero for different spin multiplicities (eqn (2), Section 1). Nevertheless, the coupling of multiple vibrational modes could be relevant to the ISC dynamics in transition–metal complexes leading to mechanistic pictures similar to the ones discussed above. Spectroscopically observed vibrational and vibronic coherences are again relevant markers to track and control ISC and IC pathways.[288,296] Khalil and co-workers studied the photochemical dynamics of a Ru(II) complex with 3D EV spectroscopy, which is a technique capable of following vibronic couplings involving multiple normal modes.[297] Clear evidence of the cooperation between two normal modes to reach the ^{3}MLCT state through a singlet–triplet crossing was provided in this study.

Recent ground-breaking work of Ihee and co-workers demonstrated how femtosecond time-resolved X-ray liquidography (TRXL) could reveal real-time wavepacket trajectories in the photoinduced asynchronous bond formation of a trimer gold complex, $[Au(CN)_2^-]_3$, from its monomers in an aqueous solution.[298] The multidimensional wavepacket trajectory in Fig. 21 shows how after excitation to the FC-region in the S_1 state, its evolution on the T_1' PES in the first 60 fs is dominated by formation of one covalent bond (R_{AB}) and within 360 fs the next one (R_{BC}), which along with increasing bond angle (θ) eventually yields the T_1' equilibrated linear trimer complex. From the R_{AB}–R_{BC} subspace it is clear how the temporal changes in both coordinates are correlated, implying a vibrationally coherent ultrafast photochemical reaction. The atomistic motions associated of R_{AB} and R_{BC} could also be fitted to the sum of two symmetric stretching modes.[299]

4. Conclusion and outlook

Above we have seen how, in general, the control of "elementary" ultrafast photochemical processes requires information on the precise dynamics leading to the IS. This is provided by state-of-the-art time-resolved spectroscopic and computational studies that, in recent years, have produced results leading to a significantly refined and extended mechanistic spectrum of these processes. This conclusion is schematically illustrated in Fig. 22 that displays the limiting mechanisms affecting the product/reactant branching ratio of a barrierless photochemical reaction of the type shown in Fig. 5b and 6. In Fig. 22a we display what is, essentially, a one-mode mechanism implying decay at a single critical CoIn usually assumed to correspond to the MECI. In such a situation, the population propagates along a single ES path ultimately entering the BP along a specific direction, which is described by a combination of $\mathbf{Q}_1$ and $\mathbf{Q}_2$. If this direction is known one can apply the standard LZ model that predicts that an increase in nuclear velocity at the point of decay (this may as well arise from a steeper slope of the ES PES) leads to an enhanced QY. As discussed above, this simple conclusion has opened the route to the rationalization of many trends observed by chemical substitution in this review.[61]

Despite its successes, the one-dimensionality of the reaction coordinate that the above model assumes fails when the photochemical reaction mechanism is of multi-mode character, and it becomes important to consider decay at multiple CoIn points along the IS. Such a mechanism is shown in Fig. 22b and is consistent with the studies of the photoisomerization of the rPSB11 chromophore in rhodopsin where the "reaction coordinate" is described by a number of parallel trajectories each displaying distinct dynamic changes in the weights of the HOOP and torsional modes.[134,153] The final QY is, therefore, given by the sum of different QY contributions determined by the evolution of the phase relationship of each trajectory and, in turn, the velocities at decay that may also have opposite orientation for different subpopulations. It is apparent that the multi-mode mechanism can lead to the failure of

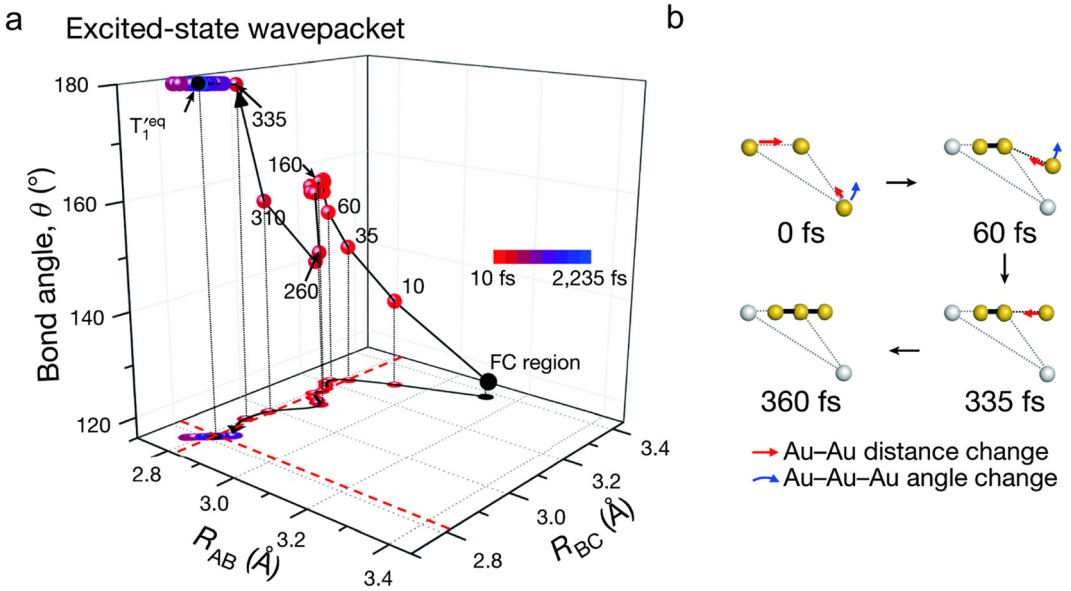

Fig. 21 Photoinduced asynchronous bond formation of the gold trimer complex $[Au(CN)_2^-]_3$. Excitation with a pump pulse generates an ES wavepacket in the S_1 state, which undergoes ISC to populate T_1' in 20 fs. (a) Evolution of ES wavepacket in T_1' as a function of multiple nuclear coordinates, R_{AB}, R_{BC} and θ, which show significant changes in the early timescale (<360 fs). Some representative points during this period are indicated with red dots. The trajectory in the $R_{AB} - R_{BC}$ subspace is shown at the bottom. At later time (>360 fs), oscillations around the equilibrium structure of T_1' occur, of which the equilibrium coordinates R_{AB} and R_{BC} are indicated with red dashed lines. (b) Geometrical transient structures at representative points in time, showing with red and blue arrows the changes in bond lengths and angle respectively. Whereas the yellow dots represent the geometrical evolution of Au atoms, the grey dots represent the Au atoms in the FC-region. Covalent bond formation is visualized with the thick black lines. The CN ligands are omitted for clarity.[298] Reproduced with permission from ref. 298. Copyright 2020 Springer Nature.

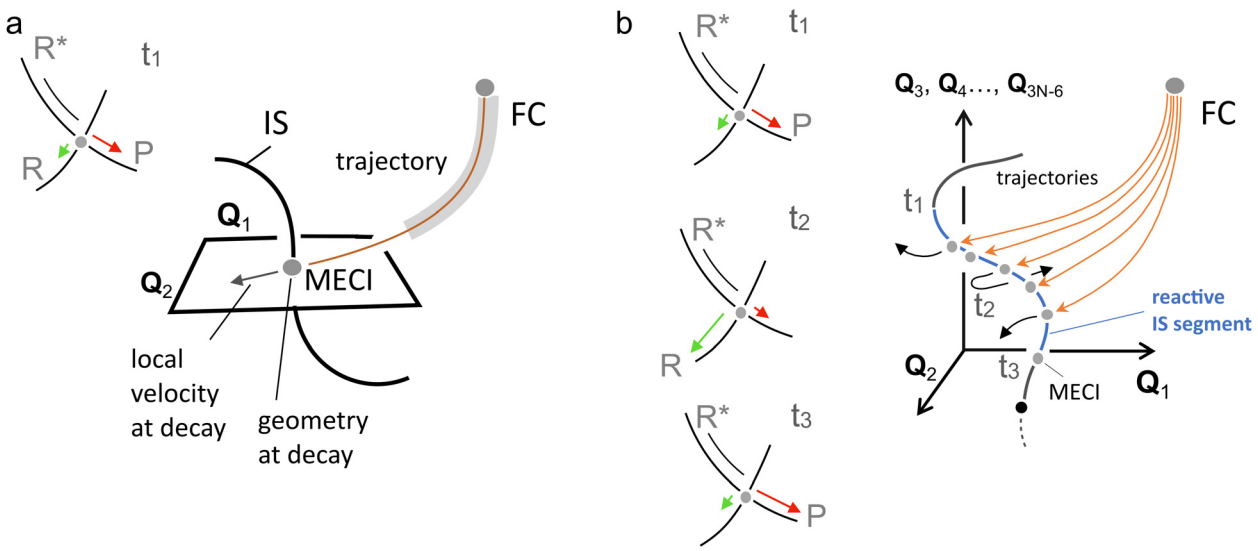

Fig. 22 Limiting mechanisms for an "elementary" ultrafast photochemical reaction. (a) One-mode mechanistic picture. The MECI is accessed along a single specific mode (reaction coordinate) describing the trajectory along the BP of a compact (vibrationally coherent) population. The QY is proportional to the corresponding velocity at the decay point (see inset on the top-left). Such mode does not necessarily correspond to the mode driving the system out of the FC region. In fact (see trajectory region highlighted in grey), the ES trajectory may be described by a "curved" coordinate featuring sequential progression along different modes. (b) Multi-mode mechanism. In this case the populations are less compact or partially fragmented thus generating a set of subpopulations reaching the IS at different times (*e.g.* t_1, t_2 and t_3) and along different BP modes (see also Fig. 3b). Along each trajectory the phase relationship between different modes belonging to BP and/or IS (*e.g.* $\mathbf{Q}_1$ and $\mathbf{Q}_3$) changes resulting in different velocity patterns at decay. The QY now becomes a much more complex quantity featuring the contributions of each subpopulation (see insets on the left).

the standard LZ model. For instance, such event would explain an "anti-LZ" correlation, *i.e.* slower nuclear velocity leading to enhanced isomerization QY.[205] In addition, and irrespective of the operating mechanism, the observation of VCs in complex

molecular systems throughout the complete photoisomerization path strongly hints towards a higher-dimensional reaction coordinate that incorporates multiple normal modes and their coordinated interplay.[73] This results in vibrationally "curved" reaction coordinates.

Strong computational evidence supported by isotopic substitution experiments has been provided for the photoisomerization of rPSB11 and rPSBAT that demonstrates a multi-mode model, demonstrating the relevance of the relative phase of normal modes in controlling the photochemical QY.[113,194] Specifically, it is the branching at different IS points that is controlled by the relative phase of the HOOP mode with respect to the torsional mode. This phase matching is dependent on the ES PES, as this provides the forces on the reactive normal modes and therefore the dynamical progression towards the CoIn. However, again in contrast with the standard LZ model, it is not only the velocity along one relevant normal mode (*e.g.*, the torsional mode) that controls the branching ratio at decay and therefore the QY, but the coordinated motion of multiple modes up until the BP of each CoIn point along the IS segment that is entered (more correctly the point where the wavefunction switches from antibonding to bonding). A prerequisite for this phase-controlled regime is that the nuclear velocities are above a certain threshold, as reactive modes with near zero velocities would not have a favored direction towards either the product or reactant, possibly making the phase rule less effective.

Although it is fascinating that rhodopsin photoisomerization displays multi-mode VC throughout the complete reaction, there is no reason to suspect that it is unique in this regard. Indeed, it is likely that such a mechanism applies to other vibrationally coherent ultrafast ES processes as well, including pericyclic reactions, electron transfer and energy transfer. Although in many of these processes it has been highlighted how the coordinated motion of multiple normal modes drives ES dynamics and in some cases VCs of those modes have even been spectroscopically observed throughout the reaction,[215,225,234,245,300] detailed investigations of the decay process at a level similar to what has been done for rhodopsin photoisomerization are required to confirm a multi-mode mechanism for these systems. We anticipate that an increased understanding of the role that the coordinated motion of normal modes play near the CoIn will greatly benefit from advances in both the simulation and spectroscopy fields.[152] Computational photochemists in particular will benefit from rapid progress in sampling techniques and machine learning algorithms for the accurate prediction of ES properties and automated discovery of ultrafast photochemical reactions and mechanisms.[58,141,142]

Owing to major advances in the generation of stable and short laser pulses, ultrafast spectroscopic techniques are capable of studying temporally resolved ES processes with unprecedented high accuracy,[301] including ultrafast fluorescence upconversion techniques specifically applied to photochemical reactions in confined media.[302] In particular, time-domain Raman spectroscopy has benefited from the availability of <10 fs pulses, allowing the observation of fundamental modes up to ~ 3000 cm^{-1}.[168] However, the observation of VCs associated with coupling the two ES PESs involved in the nonadiabatic transition remains a challenge, due to the near-zero Huang–Rhys factor.[244] Technological progress in higher dimensional ultrafast techniques enables the observation of vibrational and vibronic couplings in the ES, which is critical to develop a multi-mode understanding of photochemical reactions next to the mere detection of the relevant modes.[297,303–308] However, the assignment of normal modes is often solely based on a numerical comparison between the frequencies obtained from Fourier-transformation with computationally acquired frequencies. More detailed mechanistic insights of ES dynamics may be obtained through analysis of time-dependent amplitude and phase, providing a more direct comparison to nonadiabatic calculations as well. In particular, addition of an extra "actinic" pulse in IVS experiments allows the time-resolved tracking of ES modes.[169,309,310] Although it has already been demonstrated how tracking the time-dependent amplitude provides crucial insights in the ES proton transfer in the photoactive yellow protein[311] and GFP,[304] we believe that tracking the relative phase of ES modes could elucidate the multi-mode character of photochemical reaction paths and its impact on the QY.

Tracking the time-dependent phase and amplitude of the ES nuclear dynamics might be achieved with alternative spectroscopic techniques that achieve atomistic detail, such as femtosecond electron diffraction.[312,313] Alternatively, the recent development of X-ray free electron laser beam sources has enabled techniques which are, in principle, capable of probing photochemical dynamics with such high structural sensitivity and temporal resolution,[314] as has been demonstrated experimentally through direct observation of CoIn dynamics with transient X-ray absorption spectroscopy.[315–319] To extract information about the underlying nonadiabatic dynamics from their spectral signatures it is key to construct theoretical frameworks,[320] with important contributions for transient X-ray absorption spectroscopy,[321] but also X-ray based techniques that have only been demonstrated theoretically, such as time-resolved X-ray diffraction,[322,323] time-resolved X-ray spontaneous emission spectroscopy[324] and TRUECARS. The latter was developed by Mukamel and colleagues to analyse vibronic coherences that are generated by stimulated ultrafast X-ray Raman pulses.[325] The TRUECARS probing setup is designed to measure these generally weaker vibronic coherence signals, which are otherwise hidden underneath the much stronger electronic population contributions, allowing the detection of multiple CoIn passages as well as the assignment of the relevant vibronic normal modes of a photoexcited bichromophoric molecule.[326] Finally, amplifying vibronic coherences with a correctly timed resonant IR pulse holds further promise to detect these otherwise weak signals in X-ray diffractive imaging.[327] The use of IR pulses could also elucidate vibrational energy transfer mechanisms as recently demonstrated in a GS isomerization reaction.[328]

We propose that the three pillars that have elucidated the mechanism of ultrafast rhodopsin photoisomerization,

should function as a template to discover and rationalize similar multi-mode mechanisms in other systems. Although VCs that are preserved after passage through a CoIn could potentially demonstrate the significance of phase matching at different IS points (I), nonadiabatic dynamics calculations are required for a detailed understanding of how this coherence connects to the QY (II). The vibrational phase isotope effect is then the perfect experimental confirmation for such a mechanism, as isotopic substitution only changes the vibrational dynamics, but not the spectroscopic properties or the shape of the ES PES (III). Alternatively, application of an electric field or external forces (Section 3.1.4) will prove fruitful in future research, as subtle tuning of the phases of specific normal modes may be achieved.[198,329,330] It is also expected that synergy between coherent control laser experiments and the tuning of the relative phases in controlling photochemistry will increase, as shaped laser pulses are potentially capable of selectively preparing wavepackets on the ES PES with certain mode phase relationships. Although the optimization of the isomerization QY in rhodopsin[162,331] and molecular switches,[332] or the selective hydrogen abstraction in acetylenes, allenes and toluene[333–335] has already been achieved with coherent control, these approaches rely on learning algorithms rather than chemically intuitive tuning or rational design.

Any rational design approach to control the ultrafast ES dynamics and reactivity should start by characterizing the normal modes which drive the nonadiabatic decay through their coherent motion and disentangling them from irrelevant VCs,[336,337] which may be derived from mode-specific dephasing times.[338] Although the methods described above could achieve this, synthetic modification has proven to be a successful method as well to assess whether a vibronic relevant mode has been targeted through measurement of the reaction rate or QY.[205,287] Optimization of the phase matching may, in principle, then be accomplished through a similar chemical modification, shaping the ES PES in such a way that the targeted normal mode either differs in relative phase or frequency. This chemical modification may be an electronically or sterically distinct substituent, a protein environment or solvent.[152,339] Finally, with the advent of attosecond laser pulses an initial ES population can be prepared in a mixed electronic state, which may result in ''unnatural'' populations of coupled vibrational modes, thus having the potential of further improving our understanding of multi-mode photochemistry.[340] We predict that such a rational design approach, at the molecular or supramolecular levels, will impact a wide variety of research fields that rely on light induced processes, including molecular motors, artificial sunscreens and solar energy conversion, where photochemistry, photostability and a long-lived ES are the goals respectively.

Conflicts of interest

There are no conflicts to declare.

Acknowledgements

We thank Dr Christoph Schnedermann and Prof. Fred Brouwer for useful discussions. We also wish to thank Prof. Michael A. Robb for his useful comments on the first version of the manuscript. M. O. acknowledges support from NSF CSDM-A Grant No. 2102619 and European-Union, Next Generation EU, MIUR Italia Domani *Progetto mRNA Spoke 6 del ''National Center for Gene Therapy and Drugs based on RNA Technology''. – CUP B63C22000610006*.

References

1 D. R. Yarkony, *J. Phys. Chem. A*, 2001, **105**, 6277–6293.
2 K. R. Naqvi and W. B. Brown, *Int. J. Quantum Chem.*, 1972, **6**, 271–279.
3 E. Teller, *J. Phys. Chem.*, 1937, **41**, 109–116.
4 G. Herzberg and H. C. Longuet-Higgins, *Discuss. Faraday Soc.*, 1963, **35**, 77–82.
5 X. Zhu and D. R. Yarkony, *Mol. Phys.*, 2016, **114**, 1983–2013.
6 F. Bernardi, S. De, M. Olivucci and M. A. Robb, *J. Am. Chem. Soc.*, 1990, **112**, 592–634.
7 M. A. Bernardi, F. De Sushovan, S. Olivucci and M. Robb, *J. Am. Chem. Soc.*, 1990, **112**, 1737.
8 I. N. Ragazos, M. A. Robb, F. Bernardi and M. Olivucci, *Chem. Phys. Lett.*, 1992, **197**, 217–223.
9 F. Bernardi, M. Olivucci, M. A. Robb and G. Tonachini, *J. Am. Chem. Soc.*, 1992, **114**, 5805–5812.
10 M. Olivucci, I. N. Ragazos, F. Bernardi and M. A. Robb, *J. Am. Chem. Soc.*, 1993, **115**, 3710–3721.
11 I. J. Palmer, I. N. Ragazos, M. A. Robb, F. Bernardi and M. Olivucci, *J. Am. Chem. Soc.*, 1993, **115**, 673–682.
12 P. Celani, M. Garavelli, S. Ottani, F. Bernardi, M. A. Robb and M. Olivucci, *J. Am. Chem. Soc.*, 1995, **117**, 11584–11585.
13 I. J. Palmer, I. N. Ragazos, F. Bemardi, M. Olivucci and M. A. Robb, *J. Am. Chem. Soc.*, 1994, **116**, 2121–2132.
14 M. J. Bearpark, F. Bernardi, S. Clifford, M. Olivucci, M. A. Robb, B. R. Smith and T. Vreven, *J. Am. Chem. Soc.*, 1996, **118**, 169–175.
15 P. J. Reid, S. J. Doig, S. D. Wickham and R. A. Mathies, *J. Am. Chem. Soc.*, 1993, **115**, 4754–4763.
16 D. R. Cyr and C. C. Hayden, *J. Chem. Phys.*, 1996, **104**, 771–774.
17 M. O. Trulson and R. A. Mat, *J. Phys. Chem.*, 1990, **94**, 5741–5747.
18 K. O. Hiller, K. D. Asmus, F. P. Lossing, Y. T. Lam, A. Maccoll and C. E. Klots, *J. Am. Chem. Soc.*, 1993, **115**, 682–686.
19 F. Bernardi, M. Olivucci and M. A. Robb, *Chem. Soc. Rev.*, 1996, **25**, 321–328.
20 M. S. Schuurman and A. Stolow, *Annu. Rev. Phys. Chem.*, 2018, **69**, 427–447.
21 P. Avouris, W. M. Gelbart and M. A. El-Sayed, *Chem. Rev.*, 1977, **77**, 793–833.
22 A. P. Penner, W. Siebrand and M. Z. Zgierski, *J. Chem. Phys.*, 1978, **69**, 5496–5508.

23 S. Karashima, A. Humeniuk, R. Uenishi, T. Horio, M. Kanno, T. Ohta, J. Nishitani, R. Mitrić and T. Suzuki, *J. Am. Chem. Soc.*, 2021, **143**, 8034–8045.
24 J. M. Toldo, M. T. do Casal and M. Barbatti, *J. Phys. Chem. A*, 2021, **125**, 5499–5508.
25 Y. Shao, J. M. De Ruiter, H. J. M. De Groot and F. Buda, *J. Phys. Chem. C*, 2019, **123**, 21403–21414.
26 R. R. Birge, *Biochim. Biophys. Acta, Bioenerg.*, 1990, **1016**, 293–327.
27 M. Wanko, M. Hoffmann, T. Frauenheim and M. Elstner, *J. Comput.-Aided Mol. Des.*, 2006, **20**, 511–518.
28 D. Polli, P. Altoè, O. Weingart, K. M. Spillane, C. Manzoni, D. Brida, G. Tomasello, G. Orlandi, P. Kukura, R. A. Mathies, M. Garavelli and G. Cerullo, *Nature*, 2010, **467**, 440–443.
29 B. G. Levine and T. J. Martínez, *Annu. Rev. Phys. Chem.*, 2007, **58**, 613–634.
30 S. Takeuchi, S. Ruhman, T. Tsuneda, M. Chiba, T. Taketsugu and T. Tahara, *Science*, 2008, **322**, 1073–1077.
31 C. E. Crespo-Hernández, B. Cohen, M. Hare and B. Kohler, *Chem. Rev.*, 2004, **104**, 1977–2019.
32 W. J. Schreier, T. E. Schrader, F. O. Koller, P. Gilch, C. E. Crespo-Hernández, V. N. Swaminathan, T. Carell, W. Zinth and B. Kohler, *Science*, 2007, **315**, 625–629.
33 J. Fan, L. Finazzi and W. J. Buma, *Phys. Chem. Chem. Phys.*, 2022, **24**, 3984–3993.
34 T. T. Abiola, B. Rioux, J. M. Toldo, J. Alarcan, J. M. Woolley, M. A. P. Turner, D. J. L. Coxon, M. Telles Do Casal, C. Peyrot, M. M. Mention, W. J. Buma, M. N. R. Ashfold, A. Braeuning, M. Barbatti, V. G. Stavros and F. Allais, *Chem. Sci.*, 2021, **12**, 15239–15252.
35 D. P. Hoffman, S. R. Ellis and R. A. Mathies, *J. Phys. Chem. A*, 2014, **118**, 4955–4965.
36 A. M. El-Zohry, D. Roca-Sanjua and B. Zietz, *J. Phys. Chem. C*, 2015, **119**, 2249–2259.
37 B. G. Levine, W. T. Peng and M. P. Esch, *Phys. Chem. Chem. Phys.*, 2019, **21**, 10870–10878.
38 J. K. McCusker, *Science*, 2019, **363**, 484–488.
39 M. Rivera, L. Stojanović and R. Crespo-Otero, *J. Phys. Chem. A*, 2021, **125**, 1012–1024.
40 G. U. Nienhaus, *Angew. Chem., Int. Ed.*, 2008, **47**, 8992–8994.
41 H. Kandori, *Biophys. Rev.*, 2020, **12**, 355–361.
42 B. O. Leung and K. C. Chou, *Appl. Spectrosc.*, 2011, **65**, 967–980.
43 P. Vogel and K. N. Houk, *Organic Chemistry: Theory, Reactivity and Mechanisms in Modern Synthesis*, Wiley-VCH, Weinheim, 2019, pp. 710–726.
44 M. Persico and G. Granucci, *Photochemistry: A Modern Theoretical Perspective*, Springer, Cham, 2018, pp. 141–175.
45 G. J. Atchity, S. S. Xantheas and K. Ruedenberg, *J. Chem. Phys.*, 1991, **95**, 1862–1876.
46 H. Koppel, W. Domcke and L. S. Cederbaum, *Adv. Chem. Phys.*, 1984, **57**, 59–246.
47 D. R. Yarkony, *J. Phys. Chem.*, 1996, **100**, 18612–18628.
48 A. M. Virshup, J. Chen and T. J. Martínez, *J. Chem. Phys.*, 2012, **137**, 22–519.
49 N. Agmon, *J. Chem. Soc., Faraday Trans. 2*, 1978, **74**, 388–404.
50 Y. J. Hong and D. J. Tantillo, *Nat. Chem.*, 2009, **1**, 384–389.
51 M. Ruckenbauer, M. Barbatti, T. Müller and H. Lischka, *J. Phys. Chem. A*, 2013, **117**, 2790–2799.
52 J. Clayden, N. Greeves and S. Warren, *Organic Chemistry*, Oxford University Press, Second edn, 2001, pp. 240–267.
53 I. Fernández and F. M. Bickelhaupt, *Chem. Soc. Rev.*, 2014, **43**, 4953–4967.
54 D. G. Truhlar, B. C. Garrett and S. J. Klippenstein, *J. Phys. Chem.*, 1996, **100**, 12771–12800.
55 J. M. Anglada, J. M. Bofill and R. Crehuet, *J. Comput. Chem.*, 1999, **20**, 1112–1129.
56 V. Balzani, P. Ceroni and A. Juris, *Photochemistry and Photophysics. Concepts, Research, Applications*., Wiley-VCH, Weinheim, 2014, pp. 55–74.
57 H. An, H. Choi, Y. S. Lee and K. K. Baeck, *ChemPhysChem*, 2015, **16**, 1529–1534.
58 E. Pieri, D. Lahana, A. M. Chang, C. R. Aldaz, K. C. Thompson and T. J. Martínez, *Chem. Sci.*, 2021, **12**, 7294–7307.
59 L. M. Frutos, U. Sancho, M. Garavelli, M. Olivucci and O. Castaño, *J. Phys. Chem. A*, 2007, **111**, 2830–2838.
60 C. Wittig, *J. Phys. Chem. B*, 2005, **109**, 8428–8430.
61 L. D. Landau, *Phys. Z. Sowjetunion*, 1932, **1**, 88–98.
62 C. Zener, *Proc. R. Soc. London, Ser. A*, 1932, **137**, 696–702.
63 X. R. Ma, J. Zhang, Y. C. Xiong and W. Zhou, *Mol. Phys.*, 2022, **120**, e2051761.
64 T. R. Nelson, A. J. White, J. A. Bjorgaard, A. E. Sifain, Y. Zhang, B. Nebgen, S. Fernandez-Alberti, D. Mozyrsky, A. E. Roitberg and S. Tretiak, *Chem. Rev.*, 2020, **120**, 2215–2287.
65 A. Kühl and W. Domcke, *J. Chem. Phys.*, 2002, **116**, 2761.
66 W. Domcke and D. R. Yarkony, *Annu. Rev. Phys. Chem.*, 2012, **63**, 325–352.
67 J. Briand, O. Bräm, J. Réhault, J. Léonard, A. Cannizzo, M. Chergui, V. Zanirato, M. Olivucci, J. Helbing and S. Haacke, *Phys. Chem. Chem. Phys.*, 2010, **12**, 3178–3187.
68 J. P. Malhado and J. T. Hynes, *J. Chem. Phys.*, 2016, **145**, 194104.
69 W. Fuß, S. Lochbrunner, A. M. Muller, T. Schikarski, W. E. Schmid and S. A. Trushin, *Chem. Phys.*, 1998, **232**, 161–174.
70 R. M. Weiss and A. Warshel, *J. Am. Chem. Soc.*, 1979, **101**, 6131–6133.
71 J. E. Kim, M. J. Tauber and R. A. Mathies, *Biophys. J.*, 2003, **84**, 2492–2501.
72 M. A. Robb and M. Olivucci, *J. Photochem. Photobiol., A*, 2001, **144**, 237–243.
73 Q. Wang, R. W. Schoenlein, L. A. Peteanu, R. A. Mathies and C. V. Shank, *Science*, 1994, **266**, 422–424.
74 A. Kazaryan, J. C. M. Kistemaker, L. V. Schäfer, W. R. Browne, B. L. Feringa and M. Filatov, *J. Phys. Chem. A*, 2010, **114**, 5058–5067.
75 E. E. Nikitin, *J. Chem. Phys.*, 1996, **104**, 7059–7067.
76 E. E. Nikitin, *J. Chem. Phys.*, 1997, **107**, 6748–6755.

77 A. Alijah and E. E. Nikitin, *Mol. Phys.*, 1999, **96**, 1399–1410.
78 M. Desouter-Lecomte, C. Sannen and J. C. Lorquet, *J. Chem. Phys.*, 1983, **79**, 894–904.
79 M. Desouter-Lecomte, D. Dehareng, B. Leyh-Nihant, M. Th Praet, A. J. Lorquet and J. C. Lorquet, *J. Phys. Chem.*, 1985, **89**, 214–222.
80 C. A. Farfan and D. B. Turner, *Phys. Chem. Chem. Phys.*, 2020, **22**, 20265–20283.
81 I. Galván Fernández, M. G. Delcey, T. B. Pedersen, F. Aquilante and R. Lindh, *J. Chem. Theory Comput.*, 2016, **12**, 3636–3653.
82 M. Olivucci, F. Bernardi, S. Ottani and M. A. Robb, *J. Am. Chem. Soc.*, 1994, **116**, 2034–2048.
83 J. J. Serrano-Pérez, F. De Vleeschouwer, F. De Proft, D. Mendive-Tapia, M. J. Bearpark and M. A. Robb, *J. Org. Chem.*, 2013, **78**, 1874–1886.
84 A. Nenov, W. J. Schreier, F. O. Koller, M. Braun, R. De Vivie-Riedle, W. Zinth and I. Pugliesi, *J. Phys. Chem. A*, 2012, **116**, 10518–10528.
85 A. M. D. Lee, J. D. Coe, S. Ullrich, M. L. Ho, S. J. Lee, B. M. Cheng, M. Z. Zgierski, I. C. Chen, T. J. Martinez and A. Stolow, *J. Phys. Chem. A*, 2007, **111**, 11948–11960.
86 D. R. Yarkony, *J. Chem. Phys.*, 2000, **112**, 2111.
87 I. Fernández. Galván, A. Brakestad and M. Vacher, *Phys. Chem. Chem. Phys.*, 2022, **24**, 1638–1653.
88 S. Matsika, *Chem. Rev.*, 2021, **121**, 9407–9449.
89 I. Fernández Galván, M. G. Delcey, T. B. Pedersen, F. Aquilante and R. Lindh, *J. Chem. Theory Comput.*, 2016, **12**, 3636–3653.
90 V. Bonačić-Koutecký, J. Koutecký and J. Michl, *Angew. Chem., Int. Ed.*, 1987, **26**, 170–189.
91 M. Ben-Nun, F. Molnar, K. Schulten and T. J. Martínez, *Proc. Natl. Acad. Sci. U. S. A.*, 2002, **99**, 1769–1773.
92 D. R. Yarkony, *J. Chem. Phys.*, 2001, **114**, 2601–2613.
93 J. P. Malhado and J. T. Hynes, *J. Chem. Phys.*, 2012, **137**, 22A543.
94 G. J. Atchity, S. S. Xantheas and K. Ruedenberg, *J. Chem. Phys.*, 1991, **95**, 2601.
95 T. J. Martínez, *Chem. Phys. Lett.*, 1997, **272**, 139–147.
96 N. H. List, C. M. Jones and T. J. Martínez, *Chem. Sci.*, 2022, **13**, 373–385.
97 E. V. Anslyn and D. A. Dougherty, *Modern Physical Organic Chemistry*, University Science Books, Mill Valley, California, 2006, pp. 355–421.
98 G. Wu, A. E. Boguslavskiy, O. Schalk, M. S. Schuurman and A. Stolow, *J. Chem. Phys.*, 2011, **135**, 164309.
99 M. Manathunga, X. Yang, Y. Orozco-Gonzalez and M. Olivucci, *J. Phys. Chem. Lett.*, 2017, **8**, 5222–5227.
100 X. Yang, M. Manathunga, S. Gozem, J. Léonard, T. Andruniów and M. Olivucci, *Nat. Chem.*, 2022, **2022**, 1–9.
101 S. Oesterling, O. Schalk, T. Geng, R. D. Thomas, T. Hansson and R. De Vivie-Riedle, *Phys. Chem. Chem. Phys.*, 2017, **19**, 2025.
102 R. C. Couto and M. Kowalewski, *Phys. Chem. Chem. Phys.*, 2022, **24**, 19199–19208.
103 B. Gu and S. Mukamel, *J. Phys. Chem. Lett.*, 2021, **12**, 2052–2056.
104 F. Bernardi, M. Olivucci, J. J. W. McDouall and M. A. Robb, *J. Chem. Phys.*, 1998, **89**, 6365.
105 F. Bernardi, M. Olivucci and M. A. Robb, *Acc. Chem. Res.*, 1990, **23**, 405–412.
106 P. Celani, M. OIivucci, F. Bernard, S. Ottani and M. A. Robb, *J. Am. Chem. Soc.*, 1994, **116**, 10141–10151.
107 D. Sampedro Ruiz, A. Cembran, M. Garavelli, M. Olivucci and W. Fuß, *Photochem. Photobiol.*, 2002, **76**, 622–633.
108 L. Blancafort, P. Celani, M. J. Bearpark and M. A. Robb, *Theor. Chem. Acc.*, 2003, **110**, 92–99.
109 W. J. Glover, T. Mori, M. S. Schuurman, A. E. Boguslavskiy, O. Schalk, A. Stolow and T. J. Martínez, *J. Chem. Phys.*, 2018, **148**, 164303.
110 R. L. Christensen, M. G. I. Galinato, E. F. Chu, J. N. Howard, R. D. Broene and H. A. Frank, *J. Phys. Chem. A*, 2008, **112**, 12629–12636.
111 J. Michl and V. Bonačić-Koutecký, *Electronic Aspects of Organic Photochemistry*, Wiley-Interscience, New York, 1990.
112 M. Garavelli, P. Celani, M. Fato, M. J. Bearpark, B. R. Smith, M. Olivucci and M. A. Robb, *J. Phys. Chem. A*, 1997, **101**, 2023–2032.
113 I. Schapiro, M. N. Ryazantsev, L. M. Frutos, N. Ferré, R. Lindh and M. Olivucci, *J. Am. Chem. Soc.*, 2011, **133**, 3354–3364.
114 M. Garavelli, P. Celani, F. Bernardi, M. A. Robb and M. Olivucci, *J. Am. Chem. Soc.*, 1997, **119**, 6891–6901.
115 A. Sanchez-Galvez, P. Hunt, M. A. Robb, M. Olivucci, T. Vreven and H. B. Schlegel, *J. Am. Chem. Soc.*, 2000, **122**, 2911–2924.
116 Z. R. Grabowski and J. Dobkowski, *Pure Appl. Chem.*, 1983, **55**, 245–252.
117 R. J. MacDonell, O. Schalk, T. Geng, R. D. Thomas, R. Feifel, T. Hansson and M. S. Schuurman, *J. Chem. Phys.*, 2016, **145**, 114306.
118 M. Reguero, M. Olivucci, F. Bernardi and M. A. Robb, *J. Am. Chem. Soc.*, 1994, **116**, 2103–2114.
119 M. Reguero, I. B. Fernando Bernardi, A. Bottoni and M. A. Robb, *J. Am. Chem. Soc.*, 1991, **113**, 1566–1572.
120 L. Greenman and D. A. Mazziotti, *J. Chem. Phys.*, 2010, **133**, 164110.
121 M. Vacher, A. Brakestad, H. O. Karlsson, I. Fernández Galván and R. Lindh, *J. Chem. Theory Comput.*, 2017, **13**, 2448–2457.
122 L. Yue and Y. J. Liu, *J. Phys. Chem. Lett.*, 2022, **13**, 10671–10687.
123 M. Garavelli, B. Frabboni, M. Fato, P. Celani, F. Bernardi, M. A. Robb and M. Olivucci, *J. Am. Chem. Soc.*, 1999, **121**, 1537–1545.
124 P. Celani, F. Bernardi, M. Olivucci and M. A. Robb, *J. Chem. Phys.*, 1995, **102**, 5733–5742.
125 H. Ichikawa and K. Takatsuka, *J. Phys. Chem. A*, 2017, **121**, 315–325.
126 B. G. Levine and T. J. Martínez, *J. Phys. Chem. A*, 2009, **113**, 12815–12824.
127 S. P. Neville, M. Chergui, A. Stolow and M. S. Schuurman, *Phys. Rev. Lett.*, 2018, **120**, 243001.

128 I. Seidu, S. P. Neville, R. J. Macdonell and M. S. Schuurman, *Phys. Chem. Chem. Phys.*, 2022, **24**, 1345–1354.
129 R. J. MacDonell and M. S. Schuurman, *J. Phys. Chem. A*, 2019, **123**, 4693–4701.
130 R. J. MacDonell, M. E. Corrales, A. E. Boguslavskiy, L. Bañares, A. Stolow and M. S. Schuurman, *J. Chem. Phys.*, 2020, **152**, 084308.
131 A. E. Boguslavskiy, O. Schalk, N. Gador, W. J. Glover, T. Mori, T. Schultz, M. S. Schuurman, T. J. Martínez and A. Stolow, *J. Chem. Phys.*, 2018, **148**, 164302.
132 R. Srinivasan, *J. Am. Chem. Soc.*, 1962, **84**, 4141–4145.
133 D. H. Aue and R. N. Reynolds, *J. Am. Chem. Soc.*, 1973, **95**, 2027–2028.
134 T. Sovdat, G. Bassolino, M. Liebel, C. Schnedermann, S. P. Fletcher and P. Kukura, *J. Am. Chem. Soc.*, 2012, **134**, 8318–8320.
135 B. Demoulin, S. F. Altavilla, I. Rivalta and M. Garavelli, *J. Phys. Chem. Lett.*, 2017, **8**, 4407–4412.
136 R. Barata-Morgado, M. L. Sánchez, A. Muñoz-Losa, M. E. Martín, F. J. Olivares, D. Valle and M. A. Aguilar, *J. Phys. Chem. A*, 2018, **122**, 3096–3106.
137 S. P. Neville, Y. Wang, A. E. Boguslavskiy, A. Stolow and M. S. Schuurman, *J. Chem. Phys.*, 2016, **144**, 14305.
138 O. Schalk, A. E. Boguslavskiy and A. Stolow, *J. Phys. Chem. A*, 2010, **114**, 4058–4064.
139 J. S. Lim, Y. S. Lee and S. K. Kim, *Angew. Chem., Int. Ed.*, 2008, **47**, 1853–1856.
140 L. Pedraza-González, L. De Vico, M. D. C. Marĺn, F. Fanelli and M. Olivucci, *J. Chem. Theory Comput.*, 2019, **15**, 3134–3152.
141 P. O. Dral and M. Barbatti, *Nat. Rev. Chem.*, 2021, **5**, 388–405.
142 G. W. Richings and S. Habershon, *Acc. Chem. Res.*, 2022, **55**, 209–220.
143 J. Westermayr and P. Marquetand, *Chem. Rev.*, 2021, **121**, 9873–9926.
144 D. Hu, Y. Xie, X. Li, L. Li and Z. Lan, *J. Phys. Chem. Lett.*, 2018, **9**, 2725–2732.
145 G. W. Richings, C. Robertson and S. Habershon, *J. Chem. Theory Comput.*, 2019, **15**, 857–870.
146 J. Westermayr, P. Marquetand and P. Marquetand, *J. Chem. Phys.*, 2020, **153**, 154112.
147 T. Husch, J. Sun, L. Cheng, S. J. R. Lee and T. F. Miller, *J. Chem. Phys.*, 2021, **154**, 064108.
148 S. Mai, P. Marquetand and L. González, *Wiley Interdiscip. Rev.: Comput. Mol. Sci.*, 2018, **8**, e1370.
149 C. Ciminelli, G. Granucci and M. Persico, *Chem. – Eur. J.*, 2004, **10**, 2327–2341.
150 D. Tuna, L. Spörkel, M. Barbatti and W. Thiel, *Chem. Phys.*, 2018, **515**, 521–534.
151 J. K. Yu, C. Bannwarth, R. Liang, E. G. Hohenstein and T. J. Martínez, *J. Am. Chem. Soc.*, 2020, **142**, 20680–20690.
152 S. Gozem, H. L. Luk, I. Schapiro and M. Olivucci, *Chem. Rev.*, 2017, **117**, 13502–13565.
153 G. Bassolino, T. Sovdat, M. Liebel, C. Schnedermann, B. Odell, T. D. W. Claridge, P. Kukura and S. P. Fletcher, *J. Am. Chem. Soc.*, 2014, **136**, 2650–2658.
154 A. Cheminal, J. Léonard, S. Y. Kim, K. H. Jung, H. Kandori and S. Haacke, *Phys. Chem. Chem. Phys.*, 2015, **17**, 25429–25439.
155 M. Gueye, M. Manathunga, D. Agathangelou, Y. Orozco, M. Paolino, S. Fusi, S. Haacke, M. Olivucci and J. Leónard, *Nat. Commun.*, 2018, **9**, 1–8.
156 M. M. T. El-Tahawy, A. Nenov, O. Weingart, M. Olivucci and M. Garavelli, *J. Phys. Chem. Lett.*, 2018, **9**, 3315–3322.
157 J. C. Tully and R. K. Preston, *J. Chem. Phys.*, 1971, **55**, 562.
158 J. C. Tully, *J. Chem. Phys.*, 1990, **93**, 1061.
159 A. K. Belyaev, C. Lasser and G. Trigila, *J. Chem. Phys.*, 2014, **140**, 224108.
160 J. C. Tully, *J. Chem. Phys.*, 2012, **137**, 22A301.
161 M. Sala and D. Egorova, *Chem. Phys.*, 2016, **481**, 206–217.
162 V. I. Prokhorenko, A. M. Nagy, S. A. Waschuk, L. S. Brown, R. R. Birge and R. J. D. Miller, *Science*, 2006, **313**, 1257–1261.
163 A. W. Jasper and D. G. Truhlar, *J. Chem. Phys.*, 2005, **122**, 044101.
164 C. A. Farfan and D. B. Turner, *J. Phys. Chem. A*, 2019, **123**, 7768–7776.
165 M. V. Berry, *Proc. R. Soc. London, Ser. A*, 1984, **392**, 45–57.
166 V. Bonačić-Koutecký, K. Schöffel and J. Michl, *Theor. Chim. Acta*, 1987, **72**, 459–474.
167 R. W. Schoenlein, L. A. Peteanu, R. A. Mathies and C. V. Shank, *Science*, 1991, **254**, 412–415.
168 H. Kuramochi and T. Tahara, *J. Am. Chem. Soc.*, 2021, **143**, 9699–9717.
169 M. Liebel, C. Schnedermann, T. Wende and P. Kukura, *J. Phys. Chem. A*, 2015, **119**, 9506–9517.
170 C. Schnedermann, M. Liebel and P. Kukura, *J. Am. Chem. Soc.*, 2015, **137**, 2886–2891.
171 P. B. Coto, A. Sinicropi, L. De Vico, N. Ferré and M. Olivucci, *Mol. Phys.*, 2006, **104**, 983–991.
172 L. Dhar, J. A. Rogers and K. A. Nelson, *Chem. Rev.*, 1994, **94**, 157–193.
173 J. Léonard, I. Schapiro, J. Briand, S. Fusi, R. R. Paccani, M. Olivucci and S. Haacke, *Chem. – Eur. J.*, 2012, **18**, 15296–15304.
174 T. Wende, M. Liebel, C. Schnedermann, R. J. Pethick and P. Kukura, *J. Phys. Chem. A*, 2014, **118**, 9976–9984.
175 W. H. Miller, *J. Chem. Phys.*, 2012, **136**, 210901.
176 T. Rosenfeld, B. Honig, M. Ottolenghi, J. Hurley and T. G. Ebrey, *Pure Appl. Chem.*, 1977, **49**, 341–351.
177 P. Kukura, D. W. McCamant, S. Yoon, D. B. Wandschneider and R. A. Mathies, *Science*, 2005, **310**, 1006–1009.
178 P. J. M. Johnson, A. Halpin, T. Morizumi, V. I. Prokhorenko, O. P. Ernst and R. J. D. Miller, *Nat. Chem.*, 2015, **7**, 980–986.
179 R. A. Mathies, *Nat. Chem.*, 2015, **7**, 945–947.
180 G. R. Loppnow and R. A. Mathies, *Biophys. J.*, 1988, **54**, 35–43.
181 L. M. Frutos, T. Andruniów, F. Santoro, N. Ferré and M. Olivucci, *Proc. Natl. Acad. Sci. U. S. A.*, 2007, **104**, 7764–7769.

182 A. Warshel, *Nature*, 1976, **260**, 679–683.
183 I. Schapiro, O. Weingart and V. Buss, *J. Am. Chem. Soc.*, 2009, **131**, 16–17.
184 R. González-Luque, M. Garavelli, F. Bernardi, M. Merchán, M. A. Robb and M. Olivucci, *Proc. Natl. Acad. Sci. U. S. A.*, 2000, **97**, 9379–9384.
185 O. Weingart, *J. Am. Chem. Soc.*, 2007, **129**, 10618–10619.
186 M. Liebel, C. Schnedermann, G. Bassolino, G. Taylor, A. Watts and P. Kukura, *Phys. Rev. Lett.*, 2014, **112**, 238301.
187 W. H. Miller, *J. Phys. Chem. A*, 2009, **113**, 1405–1415.
188 S. Gozem, F. Melaccio, R. Lindh, A. I. Krylov, A. A. Granovsky, C. Angeli and M. Olivucci, *J. Chem. Theory Comput.*, 2013, **9**, 4495–4506.
189 G. Zgrablić, A. M. Novello and F. Parmigiani, *J. Am. Chem. Soc.*, 2012, **134**, 955–961.
190 O. Weingart and M. Garavelli, *J. Chem. Phys.*, 2012, **137**, 22A523.
191 O. Weingart, P. Altoè, M. Stenta, A. Bottoni, G. Orlandi and M. Garavelli, *Phys. Chem. Chem. Phys.*, 2011, **13**, 3645–3648.
192 H. G. Duan, R. J. D. Miller and M. Thorwart, *J. Phys. Chem. Lett.*, 2016, **7**, 3491–3496.
193 D. L. Qi, H. G. Duan, Z. R. Sun, R. J. D. Miller and M. Thorwart, *J. Chem. Phys.*, 2017, **147**, 074101.
194 C. Schnedermann, X. Yang, M. Liebel, K. M. Spillane, J. Lugtenburg and I. Fernández, *Nat. Chem.*, 2018, **10**, 449–455.
195 A. Ockenfels, I. Schapiro and W. Gärtner, *Photochem. Photobiol. Sci.*, 2016, **15**, 297–308.
196 G. Eyring, B. Curry, A. Broek, J. Lugtenburg and R. Mathies, *Biochemistry*, 1982, **21**, 384–393.
197 C. Schnedermann and R. A. Mathies, On the Critical Role of Vibrational Phase in the Photochemistry of Vision, **https://chemistrycommunity.nature.com/amp/posts/31527-on-the-critical-role-of-vibrational-phase-in-the-photochemistry-of-vision**, accessed 20 November 2022.
198 A. Valentini, D. Rivero, F. Zapata, C. García-Iriepa, M. Marazzi, R. Palmeiro, I. Fernández. Galván, D. Sampedro, M. Olivucci and L. M. Frutos, *Angew. Chem., Int. Ed.*, 2017, **56**, 3842–3846.
199 R. Liang, J. K. Yu, J. Meisner, F. Liu and T. J. Martinez, *J. Am. Chem. Soc.*, 2021, **143**, 5425–5437.
200 M. Filatov, S. Kyu Min and K. S. Kim, *J. Chem. Theory Comput.*, 2018, **14**, 4499–4512.
201 O. Weingart, I. Schapiro and V. Buss, *J. Mol. Model.*, 2006, **12**, 713–721.
202 O. Weingart, V. Buss and M. A. Robb, *Phase Trans.*, 2005, **78**, 17–24.
203 L. Vuković, C. F. Burmeister, P. Král and G. Groenhof, *J. Phys. Chem. Lett.*, 2013, **4**, 1005–1011.
204 H. Kandori, H. Sasabe, K. Nakanishi, T. Yoshizawa, T. Mizukami and Y. Shichida, *J. Am. Chem. Soc.*, 1996, **118**, 1002–1005.
205 P. H. M. Bovee-Geurts, J. Lugtenburg and W. J. DeGrip, *Biochim. Biophys. Acta, Bioenerg.*, 2017, **1858**, 118–125.
206 L. A. Bizimana, C. A. Farfan, J. Brazard and D. B. Turner, *J. Phys. Chem. Lett.*, 2019, **10**, 3550–3556.
207 J. Dasgupta, R. R. Frontiera, K. C. Taylor, J. C. Lagarias and R. A. Mathies, *Proc. Natl. Acad. Sci. U. S. A.*, 2009, **106**, 1784–1789.
208 W. Fuß, *Phys. Chem. Chem. Phys.*, 2019, **21**, 6776–6789.
209 R. S. H. Liu and G. S. Hammond, *Proc. Natl. Acad. Sci. U. S. A.*, 2000, **97**, 11153–11158.
210 W. Fuß, C. Kosmidis, W. E. Schmid and S. A. Trushin, *Angew. Chem., Int. Ed.*, 2004, **43**, 4178–4182.
211 D. Morozov and G. Groenhof, *Angew. Chem.*, 2016, **128**, 586–588.
212 J. W. Park and Y. M. Rhee, *J. Am. Chem. Soc.*, 2016, **138**, 13619–13629.
213 H. Niwa, S. Inouye, T. Hirano, T. Matsuno, S. Kojima, M. Kubota, M. Ohashi and F. I. Tsuji, *Proc. Natl. Acad. Sci. U. S. A.*, 1996, **93**, 13617–13622.
214 T. Grotjohann, I. Testa, M. Leutenegger, H. Bock, N. T. Urban, F. Lavoie-Cardinal, K. I. Willig, C. Eggeling, S. Jakobs and S. W. Hell, *Nature*, 2011, **478**, 204–208.
215 Q. Zhang, X. Chen, G. Cui, W.-H. Fang and W. Thiel, *Angew. Chem.*, 2014, **126**, 8793–8797.
216 V. B. Delchev, A. L. Sobolewski and W. Domcke, *Phys. Chem. Chem. Phys.*, 2010, **12**, 5007–5015.
217 M. A. Ismail, N. Blancafort, L. Olivucci, M. Kohler and B. Robb, *J. Am. Chem. Soc.*, 2002, **124**, 6818–6819.
218 M. Merchán, R. González-Luque, T. Climent, L. Serrano-Andrés, E. Rodríguez, M. Reguero and D. Peláez, *J. Phys. Chem. B*, 2006, **110**, 26471–26476.
219 M. Gueye, M. Paolino, E. Gindensperger, S. Haacke, M. Olivucci and J. Léonard, *Faraday Discuss.*, 2019, **221**, 299–321.
220 I. Schapiro, S. Fusi, M. Olivucci, T. Andruniów, S. Sasidharanpillai and G. R. Loppnow, *J. Phys. Chem. B*, 2014, **118**, 12243–12250.
221 F. Lumento, V. Zanirato, S. Fusi, E. Busi, L. Latterini, F. Elisei, A. Sinicropi, T. Andruniów, N. Ferré, R. Basosi and M. Olivucci, *Angew. Chem.*, 2007, **119**, 418–424.
222 A. Sinicropi, E. Martin, M. Ryazantsev, J. Helbing, J. Briand, D. Sharma, J. Léonard, S. Haacke, A. Cannizzo, M. Chergui, V. Zanirato, S. Fusi, F. Santoro, R. Basosi, N. Ferré and M. Olivucci, *Proc. Natl. Acad. Sci. U. S. A.*, 2008, **105**, 17642–17647.
223 A. Kazaryan, Z. Lan, L. V. Schäfer, W. Thiel and M. Filatov, *J. Chem. Theory Comput.*, 2011, **7**, 2189–2199.
224 L. Liu, W.-H. Fang and T. J. Martinez, *J. Am. Chem. Soc.*, 2023, DOI: **10.1021/jacs.3c00275**.
225 U. Banin and S. Ruhman, *J. Chem. Phys.*, 1993, **98**, 4391–4403.
226 M. J. Rosker, M. Dantus and A. H. Zewail, *J. Chem. Phys.*, 1988, **89**, 6113–6127.
227 M. Dantus, R. M. Bowman, M. Gruebele and A. H. Zewail, *J. Chem. Phys.*, 1989, **91**, 7437–7450.
228 S. A. Trushin, W. Fuss, K. L. Kompa and W. E. Schmid, *J. Phys. Chem. A*, 2000, **104**, 1997–2006.
229 S. A. Trushin, W. Fuss, W. E. Schmid and K. L. Kompa, *J. Phys. Chem. A*, 1998, **102**, 4129–4137.
230 F. Bernardi, M. Olivucci and M. A. Robb, *J. Photochem. Photobiol., A*, 1997, **105**, 365–371.

231 W. Fuß, W. E. Schmid and S. A. Trushin, *J. Chem. Phys.*, 2000, **112**, 8347–8362.
232 K. Kosma, S. A. Trushin, W. Fuß and W. E. Schmid, *Phys. Chem. Chem. Phys.*, 2009, **11**, 172–181.
233 S. Li, B. Jochim, J. E. Jackson and M. Dantus, *J. Chem. Phys.*, 2021, **155**, 044303.
234 K. Haiser, B. P. Fingerhut, K. Heil, A. Glas, T. T. Herzog, B. M. Pilles, W. J. Schreier, W. Zinth, R. de Vivie-Riedle and T. Carell, *Angew. Chem., Int. Ed.*, 2012, **51**, 408–411.
235 D. E. Lemaire and B. P. Ruzsicska, *Photochem. Photobiol.*, 1993, **57**, 755–757.
236 Y. J. Ai, R. Z. Liao, S. F. Chen, Y. Luo and W. H. Fang, *J. Phys. Chem. B*, 2010, **114**, 14096–14102.
237 K. A. Kistler and S. Matsika, *J. Chem. Phys.*, 2008, **128**, 215102.
238 M. B. Smith and J. Michl, *Chem. Rev.*, 2010, **110**, 6891–6936.
239 H. L. Stern, A. Cheminal, S. R. Yost, K. Broch, S. L. Bayliss, K. Chen, M. Tabachnyk, K. Thorley, N. Greenham, J. M. Hodgkiss, J. Anthony, M. Head-Gordon, A. J. Musser, A. Rao and R. H. Friend, *Nat. Chem.*, 2017, **9**, 1205–1212.
240 N. R. Monahan, D. Sun, H. Tamura, K. W. Williams, B. Xu, Y. Zhong, B. Kumar, C. Nuckolls, A. R. Harutyunyan, G. Chen, H.-L. Dai, D. Beljonne, Y. Rao and X.-Y. Zhu, *Nat. Chem.*, 2017, **9**, 341–346.
241 A. J. Musser, M. Liebel, C. Schnedermann, T. Wende, T. B. Kehoe, A. Rao and P. Kukura, *Nat. Phys.*, 2015, **11**, 352–357.
242 H.-G. Duan, A. Jha, X. Li, V. Tiwari, H. Ye, P. K. Nayak, X.-L. Zhu, L. Zheng, T. J. Martinez, M. Thorwart and R. J. D. Miller, *Sci. Adv.*, 2020, **6**, eabb0052.
243 A. M. Alvertis, S. Lukman, T. J. H. Hele, E. G. Fuemmeler, J. Feng, J. Wu, N. C. Greenham, A. W. Chin and A. J. Musser, *J. Am. Chem. Soc.*, 2019, **141**, 17558–17570.
244 W. Kim and A. J. Musser, *Adv. Phys. X*, 2021, **6**, 1918022.
245 C. Schnedermann, A. M. Alvertis, T. Wende, S. Lukman, J. Feng, F. A. Y. N. Schröder, D. H. P. Turban, J. Wu, N. D. M. Hine, N. C. Greenham, A. W. Chin, A. Rao, P. Kukura and A. J. Musser, *Nat. Commun.*, 2019, **10**, 1–11.
246 F. A. Y. N. Schröder, D. H. P. Turban, A. J. Musser, N. D. M. Hine and A. W. Chin, *Nat. Commun.*, 2019, **10**, 1062.
247 S. Lukman, K. Chen, J. M. Hodgkiss, D. H. P. Turban, N. D. M. Hine, S. Dong, J. Wu, N. C. Greenham and A. J. Musser, *Nat. Commun.*, 2016, **7**, 1–13.
248 S. Lukman, A. J. Musser, K. Chen, S. Athanasopoulos, C. K. Yong, Z. Zeng, Q. Ye, C. Chi, J. M. Hodgkiss, J. Wu, R. H. Friend and N. C. Greenham, *Adv. Funct. Mater.*, 2015, **25**, 5452–5461.
249 T. Nelson, S. Fernandez-Alberti, V. Chernyak, A. E. Roitberg and S. Tretiak, *J. Phys. Chem. B*, 2011, **115**, 5402–5414.
250 T. R. Nelson, D. Ondarse-Alvarez, N. Oldani, B. Rodriguez-Hernandez, L. Alfonso-Hernandez, J. F. Galindo, V. D. Kleiman, S. Fernandez-Alberti, A. E. Roitberg and S. Tretiak, *Nat. Commun.*, 2018, **9**, 1–9.
251 S. M. Falke, C. A. Rozzi, D. Brida, M. Maiuri, M. Amato, E. Sommer, A. De Sio, A. Rubio, G. Cerullo, E. Molinari and C. Lienau, *Science*, 2014, **344**, 1001–1005.
252 A. De Sio, F. V. D. A. Camargo, K. Winte, E. Sommer, F. Branchi, G. Cerullo and C. Lienau, *Eur. Phys. J. B*, 2018, **91**, 236.
253 A. G. Dijkstra, C. Wang, J. Cao and G. R. Fleming, *J. Phys. Chem. Lett.*, 2015, **6**, 627–632.
254 F. R. Díaz, H. G. Duan, R. J. D. Miller and M. Thorwart, *J. Phys. Chem. B*, 2021, **125**, 8869–8875.
255 T. Pullerits, D. Zigmantas and V. Sundström, *Proc. Natl. Acad. Sci. U. S. A.*, 2013, **110**, 1148–1149.
256 E. Thyrhaug, R. Tempelaar, M. J. P. Alcocer, K. Žídek, D. Bína, J. Knoester, T. L. C. Jansen and D. Zigmantas, *Nat. Chem.*, 2018, **10**, 780–786.
257 E. Bukartė, A. Haufe, D. Paleček, C. Büchel and D. Zigmantas, *Chem. Phys.*, 2020, **530**, 110643.
258 S. Sil, R. W. Tilluck, N. Mohan T. M, C. H. Leslie, J. B. Rose, M. A. Domínguez-Martín, W. Lou, C. A. Kerfeld and W. F. Beck, *Nat. Chem.* 2022, 2022, 1–9.
259 K. H. Cho and Y. M. Rhee, *J. Phys. Chem. B*, 2021, **125**, 5601–5610.
260 K. H. Cho and Y. M. Rhee, *Phys. Chem. Chem. Phys.*, 2021, **23**, 26623–26639.
261 J. Clark, C. Silva, R. H. Friend and F. C. Spano, *Phys. Rev. Lett.*, 2007, **98**, 206406.
262 S. Tretiak, A. Saxena, R. L. Martin and A. R. Bishop, *Phys. Rev. Lett.*, 2002, **89**, 097402.
263 F. C. Spano, *Annu. Rev. Phys. Chem.*, 2006, **57**, 217–243.
264 G. A. Worth and L. S. Cederbaum, *Annu. Rev. Phys. Chem.*, 2004, **55**, 127–158.
265 S. Kang, T. Kim, Y. Hong, F. Würthner and D. Kim, *J. Am. Chem. Soc.*, 2021, **143**, 9825–9833.
266 S. Rafiq, B. Fu, B. Kudisch and G. D. Scholes, *Nat. Chem.*, 2020, **13**, 70–76.
267 R. Huber, L. Dworak, J. E. Moser, M. Grätzel and J. Wachtveitl, *J. Phys. Chem. C*, 2016, **120**, 8534–8539.
268 C. Zimmermann, F. Willig, S. Ramakrishna, B. Burfeindt, B. Pettinger, R. Eichberger and W. Storck, *J. Phys. Chem. B*, 2001, **105**, 9245–9253.
269 A. Aster, A.-B. Bornhof, N. Sakai, S. Matile and E. Vauthey, *J. Phys. Chem. Lett.*, 2021, **12**, 1052–1057.
270 J. Krčmář, M. F. Gelin, D. Egorova and W. Domcke, *J. Phys. B*, 2014, **47**, 124019.
271 M. Khalil, N. Demirdöven and A. Tokmakoff, *J. Chem. Phys.*, 2004, **121**, 362.
272 M. J. Nee, C. R. Baiz, J. M. Anna, R. McCanne and K. J. Kubarych, *J. Chem. Phys.*, 2008, **129**, 084503.
273 T. L. Courtney, Z. W. Fox, L. Estergreen and M. Khalil, *J. Phys. Chem. Lett.*, 2015, **6**, 1286–1292.
274 J. D. Gaynor, A. Petrone, X. Li and M. Khalil, *J. Phys. Chem. Lett.*, 2018, **9**, 6289–6295.
275 Z. W. Fox, T. J. Blair and M. Khalil, *J. Phys. Chem. Lett.*, 2020, **11**, 1558–1563.
276 L. Blancafort, F. Jolibois, M. Olivucci and M. A. Robb, *J. Am. Chem. Soc.*, 2001, **123**, 722–732.
277 A. De Sio, E. Sommer, X. T. Nguyen, L. Groß, D. Popović, B. T. Nebgen, S. Fernandez-Alberti, S. Pittalis, C. A. Rozzi, E. Molinari, E. Mena-Osteritz, P. Bäuerle, T. Frauenheim,

S. Tretiak and C. Lienau, *Nat. Nanotechnol.*, 2020, **16**, 63–68.
278 S. Biswas, J. W. Kim, X. Zhang and G. D. Scholes, *Chem. Rev.*, 2022, **122**, 4257–4321.
279 J. A. Weinstein, *Nat. Chem.*, 2020, **12**, 789–790.
280 Y. Shu and B. G. Levine, *J. Chem. Phys.*, 2013, **139**, 81102.
281 W. T. Peng, B. S. Fales, Y. Shu and B. G. Levine, *Chem. Sci.*, 2018, **9**, 681–687.
282 Y. Shu, B. S. Fales and B. G. Levine, *Nano Lett.*, 2015, **15**, 6247–6253.
283 B. G. Levine, M. P. Esch, B. S. Fales, D. T. Hardwick, W.-T. Peng and Y. Shu, *Annu. Rev. Phys. Chem.*, 2019, **70**, 21–43.
284 Y. Shu, B. S. Fales, W. T. Peng and B. G. Levine, *J. Phys. Chem. Lett.*, 2017, **8**, 4091–4099.
285 D. W. Dequilettes, K. Frohna, D. Emin, T. Kirchartz, V. Bulovic, D. S. Ginger and S. D. Stranks, *Chem. Rev.*, 2019, **119**, 11007–11019.
286 M. P. Esch, Y. Shu and B. G. Levine, *J. Phys. Chem. A*, 2019, **123**, 2661–2673.
287 B. C. Paulus, S. L. Adelman, L. L. Jamula and J. K. McCusker, *Nature*, 2020, **582**, 214–219.
288 P. Kim, A. J. S. Valentine, S. Roy, A. W. Mills, A. Chakraborty, F. N. Castellano, X. Li and L. X. Chen, *J. Phys. Chem. Lett.*, 2021, **12**, 6794–6803.
289 T. W. Kim, P. Kim, A. W. Mills, A. Chakraborty, S. Kromer, A. J. S. Valentine, F. N. Castellano, X. Li and L. X. Chen, *J. Phys. Chem. C*, 2022, **126**, 11487–11497.
290 Y. Shao, H. J. M. de Groot and B. Francesco, *ChemSusChem*, 2020, **13**, 1–9.
291 E. G. Fuemmeler, S. N. Sanders, A. B. Pun, E. Kumarasamy, T. Zeng, K. Miyata, M. L. Steigerwald, X.-Y. Zhu, M. Y. Sfeir, L. M. Campos and N. Ananth, *ACS Cent. Sci.*, 2016, **2**, 316–324.
292 S. Mai, M. Pollum, L. Martínez-Fernández, N. Dunn, P. Marquetand, I. Corral, C. E. Crespo-Hernández and L. González, *Nat. Commun.*, 2016, **7**, 1–8.
293 J. P. Zobel, J. J. Nogueira and L. González, *Chem. – Eur. J.*, 2018, **24**, 5379–5387.
294 D. Valverde, S. Mai, A. V. Sanches de Araújo, S. Canuto, L. González and A. C. Borin, *Phys. Chem. Chem. Phys.*, 2021, **23**, 5447–5454.
295 Y. Wang and D. R. Yarkony, *J. Chem. Phys.*, 2021, **155**, 174115.
296 J. N. Schrauben, K. L. Dillman, W. F. Beck and J. K. McCusker, *Chem. Sci.*, 2010, **1**, 405–410.
297 J. D. Gaynor, J. Sandwisch and M. Khalil, *Nat. Commun.*, 2019, **10**, 1–9.
298 J. G. Kim, S. Nozawa, H. Kim, E. H. Choi, T. Sato, T. W. Kim, K. H. Kim, H. Ki, J. Kim, M. Choi, Y. Lee, J. Heo, K. Y. Oang, K. Ichiyanagi, R. Fukaya, J. H. Lee, J. Park, I. Eom, S. H. Chun, S. Kim, M. Kim, T. Katayama, T. Togashi, S. Owada, M. Yabashi, S. J. Lee, S. Lee, C. W. Ahn, D. S. Ahn, J. Moon, S. Choi, J. Kim, T. Joo, J. Kim, S. Ichi Adachi and H. Ihee, *Nature*, 2020, **582**, 520–524.
299 J. G. Kim, E. H. Choi, Y. Lee and H. Ihee, *Acc. Chem. Res.*, 2021, **54**, 27.
300 M. Park, A. J. Neukirch, S. E. Reyes-Lillo, M. Lai, S. R. Ellis, D. Dietze, J. B. Neaton, P. Yang, S. Tretiak and R. A. Mathies, *Nat. Commun.*, 2018, **9**, 1–9.
301 M. Maiuri, M. Garavelli and G. Cerullo, *J. Am. Chem. Soc.*, 2019, **142**, 3–15.
302 I. A. Heisler and S. R. Meech, *Chem. Soc. Rev.*, 2021, **50**, 11486–11502.
303 T. Brixner, J. Stenger, H. M. Vaswani, M. Cho, R. E. Blankenship and G. R. Fleming, *Nature*, 2005, **434**, 625–628.
304 G. Fumero, C. Schnedermann, G. Batignani, T. Wende, M. Liebel, G. Bassolino, C. Ferrante, S. Mukamel, P. Kukura and T. Scopigno, *Phys. Rev. X*, 2020, **10**, 011051.
305 J. D. Gaynor, R. B. Weakly and M. Khalil, *J. Chem. Phys.*, 2021, **154**, 184201.
306 R. B. Weakly, J. D. Gaynor and M. Khalil, *J. Chem. Phys.*, 2021, **154**, 184202.
307 D. R. Austin, A. S. Johnson, F. McGrath, D. Wood, L. Miseikis, T. Siegel, P. Hawkins, A. Harvey, Z. Mašín, S. Patchkovskii, M. Vacher, J. P. Malhado, M. Y. Ivanov, O. Smirnova and J. P. Marangos, *Sci. Rep.*, 2021, **11**, 1–8.
308 H. Kuramochi, S. Takeuchi, H. Kamikubo, M. Kataoka and T. Tahara, *Sci. Adv.*, 2019, **5**, eaau4490.
309 J. P. Kraack, A. Wand, T. Buckup, M. Motzkus and S. Ruhman, *Phys. Chem. Chem. Phys.*, 2013, **15**, 14487–14501.
310 T. Buckup and M. Motzkus, *Annu. Rev. Phys. Chem.*, 2014, **65**, 39–57.
311 H. Kuramochi, S. Takeuchi, K. Yonezawa, H. Kamikubo, M. Kataoka and T. Tahara, *Nat. Chem.*, 2017, **9**, 660–666.
312 H. Seiler, M. Krynski, D. Zahn, S. Hammer, Y. W. Windsor, T. Vasileiadis, J. Pflaum, R. Ernstorfer, M. Rossi and H. Schwoerer, *Sci. Adv.*, 2021, **7**, eabg0869.
313 J. Yang, X. Zhu, J. P. F. Nunes, J. K. Yu, R. M. Parrish, T. J. A. Wolf, M. Centurion, M. Gühr, R. Li, Y. Liu, B. Moore, M. Niebuhr, S. Park, X. Shen, S. Weathersby, T. Weinacht, T. J. Martinez and X. Wang, *Science*, 2020, **368**, 885–889.
314 C. Pellegrini, A. Marinelli and S. Reiche, *Rev. Mod. Phys.*, 2016, **88**, 015006.
315 A. R. Attar, A. Bhattacherjee, C. D. Pemmaraju, K. Schnorr, K. D. Closser, D. Prendergast and S. R. Leone, *Science*, 2017, **356**, 54–59.
316 A. Bhattacherjee and S. R. Leone, *Acc. Chem. Res.*, 2018, **51**, 3203–3211.
317 H. Timmers, X. Zhu, Z. Li, Y. Kobayashi, M. Sabbar, M. Hollstein, M. Reduzzi, T. J. Martínez, D. M. Neumark and S. R. Leone, *Nat. Commun.*, 2019, **10**, 1–8.
318 K. S. Zinchenko, F. Ardana-Lamas, I. Seidu, S. P. Neville, J. van der Veen, V. U. Lanfaloni, M. S. Schuurman and H. J. Wörner, *Science*, 2021, **371**, 489–494.
319 D. T. Matselyukh, V. Despré, N. V. Golubev, A. I. Kuleff and H. J. Wörner, *Nat. Phys.*, 2022, **18**, 1206–1213.
320 T. Schnappinger, D. Jadoun, M. Gudem and M. Kowalewski, *Chem. Commun.*, 2022, **58**, 12763–12781.

321 M. Kowalewski, B. P. Fingerhut, K. E. Dorfman, K. Bennett and S. Mukamel, *Chem. Rev.*, 2017, **117**, 12165–12226.
322 K. Bennett, M. Kowalewski, J. R. Rouxel and S. Mukamel, *Proc. Natl. Acad. Sci. U. S. A.*, 2018, **115**, 6538–6547.
323 H. Yong, D. Keefer and S. Mukamel, *J. Am. Chem. Soc.*, 2022, **144**, 7796–7804.
324 D. Jadoun, M. Gudem and M. Kowalewski, *Struct. Dyn.*, 2021, **8**, 034101.
325 D. Keefer, T. Schnappinger, R. de Vivie-Riedle and S. Mukamel, *Proc. Natl. Acad. Sci. U. S. A.*, 2020, **117**, 24069–24075.
326 D. Keefer, V. M. Freixas Lemus, H. Song, S. Tretiak, S. Fernandez-Alberti and S. Mukamel, *Chem. Sci.*, 2021, **12**, 5286–5294.
327 D. Keefer, J. R. Rouxel, F. Aleotti, F. Segatta, M. Garavelli and S. Mukamel, *J. Am. Chem. Soc.*, 2021, **143**, 13806–13815.
328 G. Chatterjee, A. Jha, A. Blanco-Gonzalez, V. Tiwari, M. Manathunga, H. G. Duan, F. Tellkamp, I. V. Prokhorenko, N. Ferré, J. Dasgupta, M. Olivucci and R. J. D. Miller, *Chem. Sci.*, 2022, **13**, 9392–9400.
329 X. F. Xu, A. Kahan, S. Zilberg and Y. Haas, *J. Phys. Chem. A*, 2009, **113**, 9779–9791.
330 E. M. Kempfer-Robertson and L. M. Thompson, *J. Phys. Chem. A*, 2020, **124**, 3520–3529.
331 M. Liebel and P. Kukura, *Nat. Chem.*, 2016, **9**, 45–49.
332 D. Geppert, L. Seyfarth and R. De Vivie-Riedle, *Applied Physics B: Lasers and Optics*, Springer, 2004, vol. 79, pp. 987–992.
333 M. Kübel, R. Siemering, C. Burger, N. G. Kling, H. Li, A. S. Alnaser, B. Bergues, S. Zherebtsov, A. M. Azzeer, I. Ben-Itzhak, R. Moshammer, R. De Vivie-Riedle and M. F. Kling, *Phys. Rev. Lett.*, 2016, **116**, 193001.
334 A. S. Alnaser, M. Kübel, R. Siemering, B. Bergues, N. G. Kling, K. J. Betsch, Y. Deng, J. Schmidt, Z. A. Alahmed, A. M. Azzeer, J. Ullrich, I. Ben-Itzhak, R. Moshammer, U. Kleineberg, F. Krausz, R. De Vivie-Riedle and M. F. Kling, *Nat. Commun.*, 2014, **5**, 1–6.
335 H. Li, N. G. Kling, B. Förg, J. Stierle, A. Kessel, S. A. Trushin, M. F. Kling and S. Kaziannis, *Struct. Dyn.*, 2016, **3**, 043206.
336 S. Rafiq and G. D. Scholes, *J. Am. Chem. Soc.*, 2019, **141**, 708–722.
337 R. R. Frontiera, *J. Phys. Chem. B*, 2022, **126**, 5727–5729.
338 Y. Yoneda, B. Kudisch, S. Rafiq, M. Maiuri, Y. Nagasawa, G. D. Scholes and H. Miyasaka, *J. Am. Chem. Soc.*, 2021, **143**, 14511–14522.
339 A. Kahan, A. Wand, S. Ruhman, S. Zilberg and Y. Haas, *J. Phys. Chem. A*, 2011, **115**, 10854–10861.
340 M. Olivucci, T. Tran, G. A. Worth and M. A. Robb, *J. Phys. Chem. Lett.*, 2021, **12**, 5639–5643.